

Modelling and Diagnosis of Solid Oxide Fuel Cell (SOFC)

by
Babak Ghorbani

M.Sc., University of Tehran, 2015

B.Sc., University of Tehran, 2012

Thesis Submitted in Partial Fulfillment of the
Requirements for the Degree of
Doctor of Philosophy

in the
School of Mechatronic Systems Engineering
Faculty of Applied Sciences

© Babak Ghorbani 2021
SIMON FRASER UNIVERSITY
Spring 2021

Copyright in this work rests with the author. Please ensure that any reproduction or re-use is done in accordance with the relevant national copyright legislation.

Declaration of Committee

Name: Babak Ghorbani

Degree: Doctor of Philosophy

Thesis title: Modeling and Diagnosis of Solid Oxide Fuel Cell (SOFC)

Committee:

Chair: Helen Bailey
Lecturer, Mechatronic Systems Engineering

Krishna Vijayaraghavan
Supervisor
Associate Professor, Mechatronic Systems Engineering

Erik Kjeang
Committee Member
Professor, Mechatronic Systems Engineering

Flavio Firmani
Committee Member
Senior Lecturer, Mechatronic Systems Engineering

Mohammad Narimani
Examiner
Lecturer, Mechatronic Systems Engineering

Nima Atabaki
External Examiner
Associate Professor, Mechanical Engineering
University of British Columbia

Abstract

The development of mathematical models and numerical simulations is crucial to design improvement, optimization, and control of solid oxide fuel cells (SOFCs). The current study introduces a novel and computationally efficient pseudo-two-dimensional (pseudo-2D) model for simulating a single cell of a high-temperature hydrogen-fueled SOFC. The simplified pseudo-2D model can evaluate the cell polarization curve, species concentrations along the channel, cell temperature, and the current density distribution. The model takes the cell voltage as an input and computes the total current as an output. A full-physics three-dimensional model is then developed in ANSYS Fluent, with a complete step-by-step modeling approach being explained, to study the same cell with the identical operating conditions. The 3D model is validated against the other numerical and experimental studies available in the literature. It is shown that although the pseudo-2D solution converges significantly faster in comparison with the 3D case, the results of both models thoroughly match especially for the case of species distributions. The simplified model was then used to conduct sensitivity analysis of the effects of multi-physiochemical properties of porous electrodes on the polarization curve of the cell. A systematic inverse approach was then used to estimate the mentioned properties by applying the pattern search optimization algorithm to the polarization curve found by the pseudo-2D model. Finally, nine different input parameters of the model were changed to find the hydrogen distribution for each case, and a huge dataset of nearly half a million operating points was generated. The data was successfully employed to design a novel classifier-regressor pair as a virtual hydrogen sensor for online tracking of hydrogen concentration along the cell to avoid fuel starvation.

Keywords: SOFC; pseudo-2D; 3D; parameter estimation; diagnosis; machine learning

*To my family for their
unconditional support, love, and
encouragement. I love you more
than anything in the world.*

Acknowledgements

I would like to express my deep gratitude towards all the amazing people who made accomplishing this dissertation possible and enjoyable for me. My special thanks go to my senior supervisor at Simon Fraser University (SFU), Dr. Krishna Vijayaraghavan for his great support and guidance throughout my Ph.D. studies, as well as my colleagues and friends at the “Advance nonlinear control laboratory for clean energy technology”.

I would like to thank my committee members Dr. Kjeang and Dr. Firmani for their valuable comments and suggestions on my candidacy report as well as their guidance on the final thesis draft. I also would like to thank my examiners Dr. Atabaki and Dr. Narimani for evaluating my thesis and providing me with their valuable comments.

I would like to also thank Ballard corporation for giving me the opportunity to work at Ballard for one year, where I gained invaluable experience working with different PEMFC stacks and conducting electrochemical impedance spectroscopy.

Finally, I would like to express my gratitude to my Mom, who always provided me with her endless support and love in all stages of my personal life and professional career.

Table of Contents

Declaration of Committee	ii
Abstract	iii
Dedication	iv
Acknowledgements	v
Table of Contents	vi
List of Tables	viii
List of Figures	ix
List of Acronyms	xi
List of Parameters	xii
Chapter 1. Introduction	1
1.1. Background and Motivation	1
1.2. Objectives and Research Roadmap	3
1.3. Scholarly Contributions	5
1.3.1. Directly Related Contributions	5
1.3.2. Other Contributions	5
Chapter 2. Literature Review	7
2.1. Summary of Previous Review Studies on SOFCs	7
2.2. Software-based Modeling of SOFCs	9
2.3. Simplified Models	11
2.4. Parameter Estimation Using Inverse Approaches for SOFCs	12
2.5. Machine Learning Algorithms for Degradation Modeling of SOFCs	13
2.5.1. Motivation for Using Machine Learning	13
2.5.2. Implementation of ANN for Studying SOFCs	15
2.6. Extending the state of the art	18
Chapter 3. SOFC Model Development	20
3.1. Pseudo-2D Model	20
3.2. 3D Model	30
3.3. Material Selection	34
3.4. Validation of the Mathematical Model	35
Chapter 4. Parameter Estimation Using Inverse analysis	41
4.1. Inverse Problem Formulation	41
4.2. The Sensitivity of the Polarization Curve with Respect to Individual Unknown Parameters	45
4.3. Optimal Parameter Estimation Results	49
Chapter 5. Virtual Hydrogen Sensor Development Formulation	56
5.1. Data Generation	56
5.2. Data Preprocessing	57
5.3. Data Classification Task: Starved vs. Normal Operation	58

5.4.	Data Regression Task: Percentage of the Cell Starved	62
5.5.	Data Classification and Regression Results	64
5.5.1.	Classification Results	64
5.5.2.	Regression Results	67
5.5.3.	Effect of Misclassified Data Input	69
5.5.4.	Validation of the Virtual Sensor	70
Chapter 6.	Conclusion	72
Chapter 7.	Recommendations for future works	75
7.1.	Developing the pseudo-2D model for a button-cell SOFC.....	75
7.2.	Extending the pseudo-2D model for studying the stack dynamic operation.....	75
7.3.	Developing a virtual oxygen sensor for predicting oxygen starvation in PEMFCs	75
References		77
Appendix A.	Equations Used for Finding the Enthalpy of Species	101
Appendix B.	Solution to the Steady State Energy Equation of SOFCs	104

List of Tables

Table 2-1.	Review studies on SOFC components and materials	8
Table 2-2.	Review studies on simplified models for control and diagnosis under both steady-state and transient conditions	9
Table 2-3.	Utilization of Software-based SOFC models in the literature	10
Table 3-1.	Constants for calculation of Gibbs free energy [218]	21
Table 3-2.	The enthalpy constants (valid for $700\text{ }^{\circ}\text{K} \leq T \leq 2000^{\circ}\text{K}$).....	28
Table 3-3.	Different zone types corresponding to the areas shown in Figure 3-4	31
Table 3-4.	Momentum, thermal, species, and electric potential boundary conditions for the boundaries shown in Figure 3-5	32
Table 3-5.	Under-relaxation factors and solver settings for the ANSYS Fluent.....	33
Table 3-6.	Geometry of the cell	35
Table 3-7.	The inlet boundary conditions used for the validation of the study [56], [67], [230]	36
Table 3-8.	Thermophysical and electrochemical properties used for running the validation simulations [56], [67], [230].....	37
Table 4-1.	Electrodes materials and properties for the base case	41
Table 4-2.	Fitness functions previously used for the inverse analysis of SOFCs in the literature	44
Table 4-3.	Summary of results obtained by the inverse analysis for single parameter and multi-parameter estimation of the design variables.....	53
Table 5-1.	Range of different features used for generating the data set	57
Table 5-2.	An example of the raw and standardized data for a random point in the dataset	58
Table 5-3.	Confusion matrix for the classification problem	61
Table 5-4.	Confusion matrix obtained by the Naïve Bayes algorithm.....	64
Table 5-5.	Comparison of performance indicators for different classifiers in detecting incidence of fuel starvation	66
Table 5-6.	Weight matrices of the optimum neural network with nine input neurons, eight neurons in the first hidden layer, and seven neurons in the second hidden layer. HAa corresponds to the Ath neuron in the ath hidden layer.	68

List of Figures

Figure 2-1.	Progress of Ni-Oxidation (seen in yellow) near the outlet due to fuel starvation (used with permission) [171]	14
Figure 3-1.	Schematic of the pseudo-2D model.....	22
Figure 3-2.	Control volume used for solving the energy equation in a single cell	27
Figure 3-3.	The algorithm employed by the pseudo-2D approach for finding the cell temperature, the cell's current, and the reactants' concentrations as a function of cell voltage.....	29
Figure 3-4.	A generic view of the 3D model built in ANSYS Fluent.....	30
Figure 3-5.	Schematic of the boundaries of the 3D cell	32
Figure 3-6.	The step by step procedure required for finding the solution with the 3D model	34
Figure 3-7.	Comparing the polarization curve of the 3D model with those obtained by [56], [67], [230]	38
Figure 3-8.	The average temperature distribution along the cell found by the 3D simulation in ANSYS Fluent	38
Figure 3-9.	The polarization curve for both 3D and pseudo-2D simulations.....	39
Figure 3-10.	(a) Hydrogen, and (b) Oxygen concentration for the counter-flow configuration along the cell obtained by both pseudo-2D and 3D simulations for $I=1.0$ A.....	40
Figure 4-1.	Base case simulation using the pseudo-2D code [65].	42
Figure 4-2.	The algorithm used for finding the unknown parameters using the inverse approach	45
Figure 4-3.	Sensitivity of system response to anode and cathode effective porosity ϕ_a, ϕ_c ($\phi_{a\text{true}} = 0.08$, $\phi_{c\text{true}} = 0.125$)	48
Figure 4-4.	Sensitivity of system response to anode and cathode exchange current density, J_0, a , J_0, c ($J_0, a\text{true} = 7460$, $J_0, c\text{true} = 1000$)	49
Figure 4-5.	Convergence history for the inverse single parameter estimation for different initial estimates	51
Figure 4-6.	Convergence history of the inverse estimation of: (a) J_0, c and ϕ_a ; (b) J_0, c and J_0, a ; (c) J_0, c , J_0, a , and ϕ_a ; (d) J_0, c , J_0, a , ϕ_a , and ϕ_c for three different cases with different initial conditions.....	52
Figure 4-7.	The percentage error in the obtained J_0, c as a function of the percentage deviation from the real J_0, a	55
Figure 5-1.	The neural network used for the classification	61
Figure 5-2.	Schematic of the virtual hydrogen sensor proposed in this study	62
Figure 5-3.	Convergence history of the test set for the regression problem based on MSE	64
Figure 5-4.	Comparison of performance indicators for the KNN with Logistic Regression methods	65
Figure 5-5.	The F1-Score corresponding to the ANN for different number of neurons in each hidden layer	66

Figure 5-6.	The test set accuracy of the ANNr calculated based on the MAE	67
Figure 5-7.	Regression results for “normal” operating points	69
Figure 5-8.	Validation of ANNr based virtual hydrogen sensor.	71

List of Acronyms

ANN	Artificial Neural Network
BCGSTAB	Bi-Conjugate Gradient-Stable Algorithm
CC	Current Collector
CFD	Computational Fluid Dynamics
CHP	Combined heat and power
DMFC	Direct Methanol Fuel Cells
EIS	Electrochemical Impedance Spectroscopy
FEM	Finite element method
FN	False Negative
FP	False Positive
FVM	Finite volume method
GDL	Gas Diffusion Layer
GT	Gas turbine
LSM	Lanthanum Strontium Manganite
MAE	Mean Absolute Error
MSE	Mean Squared Error
MCFC	Molten Carbonate Fuel Cells
MT-SOFC	Micro-tubular solid oxide fuel cell
OCV	Open Circuit Voltage
PAFC	Phosphoric acid fuel cells
PEM	Proton Exchange Membrane
PPV	Positive Predictive Value
ReLu	Rectified Linear Unit Function
SOFC	Solid Oxide Fuel Cell
TN	True Negative
TP	True Positive
TPB	Triple-phase boundary
TPR	True Positive Rate
UDF	User-defined function
UDS	User-Defined Scalar
YSZ	Yttria Stabilized Zirconia

List of Parameters

D	Diffusion coefficient [m^2s^{-1}]
E	Specific total energy [J kg^{-1}]
F	Faraday constant [C mol^{-1}]
G	Gibbs function [J/kmolH_2]
h	Enthalpy [J mol^{-1}] or [J kg^{-1}]
i	Current density [A m^{-2}]
I	Current [A]
\vec{j}	Diffusive flux [$\text{kg m}^{-2}\text{s}^{-1}$]
J	Exchange current density [A m^{-2}]
k	Thermal conductivity [$\text{W m}^{-1}\text{K}^{-1}$]
k_B	Boltzmann Constant [$\text{m}^2 \text{kg s}^{-2}\text{K}^{-1}$]
M	Molecular weight [kmol kg^{-1}]
n	Number of electrons/moles
P	Pressure [Atm]
R	Resistivity [$\Omega \text{ m}$]
S	Source term
T	Temperature [K]
\vec{v}	Vector field [ms^{-1} , ms^{-1} , ms^{-1}]
V	Voltage [V]
X	Mole fraction
Y	Mass fraction
Greek Symbols	
α	Charge transfer coefficient
ϵ	Porosity
ε	Total error
η	Potential loss [V]
γ	Concentration exponent
Ω	Diffusion collision integral
μ	Dynamic viscosity [kg s m^{-1}]
ϕ	Electrical potential [V]
ρ	Density [kg m^{-3}]

σ	Electric conductivity [$\Omega^{-1}\mathbf{m}^{-1}$]
τ	Tortuosity
$\vec{\tau}$	Viscous stress tensor
\forall	Volume [\mathbf{m}^3]
Subscripts and superscripts	
act	Activation
an	Anode
cat	Cathode
D	Diffusion
eff	Effective
ele	Electrolyte
f	Fluid
h	Heat
i	Counter
in	Inlet
j	Counter
jump	Jump condition
m	Mass
ref	Reference condition
s	Solid
w	Weight

Chapter 1.

Introduction

1.1. Background and Motivation

The International Energy Outlook (IEA) report anticipates that by 2040, the global energy demand will increase by more than 25% from current (2018) levels, necessitating investments up to \$2 trillion [1]. The predicted growth in the energy demand would further deplete the energy sources from fossil fuels, entailing the increased utilization of alternative energy sources [2]. Fuel cells (FCs) are one of the most promising technologies for this endeavor as they offer the use of clean and abundant fuel such as hydrogen and higher system efficiency when compared to conventional energy conversion systems [3], [4]. One should note that the terms “clean” and “abundant” used in the literature should be treated carefully. Although burning hydrogen does not come with any harmful biproducts, producing hydrogen might be conducted by utilizing technologies that are not fully clean. Also, hydrogen is fairly abundant on Earth mainly in water form, but it should be transferred into pure hydrogen in order to be properly used. FCs are primarily classified into low-temperature PEMFC ($T < 120\text{ }^{\circ}\text{C}$) and high-temperature SOFC ($T \geq 800^{\circ}\text{C}$). Although PEMFCs are very useful and more widely used in comparison with SOFCs, high-temperature SOFCs offer several advantages over PEMFCs. SOFCs use less expensive catalysts than other types of fuel cells which makes their employment reasonably affordable [5]. Additionally, because of the high operating temperature, the energy in the exhaust is considered “high-quality” energy that can be utilized as a heat source in other energy provision devices such as aircraft, vehicles, steam turbines, stationary gas turbines, Stirling engines, industrial power supplies, and combined heat and power (CHP) systems [6]–[15]. Utilization of the co-generation-based SOFCs will enhance the system's overall electrical efficiency by decreasing their heat-to-power ratio since the great part of heat loss can be recovered through operation in the hybrid mode [16].

There are different cell configurations for SOFCs and the most widely used ones include planar and tubular SOFCs. Tubular SOFCs can be used in series and parallel but they suffer from very long current paths that increases the electrical losses. The focus of

the current study will be on planar SOFCs. A single cell of a planar SOFC consists three main electrodes called anode (fuel), cathode (oxidizer) and the electrolyte (see Figure 3-1). One of these components should be way thicker to provide mechanical support for the cell while the two others should be as thin as possible to maintain electrical transportation losses to a lowest level; planar SOFCs are categorized into anode-supported, cathode-supported, and electrolyte-supported SOFCs based on choice of the thicker component. Since hydrogen transport is much faster than oxygen transport and electrical losses of the electrolyte is considerably high, the best choice for planar SOFCs is the anode-supported configuration.

SOFCs are not without shortcomings. The transient operation of SOFCs might significantly deteriorate the cell performance [17]. This is particularly relevant during the start-up and shut-down when the large changes in temperature can lead to tremendous thermal stresses and ultimately internal fracture and failure due to the thermal expansion mismatch between the cell components [18], [19]. Thermal stress has been widely studied by the literature, and different methods were introduced to reduce the temperature gradient within the cell during the design stages [19]–[22]. More importantly, fuel starvation would occur during the operation if the fuel is consumed at a faster rate than it is fed to the cell [23]. Fatal cell failure due to starvation has been observed in both macro levels and microstructure of the cell [24]. Development of a fast and precise method for promptly identifying the fuel starvation, which is one of the main goals of the current study, extends the SOFCs lifetime, while also increasing their reliability for operating along with other power generation systems.

Significant progress has been made in the experimental, analytical, and numerical modeling of SOFCs. The accuracy of these models relies on understanding the multi-physiochemical phenomena that take place within the cell. This is an onerous task since mass, species, momentum, charge, and energy transfer, as well as the electrochemical equations, must be simultaneously solved in the solid interconnects, fluid zone, and the porous electrodes [25]. Physical experimental setups, on the other hand, are expensive and time-consuming. Furthermore, not all fluid characteristics such as temperature, pressure, velocity, and species distributions are applicably measurable through the cell using experimental techniques. Therefore, developing a fast and precise numerical model is necessary for studying SOFCs in order to overcome the computational burdens and to achieve accurate results validated by experiments. Furthermore, modeling can provide us

with information about distribution of different parameters that are not measurable by experiments, e.g., fuel or oxidant distribution in the catalyst layer.

The development of a numerical model for an SOFC unit requires broad knowledge about different components including the microstructural properties of the porous electrodes. However, the processes included in electrode sintering would provide an overly complicated porous micro-morphology (e.g. dual-scale and functionally graded electrodes [26]–[30]), and there is a notable discrepancy in the observed microstructural properties among different fabrication processes [31]. More importantly, newly discovered catalysts and novel electrode materials are being presented through the literature [32]–[36], necessitating the utilization of a fast and reliable method for evaluating the corresponding porous properties.

Considerably heavy computations are required by the numerical full-physics 3D models [37]. As a result, they would be tedious and impractical to be used in applications such as online control of the cell which requires fast evaluations of the outputs or when implementation in optimization or inverse algorithms with a large number of simulations is required [38]. Two major methods exist for decreasing the overall computation time: reducing the dimension or reducing the physics of the problem. Each of the mentioned approaches owns its own positives and negatives. Hence, one may integrate reduced dimension and reduced physics methods in order to achieve novel, effective, and efficient solutions. Such a model can be utilized not only for cell performance analysis but also for parameter estimation and diagnostic tools development for control proposes. In this thesis, a novel pseudo-2D numerical model is developed and validated against the experimental and numerical works in the literature (chapter 3). Thereafter, the model is utilized to find the multi-physiochemical properties of the cell and (chapter 4) and to generate a huge dataset for designing a virtual hydrogen sensor for fuel starvation detection (chapter 5).

1.2. Objectives and Research Roadmap

The primary goal of this research is developing a fast and computationally-efficient approach for finding the reactants concentration distribution, current density distribution, operating temperature, and polarization curve of a single cell of a high-temperature anode-supported solid oxide fuel cell. The simplified model then will be used for estimating the multi-physiochemical parameters of the electrodes through an inverse approach. Finally,

the model will be employed to generate a huge data set for training a classifier with the objective of detecting both incidence and extent of fuel starvation on the anode side. The following steps should be taken in order to achieve the required results:

- Developing the 3D model of a single cell using ANSYS Fluent SOFC add-on module (see Figure 3-4)
- Validating the 3D results with the available data in the literature (see Figure 3-7)
- Developing the pseudo-2D model of a single cell (see Figure 3-1)
- Comparing the pseudo-2D results with those given by the 3D simulations (see Figure 3-10)
- Conducting a sensitivity analysis on the polarization curve of the cell
- Defining the inverse problem for estimating the unknown parameters
- Conducting the optimization and inverse analysis
- Figuring out if the defined inverse problem can be successfully used for finding unknown parameters.
- Running the simulations using the pseudo-2D numerical model to generate the data required for machine learning.
- Capturing the fuel starvation on the anode side for each data point by using the pseudo-2D model, while generating the data; each data point will be labeled as either starved (1) or normal (0).
- Conducting data pre-processing followed by randomly splitting the data into the training set and the test set.
- Training different classifiers and comparing the results.
- Training an artificial neural network working as a regressor for finding the percentage of the anode active area suffering from starvation.
- Figuring out if the pair of classifier-regressor can be successfully used for capturing the fuel starvation for situations not present in the training set.

1.3. Scholarly Contributions

1.3.1. Directly Related Contributions

- Ghorbani, B., Vijayaraghavan, K., "A review study on software-based modeling of hydrogen-fueled solid oxide fuel cells", *International Journal of Hydrogen Energy*, 44 (26), 13700-13727.
- Ghorbani, B., Vijayaraghavan, K., "3D and simplified pseudo-2D modeling of single cell of a high temperature solid oxide fuel cell to be used for online control strategies", *International Journal of Hydrogen Energy*, Volume 43, May 2018, Pages 9733-9748.
- Ghorbani, B., Vijayaraghavan, K., "A Novel Computationally Efficient Pseudo-2D Approach for Modeling Single Cell of a High-Temperature Solid Oxide Fuel Cell Using Modal Analysis", *ASME 2018 International Design Engineering Technical Conferences and CIEC*, V01AT02A014.
- Ghorbani, B., Vijayaraghavan, K., "An inverse-problem approach: Estimating multi-physiochemical properties of porous electrodes of single cell of a hydrogen-fueled solid oxide fuel cell by applying the pattern-search optimization to a pseudo-2D numerical model", *Journal of Power Sources*, Volume 448, Feb 2020, 227437.
- Ghorbani, B., Vijayaraghavan, K., "Developing a virtual hydrogen sensor for detecting fuel starvation in solid oxide fuel cells using different machine learning algorithms", *International Journal of Hydrogen Energy*, 45(51), Oct 2020, Pages: 27730-27744.

1.3.2. Other Contributions

- Ghorbani, B., Ebrahimi S., Vijayaraghavan, K., "CFD Modeling and Sensitivity Analysis of Heat Transfer Enhancement of a Ferrofluid Flow in the presence of a Magnetic Field", *International Journal of Heat and Mass Transfer* 127, Pages 544-552.
- Ebrahimi, S., Ghorbani, B., Vijayaraghavan, K., "Optimization of catalyst distribution among PEMFC channel through a numerical two-phase model and genetic algorithm", *Journal of Renewable Energy*, Volume 113, December 2017, Pages 846-854.

- Ghorbani, B., Akhavan-Behabadi, M., Ebrahimi, S., Vijayaraghavan, K., "Experimental investigation of condensation heat transfer of R600a/POE/CuO nano-refrigerant in flattened tubes", *International Communications in Heat and Mass Transfer*. Vol 88, Nov. 2017, 236-244.
- Ghorbani, B., Kowsary, F., Ebrahimi, S., Vijayaraghavan, K., "CFD Modeling and optimization of a latent heat storage unit for running a solar assisted single effect Li-Br absorption chiller using multi-objective genetic algorithm", *Journal of Sustainable Cities and Society*, Volume 34, October 2017, Pages 321-334.
- Karimi, D., Ghorbani, B., Momen, M., "Net zero energy buildings in semi-arid climates: An analysis on three case studies in Tehran, Iran", *Energy Equipment and Systems*, 8(2), 169-178.

Chapter 2.

Literature Review

This chapter aims to provide a review of the literature relevant to the objectives discussed in section 1.2. This chapter aims to highlight both the key results and the shortcoming of past literature to motivate the need for this thesis. This chapter has been arranged as follows: the review surveys on SOFCs modeling are presented in section 2.1; a review of the two most common software-based SOFC models as well as related developed simplified models through sections 2.2 and 2.3, respectively; literature on optimizing the inverse problem (“inverse techniques”) for parameter estimation in SOFCs are presented in section 2.4; a review of utilization of machine learning algorithms for SOFCs will be presented after a brief introduction to the fuel starvation and the way this phenomenon might affect the SOFC performance in section 2.5.

2.1. Summary of Previous Review Studies on SOFCs

Numerical modeling of SOFCs is utilized for design optimization as well as the development of control strategies. Therefore, there is extensive research on different aspects of SOFC modeling. Researchers have mentioned different SOFC materials [39], operating principles and thermodynamics of electrodes and electrolyte materials [40], and SOFC degradation phenomena [41], as well as modeling [42], control, and diagnosis of SFOCs [37]. Table 2-1 summarizes the review studies on SOFC components and materials while Table 2-2 mentions review studies on simplified models for control and diagnosis of SOFCs operating under both steady-state and transient conditions.

Table 2-1. Review studies on SOFC components and materials

Reference	Summary
Badwal and Foger (1994) [40]	Research Overview: <ul style="list-style-type: none">➤ Operating principles and thermodynamics of SOFCs➤ Electrodes and electrolyte materials➤ Fabrication methods Conclusions: <ul style="list-style-type: none">➤ Change of morphology of the cathode layer with time and decrease in cathode active area during operation limit the life of SOFCs and need to be minimized
Jiang and Chan (2004) [43]	Research Overview: <ul style="list-style-type: none">➤ Development of Ni/Yttria-stabilized zirconia (YSZ) cermet anodes (detailed)➤ Modified Ni/YSZ cermet anodes (detailed)➤ Microstructure optimization of materials➤ Alternative and conductive oxide anodes➤ Anode supported substrate materials Conclusions: <ul style="list-style-type: none">➤ The electrochemical performance of Ni/YSZ anodes might be improved by substituting YSZ with mixed ionic and electronic conductors.➤ Anode-supported cells possess higher normalized power density
Laosiripojana et al (2009) [39]	Research Overview: <ul style="list-style-type: none">➤ A brief review of cell materials Conclusions: <ul style="list-style-type: none">➤ YSZ, porous Ni/YSZ cermet, and perovskite-based LaMnO_3 are the most common materials used for electrolyte, anode, and cathode, respectively.
Molenda et al. (2017) [44]	Research Overview: <ul style="list-style-type: none">➤ Novel electrolyte/electrode materials➤ Novel fabrication techniques➤ Metal supported SOFCs➤ Metallic interconnects for SOFCs Conclusions: <ul style="list-style-type: none">➤ Increasing the cell efficiency and lowering the manufacturing costs of individual cells/stacks are reported as the focus of the ongoing researches on SOFCs.

Table 2-2. Review studies on simplified models for control and diagnosis under both steady-state and transient conditions

Reference	Summary
Bavarian et al (2010) [42]	Research Overview: <ul style="list-style-type: none"> ➤ 3D, 2D, 1D, and 0D modeling of SOFC ➤ Dynamic and steady-state behavior of SOFC ➤ Multi-time-scale modeling of SOFC ➤ Control objectives, control strategies, actuators, and sensors Conclusions: <ul style="list-style-type: none"> ➤ The slowest and the fastest response in an SOFC correspond to thermal and electronic processes, respectively. ➤ A perfect model is the one including only necessary details rather than taking into account all complexities.
Wang et al (2011) [37]	Research Overview: <ul style="list-style-type: none"> ➤ 3D, 2D, 1D, and 0D models for control and diagnosis (detailed) Conclusions: <ul style="list-style-type: none"> ➤ 0D and 1D models show the greatest potential to be used for real-time simulations. ➤ The flexibility of grey-box models makes it possible to obtain the rules describing the cell behavior. ➤ Black-box models based on artificial intelligence are suitable enough for non-linear dynamic modeling.
Barelli et al (2013) [41]	Research Overview: <ul style="list-style-type: none"> ➤ SOFC degradation phenomena (detailed) ➤ Fault detection technologies Conclusions: <ul style="list-style-type: none"> ➤ Identification of specific parameters that can be potentially implemented in diagnostic systems for the detection of failures such as anode re-oxidation caused by fuel starvation is applicable

2.2. Software-based Modeling of SOFCs

Initial CFD modeling employed a “do-it-yourself” approach [45]. However this was quickly supplanted by studies employing commercial CFD software packages [46], [47] consisting of finite volume method (FVM) and finite element method (FEM). The fluid transport is usually modeled by the ANSYS Fluent/CFX using finite volume method (FVM), while the mechanical stress-strain analysis is conducted through ANSYS using finite

element method (FEM) techniques (see Table 2-3). One should note that a very specific step-by-step approach needs to be employed to ensure that the software-based simulations converge. In addition, boundary conditions, solution methods, material properties, thermo-physical properties, electrochemical parameters, meshing, solution controls, and appropriate solver settings need to be carefully tuned. In this thesis, ANSYS Fluent SOFC add-on Module is used to validate the proposed pseudo-2D model. Hence, details on instructions needed to setup SOFC-CFD simulation is presented in section 3.2 (in Chapter 3).

Table 2-3. Utilization of Software-based SOFC models in the literature

Models based on ANSYS	CFD Simulations	Flow analysis by ANSYS CFX		Manifold designs [48]–[55]
		Electrochemistry and flow analysis using either user-defined functions or the SOFC add-on module	Hydrogen-fueled cells	Air/Fuel flow rates [21], [56]–[58]
				Current density distribution [21], [56], [59]–[66]
				Temperature distribution [21], [57], [60], [61], [65], [67], [68]
				Different cross section geometries [55], [59], [61], [69]
				Different flow patterns [21], [54], [56], [61], [70]
				Thermal boundary conditions [56], [58], [63], [65]
				Hydrogen distribution [21], [56], [57], [59]–[61], [65], [67], [69]–[71]
		Carbon/Hydrocarbon-fueled cells	Carbon deposition [72], [73]	
			Steam/carbon ratio [73]–[77]	
			Steam reforming on the anode side [69], [72], [74]–[81]	
			Fuel composition [58], [73]	
			Nickel oxidation [73], [82]	
			Radiation heat transfer effects [58], [68], [79], [82]	
			Imposed thermal stresses [59], [63]	
	FEM simulations	Curvature/Camber analysis [83], [84]		
		Creep behavior [85], [86]		
		Different seal designs [85], [87]–[90]		
		Torsion tests [91]		
		Crack initiation tests [92]		
		Compressive stress tests [86], [93], [94]		
		Cathode contact sintering [72], [94]		
	Simultaneous CFD and FEM analysis		Stack-level thermal stress [78], [90], [95]–[100]	

2.3. Simplified Models

Researchers have been working to improve the convergence speed and to reduce the computation time by simplifying full physics 3D SOFC models [38]. Some researchers have reduced the dimensions of the problem by simplifying the 3D models into 2D models [101]–[103], 1D models [104]–[106], or 0D models [107], while others have assumed that the electrochemical reaction at the triple-phase boundary of the electrolyte shows itself as a voltage jump at the electrode-electrolyte interface [20], [21], [101], [102], [105], [108]–[111]. Although faster, the solution to the model with the reduced dimensions is less accurate than the 3D case. Simplifying the physics of the problem by making some assumptions, although being faster than 3D models, still suffers from some computational burdens and cannot be used for applications such as online control and diagnosis.

The least complicated methods are black box or 0D models which are based on either empirical correlations found by the experimental techniques [112] or treating the fuel cell as a component of a system [113]. 1D models are suitable for both planar [114] and tubular [115]–[117] configurations, taking into account the changes in the flow field only in the direction of the channels. One may note that the employment of 0D and 1D models ignores special variations in one or more direction. The closest results to the 3D cases are found by 2D models with the symmetric boundary condition at the cell axis while studying the performance of tubular SOFCs [118].

There are a couple of studies in the literature that reduced the number of dimensions while simplify the physics of the problem (as has been done in this thesis); the models built using such an approach are recognized as multi-dimensional models [118]. A novel algorithm for mapping the data from the triangular mesh on the surface of a tube to a 1D axial band in ANSYS Fluent was introduced for the first time by Goldin et al. [72]. The coupling algorithm was then utilized by Kattke et al. [119] for the stack modeling and thermal management of SOFCs. The idea was that all the electrochemical equations can be solved within 1D tubes while the 3D flow field outside of the tubes is modeled without simplifying assumptions. Followed by their previous work and using the proposed coupling algorithm [119], Kattke and Braum [82] identified the tubular SOFCs operating strategies, considering effects of system design parameters, thermal interactions between the different components, and interactions between the stack and environment. The studies mentioned thus far, however, were restricted to tubular SOFCs and require a significant

amount of computation because of the 3D effects. In this study, a pseudo-2D model is developed with a 1D mesh in the direction of the cell channels that takes into account the change of parameters in the axial direction as well as the energy equation, while not ignoring the change in species concentrations in the direction perpendicular to the channel length. The method is developed to increase the computation efficiency while keeping the accuracy in an acceptable range.

2.4. Parameter Estimation Using Inverse Approaches for SOFCs

Since there are several uncertain parameters in the SOFCs, there has been a concerted endeavor to characterize SOFCs and to expand the scope of parameter estimation. At the macro-level, scientists have investigated the cell dynamic response [120]–[123], stack configurations [124]–[126], fuel/air flow rate [21], [57], [58], cell geometry [50]–[52], [55], and AC impedance diagnosis techniques [127]–[129]. On the micro-level perspective, researchers have studied SOFC micro-catalytic reaction mechanisms [130]–[133] and cell materials [134]–[136] and attempted to optimize the microstructure of the electrodes [137]–[139]. One may find even more complicated models that use different tools such as spherical particle random packing system and percolation theory to directly determine electrodes' fundamental properties such as pore size, particle diameter, porosity, and tortuosity [140]–[144]. The focus of the so-called “direct/forward” techniques is on either investigating the cell performance when system geometry and cell properties are known or developing empirical relations for evaluating the cell properties using experimental micro-modeling analysis. On the other hand, one may analyze the cell response and pose a so-called “inverse” problem to iteratively determine single or multiple properties. Convergence to a unique solution when using an inverse method is much more complicated in comparison with the direct counterpart (i.e. the forward methods) since inverse problems are mathematically ill-posed [145], [146]. Also, the inverse analysis is potentially time-consuming because multiple forward simulations or experiments are required to formulate the inverse solution [147], [148]. In order to overcome existing computational burdens, optimization techniques can be employed by the inverse techniques [149]–[151].

There are a few studies in the literature employing inverse analysis for determining the SOFC electrode properties, the cell operating conditions, or the optimized system

geometry. Sarmah et al. [152] utilized a differential evolution-based inverse algorithm to estimate operating parameters of a hybrid SOFC/GT/ST power plant. Shi and Xue [153] used particle swarm optimization technique to estimate anodic and cathodic reference exchange current densities in a button-cell SOFC. Gogoi and Das [154] evaluated current density, pressure, and fuel flow rate of an internal reforming SOFC using the inverse simplex search method. For the inverse analysis to work, a fitness function must be employed as the difference between “a selected system output obtained by random values of the unknown variables” and “the corresponding required values”. Various fitness functions are introduced by different studies, depending on the forward model capabilities. Looking at few existing studies, it is concluded that there are no works in the literature including a systematic approach for the evaluation of the electrode properties and anodic/cathodic exchange current density of planar SOFCs. In this study, we are going to find the mentioned properties by only using the cell performance data without knowing the electrodes morphology.

2.5. Machine Learning Algorithms for Degradation Modeling of SOFCs

2.5.1. Motivation for Using Machine Learning

A typical SOFC is made of solid yttria-stabilized zirconia (YSZ) electrolyte sandwiched between two porous electrodes. The electrochemical performance of the cell is significantly influenced by the microstructure morphology of the electrodes [24]. To reach the commercialization stages, SOFCs are required to demonstrate 40000 hours of safe operation which necessitates the utilization of approaches for avoiding cell degradation [155], [156]. The real operation of SOFCs might significantly deteriorate the cell performance [17], and this has prevented wide scale adoption of SOFCs [157]. For example, temperature changes that occur during the start-up and shut-down coupled with the thermal expansion mismatch between the cell components result in tremendous thermal stresses and ultimately internal fracture leading to failure [18], [19], [158]. Thermal stress arising from mismatched coefficients of thermal expansion has been widely studied [90], [159], and different designs and methods have been proposed in the literature to reduce the temperature gradient within the cell [19]–[22], [160]. More importantly, fuel starvation would occur during the transient operation if the fuel is consumed at a faster rate than it is fed to the cell [23]. This results in Ni oxidation on the anode side and cell

destruction [24], [161]. Fatal cell failure due to starvation and the ensuing Ni oxidation [162] has been observed in both macro levels and microstructure of the cell [163], [164]. Ni oxidation is exceptionally detrimental, especially at higher current densities where fuel starvation is more likely to happen [165]. Figure 2-1 shows the progress of Ni-Oxidation near the cell outlet. Performance of all SOFC systems can deteriorate as a direct result of fuel starvation [166] regardless of the specific SOFC configuration [167]. It is fundamentally burdensome to assess internal characteristics of SOFCs [168]. Hence, development of a fast and precise method for promptly identifying the fuel starvation during the operation extends the SOFCs lifetime, while also increasing their reliability for operating along with other power generation systems [169]. It may be noted that SOFCs use excess air for controlling their temperature, and oxygen starvation is typically not a concern [170].

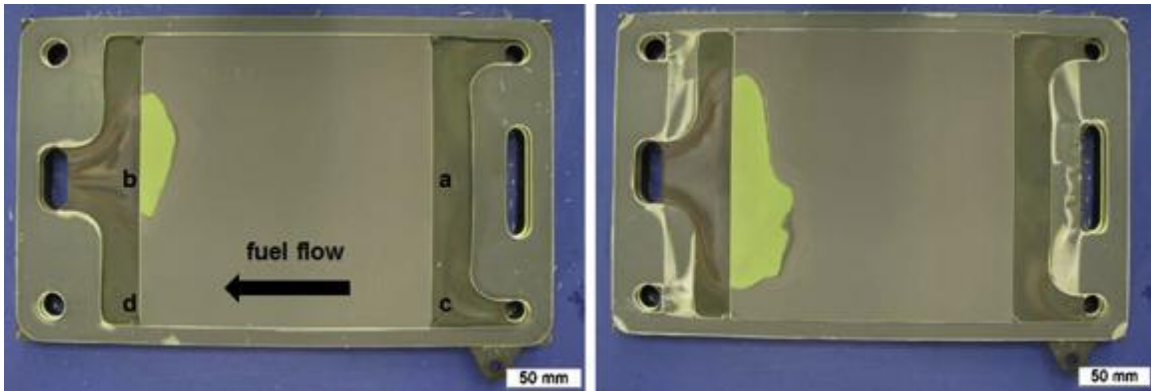


Figure 2-1. Progress of Ni-Oxidation (seen in yellow) near the outlet due to fuel starvation (used with permission) [171]

There have been several past attempts to prevent fuel starvation. Finding the hydrogen concentration along the anode channels is a determining factor for detecting local fuel starvation and subsequently avoid destructive Ni oxidation of the anode [172]. Once Ni particles are oxidized to NiO they go through more than 50 percent increase in volume, and this will result in mechanical failure of the thin electrolyte especially for the case of anode-supported SOFCs. A complete review on detrimental mechanisms resulted by Ni oxidation is provided by Faes et al. [173]. Many researchers have modified the inlet fuel manifolds to ensure that an equal amount of hydrogen is fed to all cells [48]–[53]. These studies rely on computational fluid dynamics (CFD) to find the hydrogen mole fraction along the cell. A similar CFD simulation could be employed in this work to model fuel starvation. However, CFD simulations are not suitable for online control or diagnosis

since they require a significant amount of time to converge to the solution. On the other hand, finding hydrogen distribution and predicting local fuel starvation is a very difficult task during experimental investigations because of the technical barriers [172]. Fortunately, artificial intelligence-based black-box models are reported to be extremely useful for modeling non-linear systems [174]. Artificial neural networks (ANNs) are particularly valuable for extracting black-box models from large datasets, thanks to their ability to provide a very fast response once the network is trained [175]. ANNs are shown to have a great potential for monitoring and controlling purposes [176]. ANNs are capable of modeling different manufacturing processes to reduce development costs [177]. ANNs have been even used in earlier literature to study proton exchange membrane fuel cells (PEMFCs) [178]–[180], direct methanol fuel cells (DMFCs) [181]–[185], molten carbonate fuel cells (MCFCs) [186]–[190], phosphoric acid fuel cells (PAFCs) [191], and fuel cell-based combined heat and power (CHP) systems [192]. The following sub-section reviews the application of ANN for SOFC modeling. In addition to ANN, some other classification methods including K-nearest neighbor (KNN) are employed and compared in this thesis. It may be noted that while KNN method is a popular machine learning technique that has been used to classify systems, there is no earlier literature on the application of KNN to SOFCs.

2.5.2. Implementation of ANN for Studying SOFCs

An ANN consists of an input layer of neurons that is connected to an output layer either directly or through single/multiple hidden layers. ANNs provide us with rapid calculating models by learning from the data obtained by either experiments or simulations [193]. Marra et al. [194] used an ANN with only one hidden layer containing five neurons to predict the operating voltage of a disk-shaped methane-fueled electrolyte-supported SOFC stack as a function of average current density, anode mass flow rate, cathode mass flow rate, anode inlet temperature, and time. The training data was experimentally generated by running a stack at constant load for 1000+ hours allowing for stack degradation effects to be indirectly considered. Milewski et al. [195], [196] developed a single layer ANN with one to three inputs and two to five neurons to determine whether the influences of different parameters on the cell voltage can be successfully modeled using a neural network. Their model deviated from the experimental data for low hydrogen content and low anode porosity. Razbani and Assadi [197] trained an ANN consisting of

one hidden layer with eleven neurons using their previous experimental data [198]. The ANN had current, flow rate, and air temperature as input parameters, and the voltage and temperature at five different locations as the output. The ANN model was constrained by the experimental data only available at open circuit condition (no load). The authors have themselves recommended several improvements to their work such as using more data points, choosing a better test set, increasing the range of input parameters, decreasing the number of neurons in the hidden layer, and representing only temperature at the output layer [197]. Notwithstanding the drawbacks associated with their model, Razbani and Assadi [197] introduced the concept of “estimating the temperature profile within the stack using an ANN” which is a valuable outcome.

Tafazoli et al. [199] developed and optimized a neural network for finding the triple-phase boundary density, particle contact surface density, and gas diffusion factors as a function of backbone porosity, backbone axial and transversal grow rates, and particle loading. Their ANN was successfully used to investigate the effects of backbone geometric anisotropy on the performance of infiltrated SOFC electrodes. Two hidden layers, each containing one to thirty nodes, were used to optimize the neural network. It may be noted that, this approach would have required training 900 neural networks to determine the one with the best performance; this was likely only possible in Tafazoli et al. [199] due to the very small training and test sets. Fuad and Hussain [200] compared the performance of artificial neural network, support vector machine, fuzzy inference system, and genetic programming in estimating the SOFC outlet temperature and the operating voltage as a function of air temperature, air flow rate, fuel utilization, and load current. 1000 input datapoints obtained by a previously validated numerical method were used for training each regressor, and it was shown that the artificial neural network possesses the best performance.

ANNs have also been utilized by researchers for optimization purposes. Bozorgmehri and Hamed [201] trained an ANN model of a SOFC using 632 experimental data points. The ANN had only one hidden layer with four neurons and a hyperbolic tangent sigmoid transfer function. Current density, temperature, electrolyte thickness, anode thickness, anode porosity, and cathode thickness were chosen as input variables of the ANN with the cell voltage as the output. The accuracy of the test set was shown to be more than 99 percent. After training the ANN, the genetic algorithm was used, with the network inputs as the design variables, to maximize the power output. Nassef et al. [202]

applied the radial movement optimizer (RMO) to an ANN model to find a set of input parameters that maximizes the power output. The optimized set of design variables found by RMO was compared with the ones previously obtained by the Genetic Algorithm and experimental setups, and it was shown that the proposed optimizer outperforms the other methods by a small margin. The model was trained using 538 data points with current density, temperature, electrolyte thickness, anode thickness, anode porosity, and cathode thickness as input variables of the ANN and the cell voltage as the output. The accuracy of the test-set calculated using mean squared error (MSE) was found to be 0.9975, which is unacceptably higher than the accuracy of the training-set. More recently, Le et al. [203] developed an ANN with one hidden layer with five neurons to evaluate the cell voltage of a single-chamber SOFC as a function of operating temperature, current, and sintering temperature. While they reported an accuracy of 0.999 for the test-set, the paper was missing details regarding the training data such as the number of data points. Wu et al. [204] trained a radial basis function (RBF) neural network using a genetic algorithm in MATLAB. Only two input variables, the current and temperature, were used to evaluate the cell voltage using two groups of V-I data at 800 °C and 1000 °C. Tang and Huang [205] used a support vector regression machine (SVRM) to find the anode electrical conductivity of LSCM-xCu composite as a function of operating temperature and Cu content. The SVRM was shown to be capable of generalizing the results for the test set. However, a very small size of 32 and 4 were chosen for the training set and the test set, respectively. Chaichana et al. [206] estimated the current density of a direct internal reforming SOFC as a function of temperature, water mole fraction, hydrogen mole fraction, and cell voltage using a novel hybrid neural network with two hidden layers.

It is also possible to train the ANN or other regressors/classifiers using the data generated by numerical simulations. One of the earliest ANN models of SOFCs was developed by Arriagada et al. [207]. It was shown that the data obtained by a validated numerical model can be successfully used for training a neural network and ultimately predicting the system performance [207]. Zamaniyan et al. [208] trained an ANN using the data obtained by a numerical scheme to study the performance of a generic industrial hydrogen plant. They found the optimum number of neurons in the hidden layer by minimizing the MSE and using the elbow method. Ogaji et al. [209] modeled fuel cell performance using three different four-layer neural networks with two hidden layers. Temperature, voltage, power output, and efficiency were estimated as a function of

operating pressure, current density, fuel/air utilization factors, and fuel/air temperature. All the data used for training the network was obtained by numerical modeling. In a very recent work published by Yan et al. [210], an ANN was trained to predict the cathodic overpotential and degradation rate of SOFC electrodes as a function of microstructure of the cell including particle size, particle size distribution (PSD), and pore content. 770 different data points were numerically generated using the discrete element method (DEM). Multi-objective genetic algorithm was then applied to the ANN model to minimize the cathodic overpotential and the electrolyte degradation rate.

2.6. Extending the state of the art

To the best of the author's knowledge, there is no past literature on the diagnosis of the extent of fuel starvation in SOFCs by applying machine learning algorithms. Furthermore, there is a gap in the literature on estimating the morphological properties of the electrodes in planar SOFCs using an inverse analysis applied to the polarization curve. Working in these areas, however, needs accurate and fast computational models. In this research, a numerical model is developed and validated against other numerical and experimental studies. Thereafter, the model is utilized for estimating the morphological properties of the SOFC electrodes using an inverse analysis. Additionally, this study evaluates multiple machine learning techniques for their ability to predict the incidence and the extent of hydrogen starvation. Technically, it is also impossible to find out local hydrogen distribution and by virtue the extent of starvation within the cell using experimental techniques. In this study, a model previously validated by Ghorbani et al. [65], [211], [212] is used to generate the dataset required for the machine learning algorithms. In SOFCs, we control and vary the cell voltage, the inlet temperature, cathode pressure, the hydrogen and oxygen mole fractions and the anode and cathode molar flow rates for each individual fuel cell. We would also need to consider the variations in the cell active surface area, anode effective porosity, and cathode effective porosity (both can be estimated by the inverse analysis of a given experimental polarization curve) during manufacturing [211]. Since it is desirable to have a single model that could be used for any combination of the above parameters, the training data needs to be appropriately generated by varying all of them. The authors choose to generate a dataset consisting of 480,000 data points (refer section 5.1 for details). The generation of such huge amount of data is made possible by the computationally-efficient numerical model. The generated

data is then utilized to train different classifiers including Logistic Regression, K-Nearest Neighbors, Naïve Bayes, and ANN to label the cell as either “normal” or “starved”. When a cell is labeled as “starved”, another artificial neural network is used (this time for regression) to predict what percentage of the cell active area is starved. The current work also expands past approaches by studying the effect of varying the number of neurons in each of two hidden layers. It should be noted that setting the number of neurons in hidden layers to values considerably higher than the number of inputs is not recommended (as a rule of thumb) because of the possibility of overfitting the model to the data [213]–[215]. The proposed model acts as a virtual hydrogen sensor placed within a single cell of a hydrogen-fueled SOFC. Different algorithms for the classification problem are applied and the best algorithm with optimized parameters for both classification and regression problems are reported in the end.

Chapter 3.

SOFC Model Development

In this chapter, the steady-state performance of a single cell of an anode-supported high-temperature SOFC is studied by using a novel and computationally efficient pseudo-2D approach and the results are validated against a full physics 3D model developed in ANSYS Fluent. In the end, both models are validated against the experimental and numerical data available in the literature. In the following sections, steady-state governing equations are presented for the pseudo-2D model followed by a brief explanation of the 3D model and validation of the results against the literature. Furthermore, the pseudo-2D model was used in this work to conduct the parameter estimation using the inverse approach and also to generate data for developing the virtual hydrogen sensor using a novel classifier-regressor pair. All the above-mentioned tasks will be formulated in this chapter.

3.1. Pseudo-2D Model

The pseudo-2D model for studying the SOFC operation is provided in this section. The main purpose of developing such a model is to find the reactants concentrations along the air/fuel channels as well as the SOFC polarization curve and cell temperature. The schematic of the model is illustrated in Figure 3-1. The method is called pseudo-2D because the effect of reactants transport through the porous GDL in the direction perpendicular to the channels is taken into account while using a 1D mesh in the axial direction, i.e. the numerical domain is segmented into elements of different size along the channel with the transport equations being solved analytically in the normal direction. According to Figure 3-1, the very thin TPB layers and electrolyte are lumped into a surface called the electrolyte surface. Fuel and air streams diffuse through the GDL until they reach the electrolyte surface where the following electrochemical reactions occur at the anode and the cathode sides, respectively:





And the overall reaction will be:



With the number of electrons transferred per mole of fuel $n = 2$. The electrochemical model developed in this work is based on the computation of the local thermodynamically reversible potential known as Nernst potential at the operating temperature T [216]:

$$V_{\text{Nernst}} = \frac{-\Delta G_0}{nF} - \frac{R_g T}{nF} \ln \left[\prod_i (p_i/p_{\text{ref}})^{v_i} \right] \quad \text{Eq. (3)}$$

Where, p_i is the reactants partial pressure, R_g represents the universal gas constant, and F is the Faradays constant, and reference pressure is equal to 1 atm. ΔG_0 is the Gibbs free energy corresponding to the maximum reversible cell voltage that is achievable for the cell. Many studies have used constant values for the Gibbs free energy of the reaction. However, it is shown that this value is a function of temperature [217]. The following function which is used by ANSYS Fluent libraries [218] is utilized for computing ΔG_0 in this thesis with the constants presented in Table 3-1:

$$\Delta G_0 = -a - bT - cT^2 - dT^3 + eT \ln(T) \left(\frac{J}{K \cdot \text{mol } H_2} \right) \quad \text{Eq. (4)}$$

Table 3-1. Constants for calculation of Gibbs free energy [218]

Parameter	Value
a	1.192684 E05
b	15.950548
c	9.909308 E-04
d	9.198735 E-08
e	5.786936

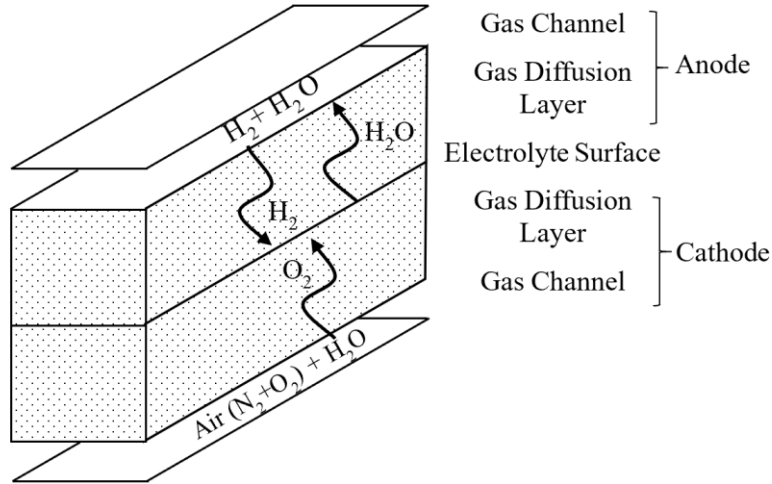


Figure 3-1. Schematic of the pseudo-2D model

The open-circuit voltage, i.e. the electric potential when no current is drawn from the system, is not practically equal to the Nernst voltage because of the cross-over of the charges through the membrane. This is especially the case for low and moderate temperature fuel cells. However, for SOFCs the cross-over is negligible which equalizes the open-circuit voltage and Nernst potential. However, after connecting the fuel cell to an external load the current flows through the cell which results in different modes of voltage loss within the system. As a result, the operating voltage drops to lower values according to the following formula:

$$V_{\text{cell}} = V_{\text{Nernst}} - (\eta_{\text{act}} + \eta_{\text{ohm}} + \eta_{\text{conc}}) \quad \text{Eq. (5)}$$

The η parameters appeared in the Eq. (5) are called cell polarization or cell overpotentials. It should be noted that the open circuit voltage (OCV) which is defined as the actual cell voltage at no load condition is assumed to be the same as the Nernst voltage. If there is electrons cross-over along the electrolyte, a small reduction from the Nernst voltage should be considered when using Eq. (5). There are three main sources of voltage loss inside an SOFC: activation polarization, ohmic polarization, and concentration polarization.

The activation polarization is the result of the inevitable irreversibilities in the electrochemical reactions. When current is drawn from the system, the cathode potential reduces to help the reduction reaction occur, while the anode potential increases to facilitate the oxidation reaction. This phenomenon results in a general decrease in the

operating voltage which is the difference between the electrodes potentials. The activation polarization can be computed using the following equation which is the implicit form of Butler-Volmer equation [216]:

$$i = i_0 \left[\exp \left(\beta \frac{nF}{R_g T} \eta_{act} \right) - \exp \left(-(1 - \beta) \frac{nF}{R_g T} \eta_{act} \right) \right] \quad \text{Eq. (6)}$$

i_0 is called the exchange current density which denotes the value of current exchange at equilibrium. Note that the n , which is a non-integer parameter, in the Butler-Volmer equation is different from the n that appears in the Nernst equation, and corresponds to the number of electrons transferred in the elementary reaction. Parameters βn and $(1 - \beta)n$, sometimes shown with α_a and α_c , are called the anodic and cathodic charge transfer coefficients. Charge transfer coefficients indicate what percentage of the activation potential goes toward the oxidation and reduction reactions at each electrode. In case of having equal anodic and cathodic charge transfer coefficients at the electrode surface, which is an acceptable assumption for high-temperature SOFCs, the Butler-Volmer equation can be re-written into its explicit form and the activation polarization at each electrode can be directly calculated:

$$\eta_{act} = \frac{R_g T}{\alpha F} \sinh^{-1} \left(\frac{i}{2i_0} \right) \quad \text{Eq. (7)}$$

Eq. (7) is used for finding the activation polarization on both electrodes. It should be noted that different values of α and i_0 are used for anode/cathode. Exchange current density for the electrodes is found using the following set of equations:

$$i_{0,c} = \gamma_c \left(\frac{p_{O_2}}{p_{O_2,ref}} \right)^{0.25} \exp \left(- \frac{E_{act,c}}{R_g T} \right) \quad \text{Eq. (8)}$$

$$i_{0,a} = \gamma_a \left(\frac{p_{H_2}}{p_{H_2,ref}} \right) \left(\frac{p_{H_2O}}{p_{H_2O,ref}} \right) \exp \left(- \frac{E_{act,a}}{R_g T} \right) \quad \text{Eq. (9)}$$

The ohmic polarization is another mode of voltage loss for SOFCs and accounts for the majority of the losses inside the cell. The current requires a voltage gradient to pass

through the cell by means of conduction, so part of the cell voltage goes towards driving the electrons and ions through the cell. The charges also encounter electric/ionic resistance through their path. Different parts of the SOFC possess different electronic conductivity. The electrolyte, however, is ionic conductive. The ohmic polarization is found using the ohm law:

$$\eta_{ohm} = R_{ohm} iA \quad \text{Eq. (10)}$$

The ohmic resistance of the planar cell is calculated using the following equation:

$$R_{ohm} = \frac{t_a}{\sigma_a A} + \frac{t_e}{\sigma_e A} + \frac{t_c}{\sigma_c A} \quad \text{Eq. (11)}$$

Where,

$$\sigma_a = \frac{9.5 \times 10^7}{T} \exp\left(-\frac{1150}{T}\right) \quad \text{Eq. (12)}$$

$$\sigma_c = \frac{4.2 \times 10^7}{T} \exp\left(-\frac{1200}{T}\right) \quad \text{Eq. (13)}$$

$$\sigma_e = 33.4 \times 10^3 \exp\left(-\frac{10300}{T}\right) \quad \text{Eq. (14)}$$

It is assumed that the electronic resistivity of the current collectors and the contact resistance between the current collectors and the electrodes are negligible.

The concentration of species in the vicinity of the electrolyte is different from the corresponding values at the gas channels (bulk concentration) because of the diffusion limitations inside the porous electrodes and this results in a further decrease in the cell voltage known as concentration loss. As mentioned earlier, the Nernst voltage is calculated based on the reactants partial pressure inside the channels. However, the real value of the maximum available voltage must be calculated using the concentrations at the reaction zones. Writing down the Nernst equation based on the partial pressures at the electrolyte surface and subtracting the result by the original version of the Nernst equation gives the concentration polarization of the cell:

$$\eta_{\text{conc}} = -\frac{R_g T}{nF} \ln \left(\frac{p_{\text{H}_2}^* p_{\text{H}_2\text{O}}^0}{p_{\text{H}_2}^0 p_{\text{H}_2\text{O}}^*} \right) - \frac{R_g T}{nF} \ln \left(\frac{p_{\text{O}_2}^*}{p_{\text{O}_2}^0} \right)^{0.5} \quad \text{Eq. (15)}$$

The superscript “*” denotes the partial pressure at the reaction zone while the superscript “0” corresponds to the partial pressure at the channel. In order to find a relation between the bulk and reaction molar fractions, the one-dimensional Fick’s 1st law of diffusion is utilized:

$$\dot{N}_i = -D_i \frac{dc_i}{dy} + X_i \sum_j \dot{N}_j \quad \text{Eq. (16)}$$

Where, D_i is the diffusion coefficient of the species i , X_i denotes the mole fraction, \dot{N}_i is the molar rate, and y is the direction perpendicular to the electrolyte surface. For the hydrogen:

$$\dot{N}_{\text{H}_2} = -\frac{PD_{\text{H}_2}^{\text{eff}}}{R_g T} \frac{d(X_{\text{H}_2})}{dy} \quad \text{Eq. (17)}$$

Note that $\dot{N}_{\text{H}_2} = -\dot{N}_{\text{H}_2\text{O}} = \frac{iA}{2F}$, so $\sum_j \dot{N}_j = 0$. Integration along the total anode GDL length yields:

$$X_{\text{H}_2}^* = X_{\text{H}_2}^0 - \frac{IR_g T t_a}{2F PD_{\text{H}_2}^{\text{eff}}} \quad \text{Eq. (18)}$$

The water mole fraction can be found using the same procedure taken for hydrogen.

$$X_{\text{H}_2\text{O}}^* = X_{\text{H}_2\text{O}}^0 + \frac{IR_g T t_a}{2F PD_{\text{H}_2\text{O}}^{\text{eff}}} \quad \text{Eq. (19)}$$

For the oxygen, the general form of the equation would be different as $\sum_j \dot{N}_j = \dot{N}_{\text{O}_2} = \frac{iA}{4F}$.

$$\dot{N}_{\text{O}_2} = -\frac{PD_{\text{O}_2}^{\text{eff}}}{R_g T} \frac{d(X_{\text{O}_2})}{dy} + X_{\text{O}_2} \dot{N}_{\text{O}_2} \quad \text{Eq. (20)}$$

Integration along the total cathode GDL length yields:

$$X_{O_2}^* = 1 + (X_{O_2}^0 - 1) \exp\left(\frac{IR_g T t_c}{4FPD_{O_2}^{eff}}\right) \quad \text{Eq. (21)}$$

The effective diffusion coefficient in the porous media, neglecting the Knudsen diffusion, is found using the following formula proposed by Hirschfelder, Bird, and Spotz [219], [220]:

$$D_{ij}^{eff} = \frac{10^{-7} T^{1.75} \left(\frac{1}{M_i} + \frac{1}{M_j} \right)^{0.5}}{P \left[(\Sigma v_i)^{\frac{1}{3}} + (\Sigma v_j)^{\frac{1}{3}} \right]^2} \frac{\phi}{\tau} \quad \text{Eq. (22)}$$

Where, M_i and M_j are the molecular weight of each species, P is the pressure of the mixture in [atm], ϕ and τ correspond to the electrode porosity and tortuosity, respectively, and Σv_i and Σv_j represent diffusion volume. The diffusion coefficient in Eq. (22) represents the bulk diffusion coefficient. However, if the pore size of the porous GDLs is relatively small, another mode of diffusion called Knudsen diffusion will be activated in addition to bulk diffusion. In this thesis, it is assumed that Knudsen diffusion effects are negligible because of large pore size and since the concentration of species found by the pseudo-2D model was the same as those obtained by ANSYS 3D simulations (in which Knudsen diffusion was considered), this was a reliable assumption.

Solid oxide fuel cells operate at elevated temperatures and the operating temperature highly affects the rest of the parameters within the cell. Therefore, solving the energy equation can help increase the accuracy of the method to a great extent. However, there are many studies in the literature in which the temperature is assumed to be an input parameter. In this research, the main assumption is that the operating temperature and the cell temperature are the same while being different from the inlet temperature; the validity of this assumption is further discussed in the next section. The energy equation is used for a lumped control volume (see Figure 3-2) over the entire cell:

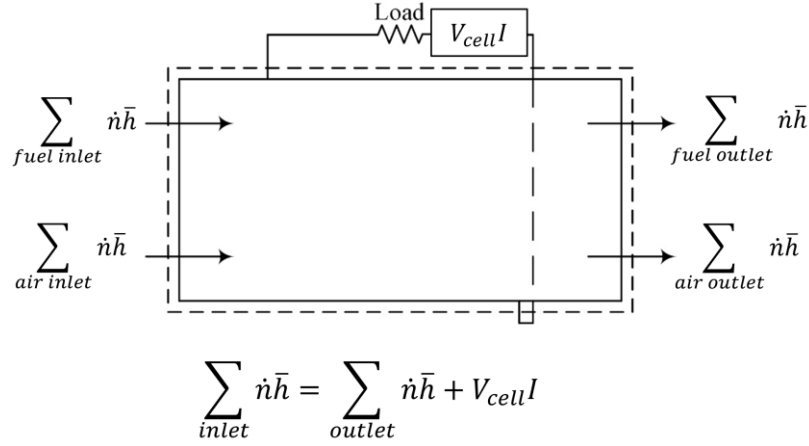


Figure 3-2. Control volume used for solving the energy equation in a single cell

$$\sum_{inlet} \dot{n} \bar{h} = \sum_{outlet} \dot{n} \bar{h} + V_{cell} I \quad \text{Eq. (23)}$$

Where, \dot{n} is the molar flow rate and \bar{h} represents the enthalpy of the species. Summations presented in Eq. (23) are calculated as follows:

$$\begin{aligned} \sum_{inlet} \dot{n} \bar{h} = & \dot{n}_{in,a} (X_{H_2,in} \bar{h}(T_{in})_{H_2,in} + X_{H_2O,in} \bar{h}(T_{in})_{H_2O,in}) \\ & + \dot{n}_{in,c} (X_{O_2,in} \bar{h}(T_{in})_{O_2,in} + X_{N_2,in} \bar{h}(T_{in})_{N_2,in}) \end{aligned} \quad \text{Eq. (24)}$$

$$\begin{aligned} \sum_{outlet} \dot{n} \bar{h} = & \left(\dot{n}_{in,a} X_{H_2,in} - \frac{I}{2F} \right) \bar{h}(T)_{H_2} \\ & + \left(\dot{n}_{in,a} X_{H_2O,in} + \frac{I}{2F} \right) \bar{h}(T)_{H_2O} \\ & + \left(\dot{n}_{in,c} X_{O_2,in} - \frac{I}{4F} \right) \bar{h}(T)_{O_2} \\ & + \dot{n}_{in,c} X_{N_2,in} \bar{h}(T)_{N_2} \end{aligned} \quad \text{Eq. (25)}$$

All species behave like ideal gas at the elevated operating temperatures. Therefore, the enthalpy values are calculated by linear functions with constants a_i and b_i (see Table 3-2) obtained by fitting to the experimental data [221]. The real data, as well as the linear regression, is presented in appendix A.2.

$$\bar{h}(T)_i = a_i T + b_i \quad \text{Eq. (26)}$$

Table 3-2. The enthalpy constants (valid for $700^\circ \text{ K} \leq T \leq 2000^\circ \text{ K}$)

species	a_i (J/mol. K)	b_i (J/mol)
H ₂	31.683	-10953
H ₂ O	45.202	-260759
O ₂	35.984	-13175
N ₂	34.104	-12514

Finally, the relation between temperature, voltage, and current, is found by simplifying the Eq. (26) and solving for T (see appendix A.2 for the proof):

$$T = f(\text{inlet conditions}, a_i's, b_i's, I, V_{\text{cell}}) \quad \text{Eq. (27)}$$

The coupled governing equations mentioned in this section are highly non-linear and an iterative algorithm is required to find the solution to the proposed simplified mathematical model. The algorithm provided in Figure 3-3 is used in the current study in order to find the species mole fraction, the current density distribution, and the temperature at different values of the operating voltage.

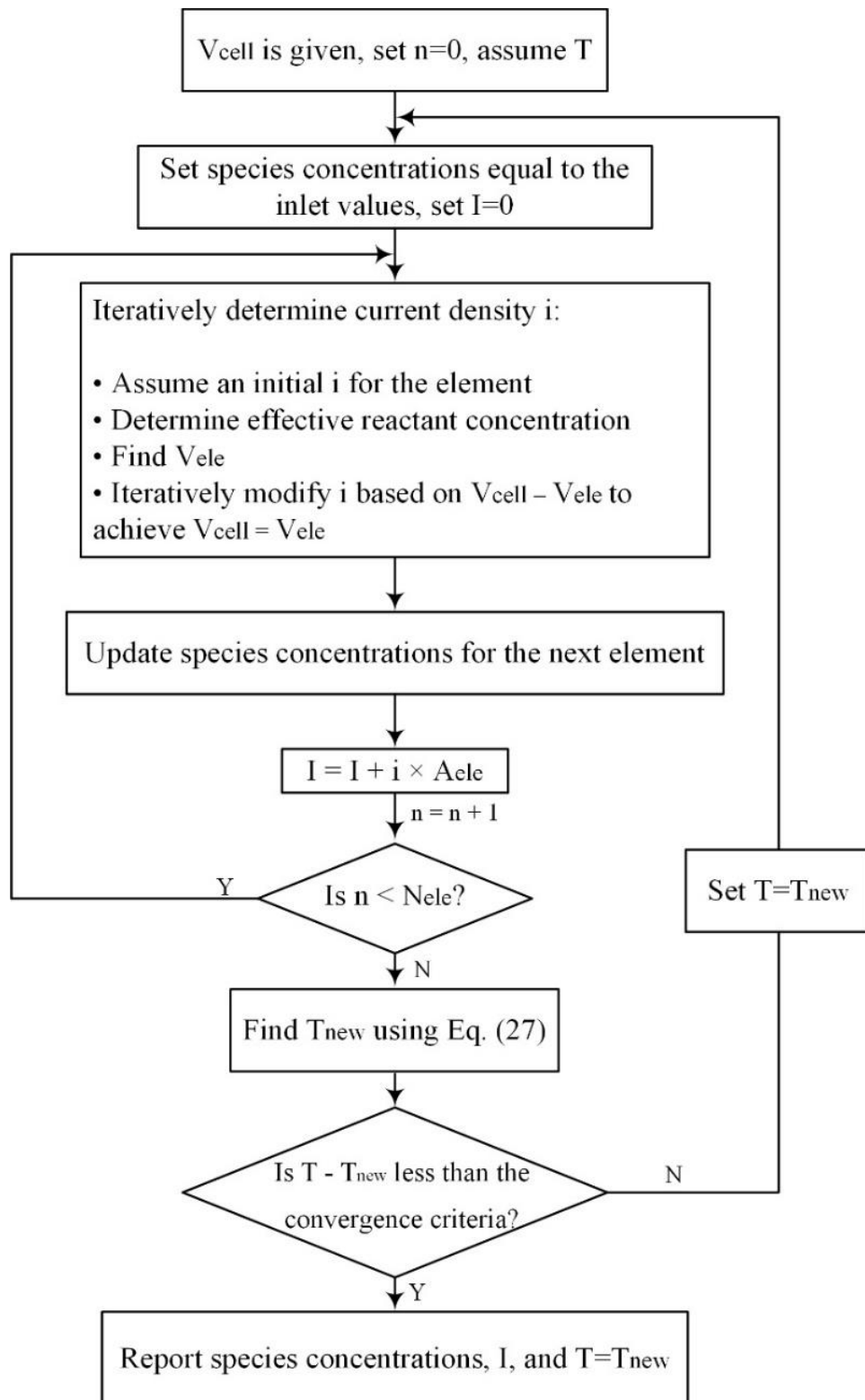


Figure 3-3. The algorithm employed by the pseudo-2D approach for finding the cell temperature, the cell's current, and the reactants' concentrations as a function of cell voltage

3.2. 3D Model

A three-dimensional full-physics model is also developed in this research to evaluate the performance of the pseudo-2D approach. The 3D model is built in ANSYS Fluent and the simulations are done by the “SOFC With Unresolved Electrolyte” add-on module of the ANSYS Fluent. The module is only available in 3D and an extra license is required for utilization of the module. There are user-defined functions inside the libraries of the module for taking into account the electrochemical effects. The module is called SOFC with unresolved electrolyte because all of the electrochemical reactions and their effects on the domain are lumped into a voltage jump at the electrolyte surface. Also, half of the heat generated by the electrochemical reaction is dissipated into the neighbor cell on the anode side, while the other half is released into the cathode side. A generic view of the 3D model is represented in Figure 3-4.

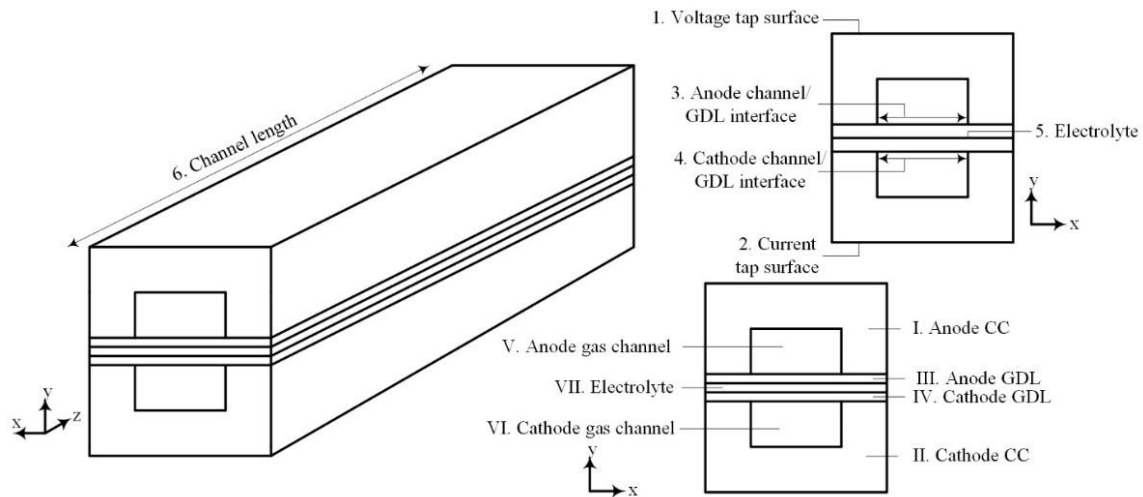


Figure 3-4. A generic view of the 3D model built in ANSYS Fluent

Appropriate boundary conditions should be set in order to solve the coupled partial differential equations through the domain. The momentum, thermal, species, and potential boundary conditions used for each surface shown in Figure 3-5 are provided in Table 3-4. Also, there are different solid, fluid, and porous zones inside the cell as shown in Figure 3-4, and each part should be clearly defined by the user according to what mentioned in Table 3-3.

Table 3-3. Different zone types corresponding to the areas shown in Figure 3-4

Zone name		Zone Type	Porous?
I.	Anode CC	Solid	-
II.	Cathode CC	Solid	-
III.	Anode GDL	Fluid	Yes
IV.	Cathode GDL	Fluid	Yes
V.	Anode gas channel	Fluid	No
VI.	Cathode gas channel	Fluid	No

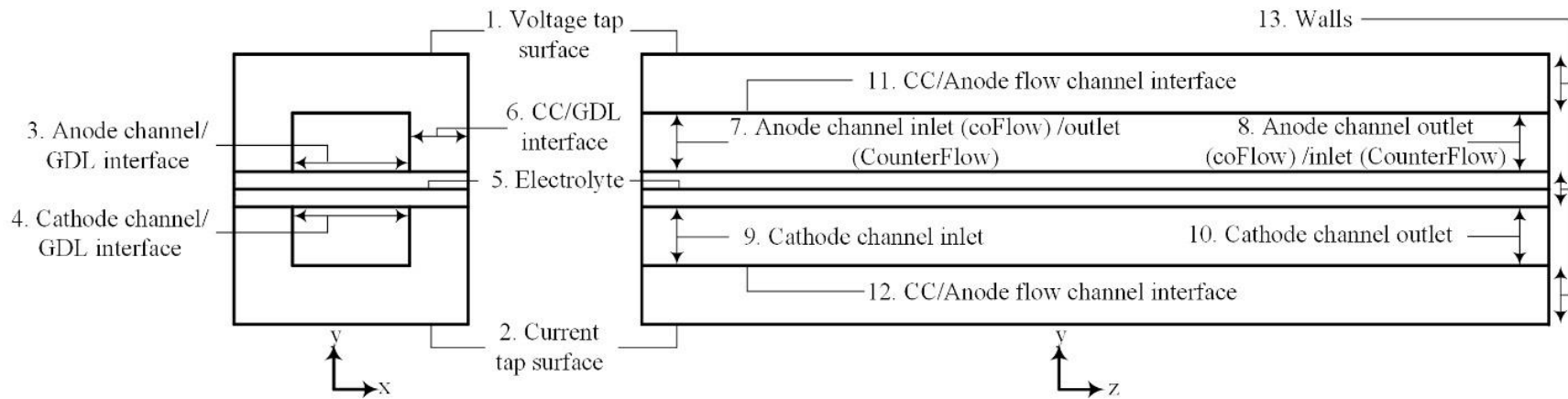


Figure 3-5. Schematic of the boundaries of the 3D cell

Table 3-4. Momentum, thermal, species, and electric potential boundary conditions for the boundaries shown in Figure 3-5

Boundary number	Surface type	Boundary conditions			
		Momentum	Thermal	Species	Electric potential
1	Wall	Stationary wall and no slip	Isolated	Zero diffusive flux	$\phi = 0$
2	Wall	Stationary wall and no slip	Isolated	Zero diffusive flux	$\phi = V_{\text{cell}}$ OR $i = I_{\text{cell}}$
3	Interface	Coupled	Coupled	Coupled	Coupled
4	Interface	Coupled	Coupled	Coupled	Coupled
5	Pair of shadow walls	Stationary wall and no slip	Coupled	Zero diffusive flux	Coupled
6	Wall	Stationary wall and no slip	Coupled	Zero diffusive flux	Coupled
7	Mass flow inlet	Mass flow rate = Fuel mass flow rate	Constant temperature	Constant mass fractions	Zero flux
8	Pressure outlet	Pressure = Operating pressure	Backflow condition	Backflow condition	Backflow condition
9	Mass flow inlet	Mass flow rate = Air mass flow rate	Constant temperature	Constant mass fractions	Zero flux
10	Pressure outlet	Pressure = Operating pressure	Backflow condition	Backflow condition	Zero flux
11	Wall	Stationary wall and no slip	Coupled	Zero diffusive flux	Coupled
12	Wall	Stationary wall and no slip	Coupled	Zero diffusive flux	Coupled
13	Wall	Stationary wall and no slip	Isolated	Zero diffusive flux	Zero flux

Solution control parameters can greatly affect the performance of the solver and unfortunately, the software default settings are not sufficient for the solution to converge, because the solver shows an extremely sensitive behavior with the changes in the species concentration. Appropriate under-relaxation factors should be used along with the adjustment of the multi-grid settings. The “BCGSTAB” can be used to stabilize the solution in case of fluctuating residuals. The solution control settings are not provided by the software user guide and the values used in this study (see Table 3-5) had to be found using trial and error.

The governing equations that are used by the software for finding the solution are all mentioned through the software user manual in detail [218]. In addition to software user manual, useful explanations on each governing equation is provided by Stam [222]. It is worth mentioning that going over the information presented in the user manual is not enough for finding the solution because of the complexity of the physics of the problem. Therefore, an interactive procedure was found by trial and error after many failures in the convergence of the solution. The sequential procedure taken for using the module is mentioned in Figure 3-6.

Table 3-5. Under-relaxation factors and solver settings for the ANSYS Fluent

Under-relaxation factors		Cycle types	
Pressure	0.30	Pressure	V-cycle
Density	0.40	X- Momentum	Flexible
Body forces	0.40	Y- Momentum	Flexible
Momentum	0.60	Z- Momentum	Flexible
h_2O	0.99	h_2O	V-cycle
O_2	0.99	O_2	V-cycle
h_2	0.99	h_2	V-cycle
Energy	1.00	Energy	F-cycle
Electric potential	1.00	Electric potential	F-cycle
		Maximum number of cycles	50

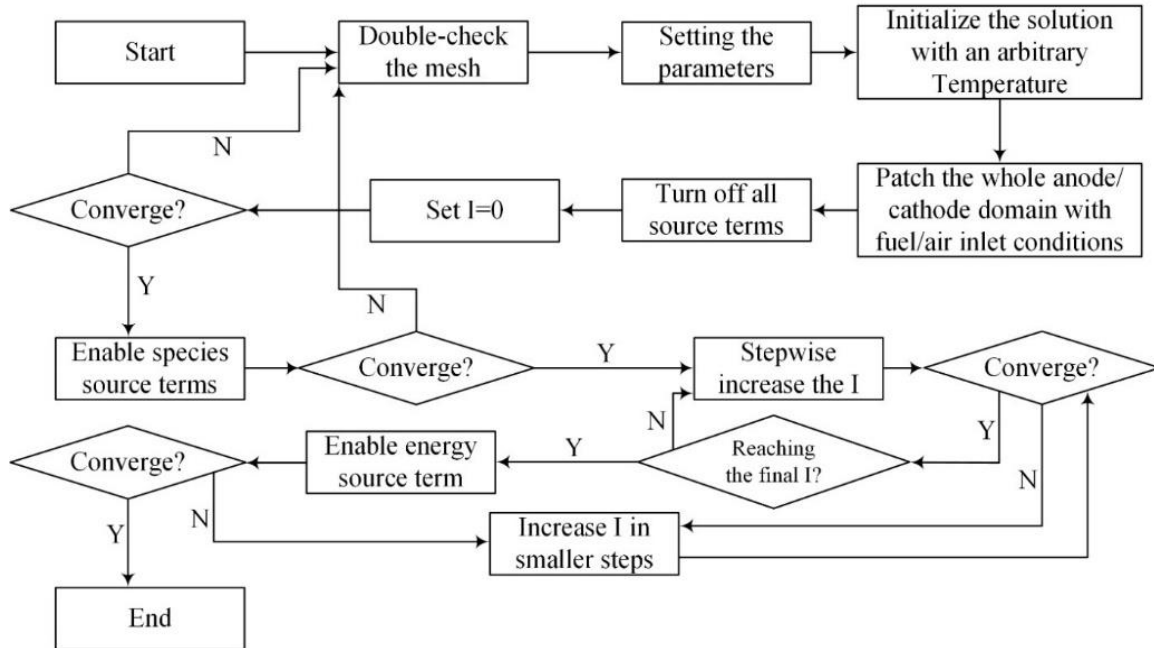


Figure 3-6. The step by step procedure required for finding the solution with the 3D model

3.3. Material Selection

The next step is selecting the appropriate materials for the electrodes and the electrolyte. The electrochemical reactions occur at the anode side where the oxygen ions coming from the cathode side react with the hydrogen molecules at the vicinity of the electrolyte. Therefore, the anode material should possess high electrical and ionic conductivity, high catalytic activity for fuel oxidation, mechanical stability to overcome the thermal stress, acceptable porosity to allow for the transport of hydrogen and water through the gas diffusion layer, and corrosion resistance to fuel impurities. Zirconia has a monoclinic structure at room temperature which morphs into tetragonal and cubic structures at high temperatures where it shows the highest conductivity. However, zirconia cannot tolerate the transition between the different crystal structures during the start-up and cool down phases. Stabilizing the structure of the zirconia with appropriate amounts of yttria results in oxygen ions vacancies that help migration of the ions from one site to another site with diffusion and random thermal motion at high temperatures. Finally, Ni should be added to the yttria-stabilized zirconia (YSZ) as a catalyst to increase the electrochemical activity of the electrode. Therefore, a cermet of Ni supported on YSZ is used for the anode material [223]. The main challenge in using such material on the anode side is oxidation of the Ni particles that occur when there is not enough fuel present at the

reaction sites. Also, thermal expansion of Ni is greater than YSZ which might result in developing cracks inside the material in case of high-temperature gradients. Poisoning of the cell with fuel impurities such as sulfur, silica, phosphorus, and carbon (in case of hydrocarbon fuels) is also another problem that should be solved by processing the fuel. YSZ is used as the electrolyte material because of the ability to conduct oxygen ions at high temperatures, impermeability to reactants cross-over, and chemical stability. YSZ shows a mixed conductivity of the electrons and ions measured by the transference number. However, the transference number is mostly close to unity which is an indicator of ionic conductivity rather than the electronic conductivity [224]–[227]. Finally, Strontium-doped Lanthanum Manganite (LSM) is used on the cathode side for promoting the oxygen ions formation while maintaining high mechanical and chemical stability at the elevated temperatures [228], [229].

3.4. Validation of the Mathematical Model

For examining the validity of the study, the 3D model is built in ANSYS Fluent to compare the polarization curve for the same cell studied by Sembler and Kumar [56], [67] and Wei et al. [230] operating with the identical inlet conditions and electrochemical parameters. The geometrical dimensions of the cell are presented in Table 3-6 while the inlet conditions are mentioned in Table 3-7.

Table 3-6. Geometry of the cell

Parameter	Value	Units
Channel height	1	mm
Channel width	1.5	mm
Channel length	50	mm
CC height above the channels	1	mm
Ribs thickness on each side	0.25	mm
Anode thickness	1.8	mm
Cathode thickness	30	μm
Electrolyte thickness (virtual)	20	μm

Table 3-7. The inlet boundary conditions used for the validation of the study [56], [67], [230]

Anode mass flow rate	4.48 e-07	kg/s
Cathode mass flow rate	2.17 e-05	kg/s
Anode inlet temperature	1123	K
Cathode inlet temperature	1123	K
Anode flow composition	97% H_2 , 3% O_2	%mole
Cathode flow composition	Dry Air	—
Cell pressure	1	Atm

Thermophysical and electrochemical properties used by [56], [67], [230] are presented in Table 3-8. The same values for the electrochemical properties were used for the purpose of validation.

The 3D CFD simulation done in the ANSYS Fluent is based on the finite volume method. Therefore, the utilization of the proper mesh is of great importance. Although using a denser mesh would typically lead to more accurate results, especially for the steady-state cases, it can lead to very long computation times even using multiple computer processors. The same mesh density proposed by Sembler and Kumar [67], i.e. $dz = 0.5\text{ mm}$, $dy = 0.1\text{ mm}$, $dx = 0.1\text{ mm}$, is used in this section to run the 3D simulations except for dy . It should be noted that a very smaller value for dy is used for the GDL section as the GDL is very thin itself and a finer mesh is required to capture the changes through the gas diffusion layer. After building the geometry, applying the mesh, defining the proper materials, and setting up the boundary conditions and solver settings, the simulations were run according to the algorithm provided in Figure 3-6 for the different values of total current. The polarization curved obtained by the 3D model and the models by [56], [67], [230] are illustrated in Figure 3-7. The results show good agreement between the models. The largest error was found to be six percent (0.47 V against 0.44 V) for the case with 1 amp/cm^2 current density. It is worth mentioning that using more polarization curves from different studies for validating the results would be a more solid approach. However, we only included two works in this thesis since details regarding all morphological and electrochemical properties were not included for a single planar cell in the literature. It is recommended that electrodes GDL properties, the activation energy of the electrochemical reactions, pre-exponential factors in evaluating the exchange current density, charge transfer coefficients in the Butler-Volmer equation, and cell geometrical dimensions are described when reporting results for SOFC simulations. The average

temperature distribution along the cell for the 3D case is shown in Figure 3-8. According to Figure 3-8, the temperature distribution is almost uniform through the cell and the outlet temperature will be assumed the same as the average cell temperature for the simplified model. It should be noted that these high operating temperatures (in comparison with the inlet temperature) are not suitable from the standpoint of thermomechanical stability. The reason behind this temperature rise is the low air flow rate on the cathode side. In future chapters, a higher cathode flow rate is set so that the results are more realistic. However, the low air flow rate reported in Table 3-7 is used in this chapter to stay consistent with the literature data that this work is going to be validated against.

Table 3-8. Thermophysical and electrochemical properties used for running the validation simulations [56], [67], [230]

Cathode GDL (LSM)	Porosity	0.375	
	Tortuosity	3	
	Exchange current density	800	Amp/m ²
	Specific heat	450	J/kgK
	Thermal conductivity	11	W/mK
	Electron conductivity	7937	1/Ωm
	Density	5620	kg/m ³
	Cathodic transfer coefficient	0.7	
	Anodic transfer coefficient	0.7	
Anode GDL (NiO+YSZ)	Porosity	0.24	
	Tortuosity	3	
	Exchange current density	200000	Amp/m ²
	Specific heat	450	J/kgK
	Thermal conductivity	10	W/mK
	Electron conductivity	333330	1/Ωm
	Density	6500	kg/m ³
	Cathodic transfer coefficient	0.7	
	Anodic transfer coefficient	0.7	
Electrolyte (YSZ)	Specific heat	450	J/kgK
	Thermal conductivity	2	W/mK
	Density	5480	kg/m ³
	Resistivity	0.1	

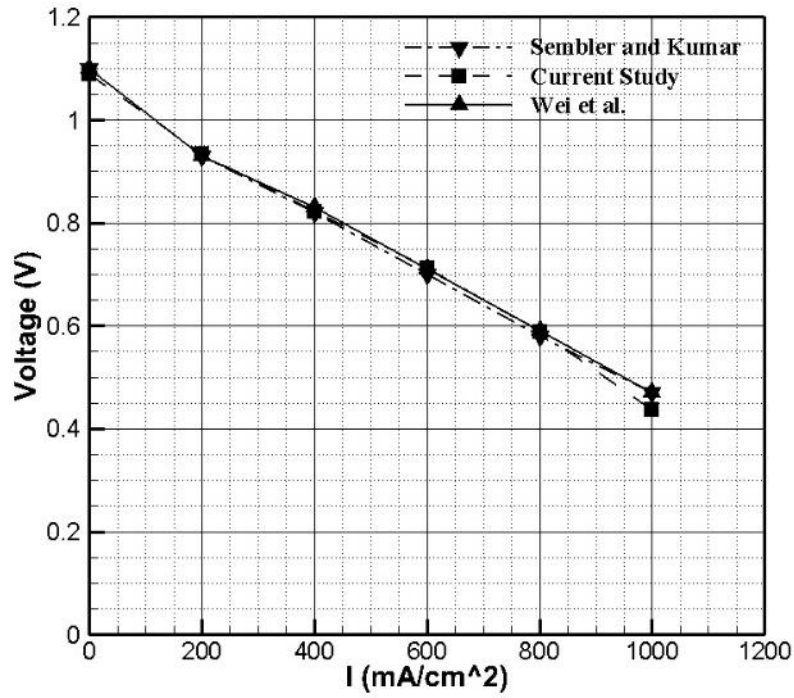


Figure 3-7. Comparing the polarization curve of the 3D model with those obtained by [56], [67], [230]

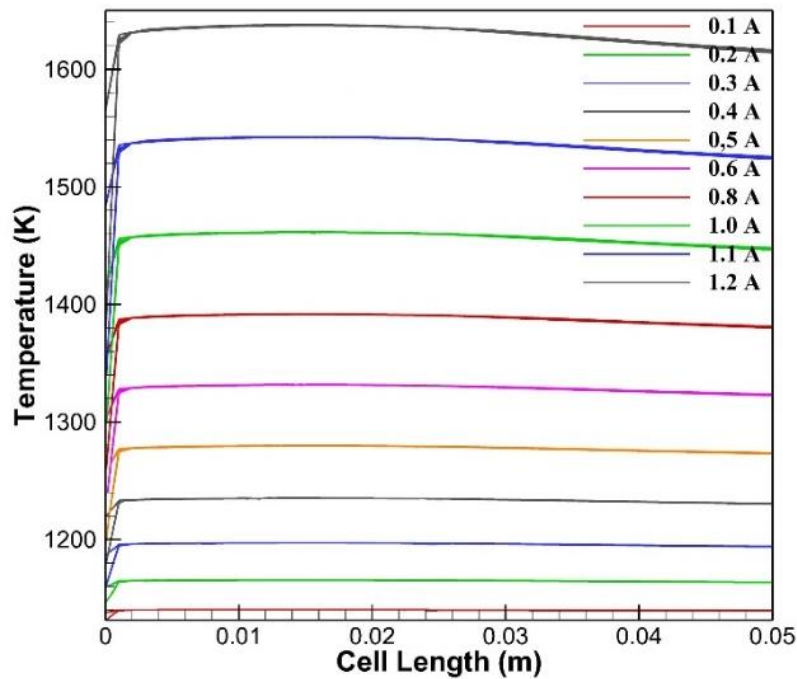


Figure 3-8. The average temperature distribution along the cell found by the 3D simulation in ANSYS Fluent

After conducting the simulations for the 3D model and comparing the results with the available data in the literature, the pseudo-2D model was used according to the same parameters and assumptions made by the 3D studies. A constant set of exchange current density on the anode and cathode sides, as well as the same electrochemical parameters used by the 3D models, were employed for comparing the results. The polarization curves obtained by both full-physics and simplified models are depicted in Figure 3-9. Furthermore, the hydrogen and oxygen mole fractions for the counter-flow case obtained by both 3D and pseudo-2D cases are shown in Figure 3-10, and the results are in good agreement. In our limited testing, the simulations for the pseudo-2D case were found to be 10^5 times faster than 3D simulations for co-flow condition and 10^3 times faster than 3D simulations for the counter-flow case (using 4 cores of “Intel(R) Xeon(R) CPU E5-2630 v3 @ 2.40 GHz”). The pseudo-2D simulation is also expected to be significantly faster to execute on other systems.

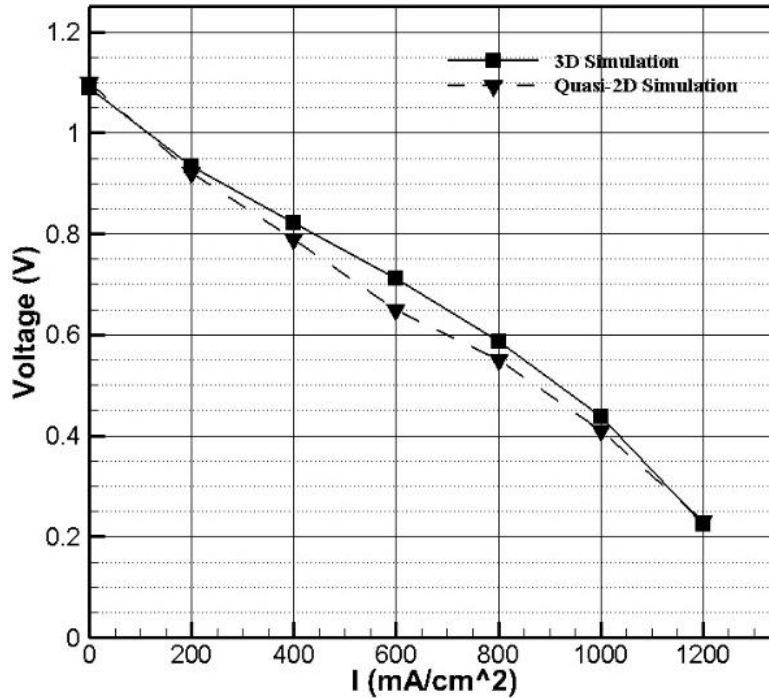
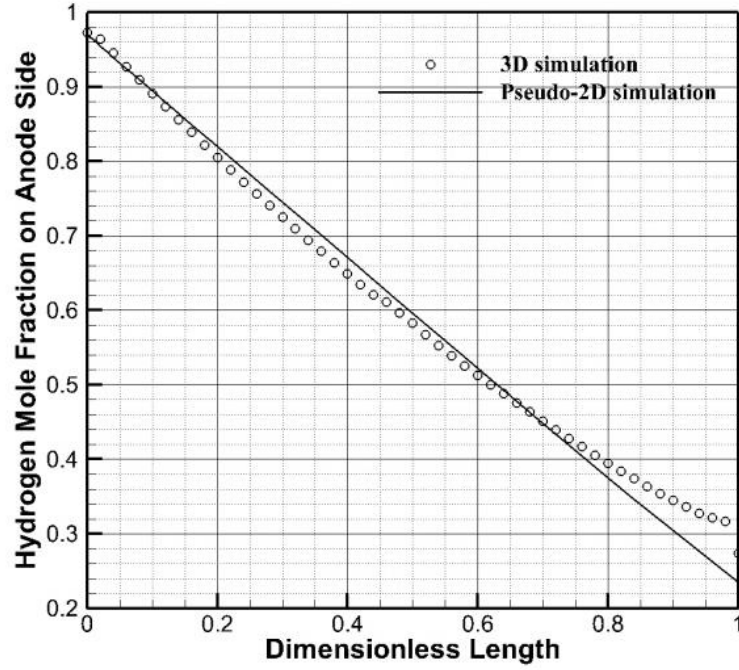


Figure 3-9. The polarization curve for both 3D and pseudo-2D simulations

(a)



(b)

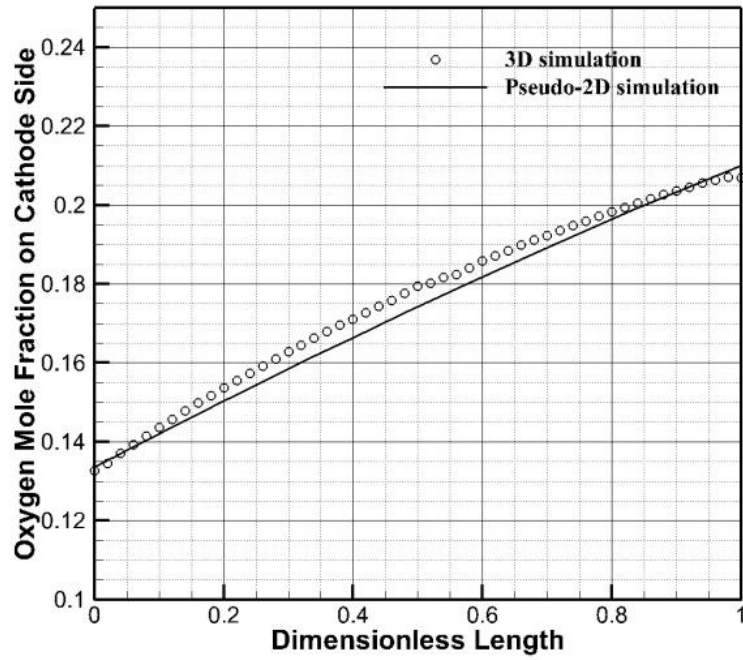


Figure 3-10. (a) Hydrogen, and (b) Oxygen concentration for the counter-flow configuration along the cell obtained by both pseudo-2D and 3D simulations for $I=1.0$ A

Chapter 4.

Parameter Estimation Using Inverse analysis

The materials properties for the anode and cathode are presented in Table 4-1. This study can be extended to SOFCs using other electrodes. A full discussion on SOFC material is beyond the scope of this section and the readers are referred to other studies in the literature [223]–[228], [231]. The cell inlet boundary conditions are provided in Table 3-7. It should be noted that porosity, tortuosity, and exchange current densities are uncertain for the inverse problem. The “true” properties of the GDL used for forward simulations and the realistic range of the unknown parameters determined from the literature [13], [232]–[242] are summarized in Table 4-1. This chapter includes the inverse problem formulation followed by the sensitivity analysis of the polarization curve to the unknown parameters and the optimum estimation results.

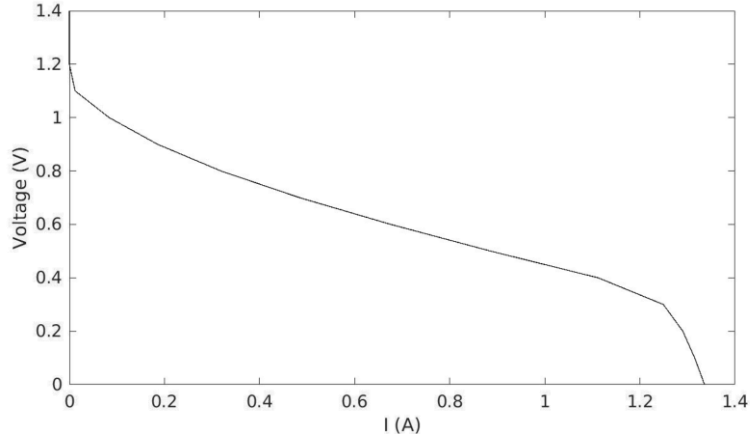
Table 4-1. Electrodes materials and properties for the base case

a. Cathode GDL (LSM) [228], [231]–[243]		
Properties	Base-case (“true”) values	Expected range
Porosity	0.375	[0.15-0.5]
Tortuosity	3	[2-6]
Exchange current density	1000 Amp/m ²	[600-5000] Amp/m ²
Cathodic transfer coefficient	0.5	(no variation assumed)
b. Anode GDL (NiO+YSZ) [223], [232]–[243]		
Properties	Base-case (“true”) values	Expected range
Porosity	0.24	[0.15-0.5]
Tortuosity	3	[2-6]
Exchange current density	7460 Amp/m ²	[600-14000] Amp/m ²
Anodic transfer coefficient	0.5	(no variation assumed)

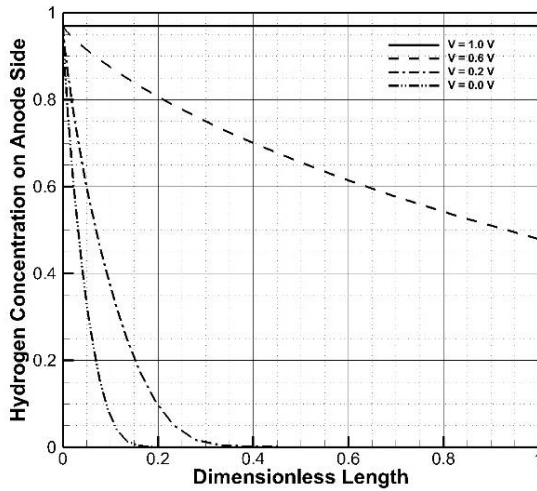
4.1. Inverse Problem Formulation

The SOFC is simulated using the pseudo-2D model for the co-flow condition with the fuel and oxidant flowing in the same direction. Figure 4-1a shows the polarization curve for the co-flow case, while Figure 4-1b and c show the reactant concentration along the dimensionless channel length (with fuel inlet plane corresponding to ‘0’). Figure 4-1 shows that hydrogen and oxygen concentration decrease along the channel as the result of

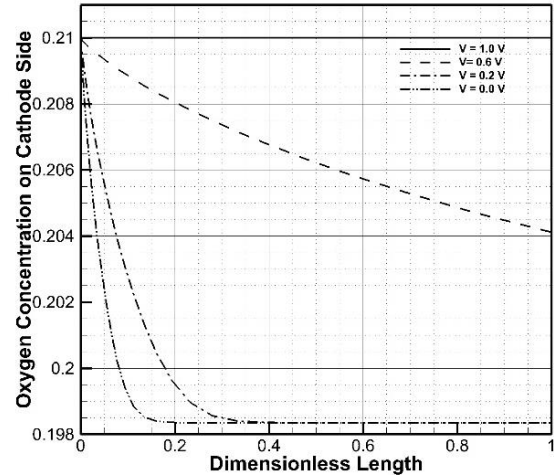
electrochemical reactions. As expected, the amount of hydrogen at the anode outlet decreases by increasing the current density (decreasing the voltage). Since the cell is supplied with excess oxygen, the drop in oxygen concentration is very small.



a. Polarization curve



b. Hydrogen concentration



c. Oxygen concentration

Figure 4-1. Base case simulation using the pseudo-2D code [65].

The primary objective of this work is to develop a systematic tool for parameter estimation using an appropriate optimization technique, through an inverse approach. It would be difficult to accurately evaluate the performance of the inverse methodology by applying the inverse method to a polarization curve given by experiments, since the exact value of the unknown parameters (effective porosity and exchange current density) may

not be known. Hence, a theoretical polarization curve is generated for the parameter set given in Table 4-1. This theoretical polarization curve is presented in Figure 4-1a. For the inverse problem, the anode and cathode exchange current densities ($J_{0,a}$, and $J_{0,c}$) appearing in the Butler-Volmer equation for evaluating the activation overpotential, and the effective porosities (i.e porosity divided by tortuosity) at the anode and cathode (ϕ_a , ϕ_c) are assumed to be the uncertain parameters. For each iteration using the unknown parameter set, we then define the following fitness function.

$$\text{fitness} = \sqrt{\frac{1}{N} \sum_{j=1}^N \left(\frac{I_{\text{iter},j} - I_{\text{target},j}}{I_{\text{target},j}} \times 100 \right)^2} \quad \text{Eq. (28)}$$

Where

$I_{\text{target},j}$, $j = 1$ to N are the target “actual” currents at N predetermined voltages (Figure 4-1a).

$I_{\text{iter},j}$, $j = 1$ to N are load currents for a given parameter set at “ N ” different voltages.

The fitness function defined in the current study considers all points on the polarization curve except the point corresponding to the open circuit voltage (where one cannot divide by zero). The exchange current densities (and subsequently activation overpotentials) are easier to discern at lower current densities. Table 4-2 summarizes the other fitness functions used in the literature for SOFCs. Sarmah et al. [244] estimated the operating parameters of a hybrid SOFC/GT/ST power plant corresponding to the total energy and exergy efficiencies (second law efficiency). In their algorithm, energy and exergy efficiencies of the power plant are first found using random initial values of unknown parameters, followed by evaluation of the fitness function and finally finding values for the unknown parameters for the next iteration. So, one can interpret the work done by Sarmah et al. [244] as a problem of finding the operating parameters of the power plant according to the target efficiencies. In another work, Gogoi and Das [154] used power output as the only target value for the fitness function they defined to evaluate current density, pressure, and fuel flow rate of an internal reforming SOFC. On the other hand, Shi and Xue [153] calculated the sum of the differences between the calculated power and the desired power for all of the points on the polarization curve to evaluate the electrochemical properties of

a button-cell SOFC. Utilizing the whole polarization curve for evaluating parameters is a more concrete way of tackling the estimation problem because it provides information about different data points. However, using just one operating point might yield counterintuitive results as the behavior of the cell changes at different values of current.

Table 4-2. Fitness functions previously used for the inverse analysis of SOFCs in the literature

Study	Fitness function used
Sarmah et al. [244]	$f = \left[\left(\frac{\dot{W}_{net,num} - \dot{W}_{net,exp}}{\dot{W}_{net,num}} \right)^2 + \left(\frac{\eta_{I,num} - \eta_{I,exp}}{\eta_{I,num}} \right)^2 + \left(\frac{\eta_{II,num} - \eta_{II,exp}}{\eta_{II,exp}} \right)^2 + \left(\frac{I_{num} - I_{exp}}{I_{num}} \right)^2 \right]$ <p>Where, \dot{W}_{net} represents the power plant net power output η_I corresponds to the power plant net energy efficiency η_{II} is the power plant net exergy efficiency I refers to the power plant irreversibility</p>
Gogoi and Das [154]	$f = (P_{out} - P)^2$ <p>Where, P is the power output at a given operating point on the polarization curve</p>
Shi and Xue [153]	$f = M_1 - M_2 \times \sum (iV_{cell,num} - iV_{cell,exp})^2$ <p>Where, M_1 and M_2 are random positive numbers</p>

The algorithm used for finding the unknown parameters using the inverse approach is presented in Figure 4-2, where \mathbb{P} is the set of unknown parameters (design variables) of the inverse problem. There exist four loops distinguished by the dashed lines. The most inner loop is only utilized for the counter-flow configuration. The total value of current for each cell voltage is found through the second loop. SOFC polarization curve is obtained by the third loop, and the outermost loop is designed to estimate the unknown parameters using the inverse approach. A brief summary of the methodology presented is presented below:

1. An arbitrary value is assumed for the initial state of design variables presented by the vector 'X'.
2. The forward solver is called to find current density corresponding to each value of cell voltage.

3. The value of the fitness function is found.
4. The next state ' X_{new} ' must be determined by an optimization technique. In this thesis, the pattern search optimization method was used because there were several local minima.
5. Steps 2 to 4 should be taken again and again until the convergence criterion is satisfied.

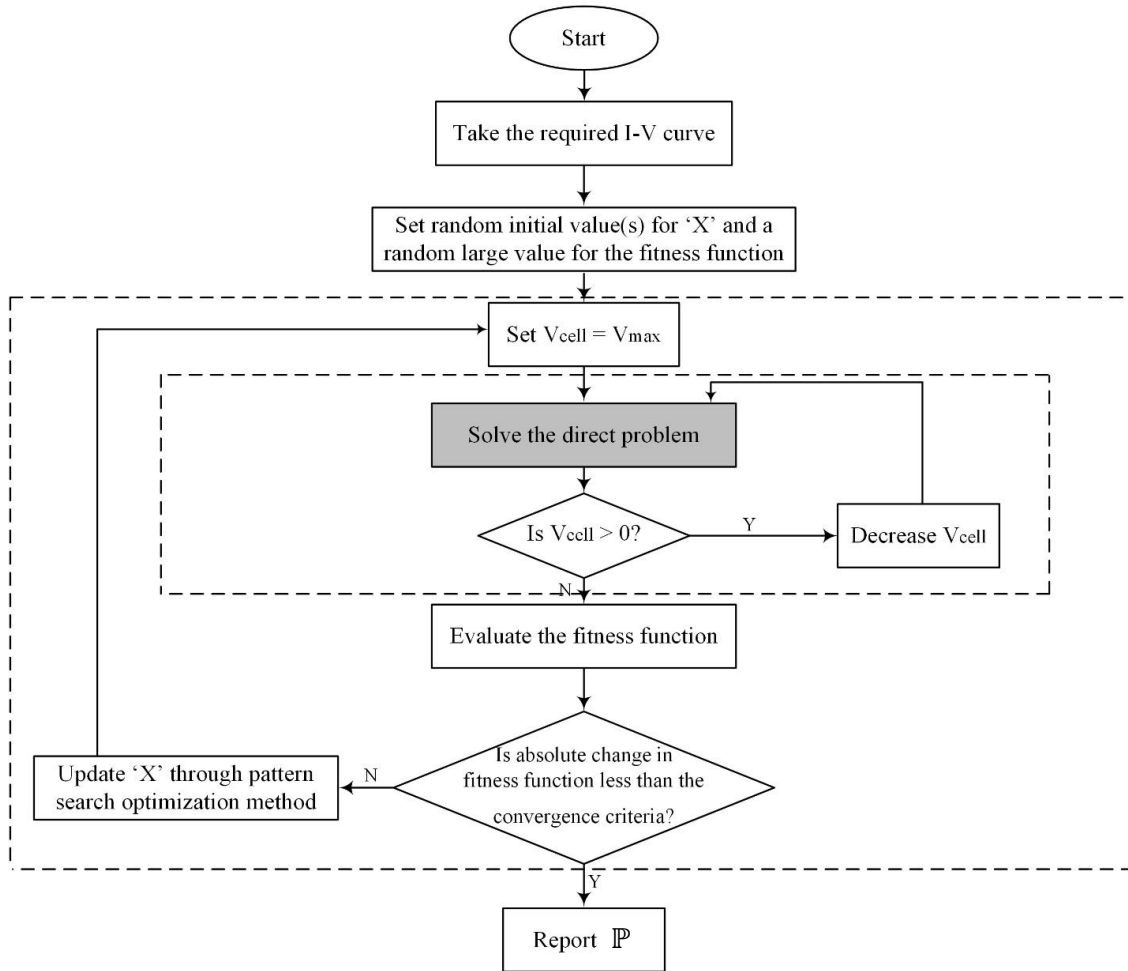


Figure 4-2. The algorithm used for finding the unknown parameters using the inverse approach

4.2. The Sensitivity of the Polarization Curve with Respect to Individual Unknown Parameters

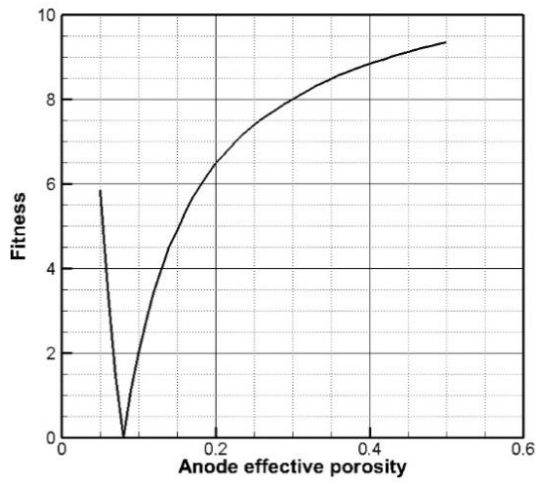
It may be noted that the unknown parameters also indirectly affect the cell temperature and therefore all the losses within the cell because of the coupling of energy equation with electrochemistry. Further details regarding both voltage-current relations and energy

equation are provided in section 3.1. In order to determine the sensitivity, we plot both the fitness function (defined in Equation 28) and the total error in evaluating the polarization curve defined as $\varepsilon = \sum_{j=1}^N (I_{iter,j} - I_{target,j})$, for each parameter. Figure 4-3 shows the sensitivity of the cell response with respect to the anode effective porosity ϕ_a and the cathode effective porosity ϕ_c . It may be noted that we use the effective porosity rather than finding the porosity and tortuosity separately. Effects of the anodic and cathodic exchange current densities on the polarization curve are presented in Figure 4-4. By examining the results, the following conclusions are drawn:

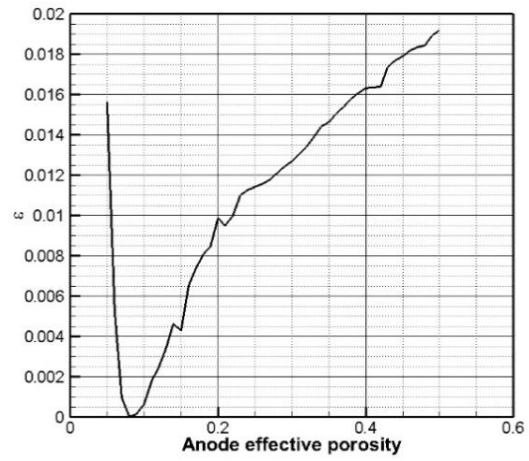
- Although some of the graphs illustrated in Figure 4-3 and Figure 4-4 showed minor oscillatory behavior in some cases, there is one and only one local and absolute minimum for the fitness function defined in Equation 28. The minimum, therefore, can be captured if an appropriate optimization algorithm is utilized.
- Comparing the fitness function values and total errors, different representation of the error in calculating the difference between the obtained polarization curve and the required one would result in different behavior.
- Oscillations are either smoothed or completely removed when using the defined fitness function.
- Looking at the vertical axis of the diagrams, the defined fitness function is easier to describe quantitatively as it comes in terms of percentage deviation from the base case.
- Although concentration losses are more severe on the cathode side, as the hydrogen diffusion coefficient on the anode side is noticeably larger than the cathodic oxygen diffusion coefficient, changing the anode effective porosity affects the polarization curve more than the amount that changing the cathode effective porosity does. Generally, cathode effective porosity did not show significant effects on system performance. This might be a result of using a very thick anode in comparison with the thin cathode GDL.
- Comparing the error resulted from changing the anodic and cathodic exchange current density values, the polarization curve showed a very sensitive behavior with respect to the exchange current density at the cathode. Also, activation losses are more significant on the cathode side. This trend is opposite to what observed for the effects of electrodes porosities. In reality, the exchange current density is considerably larger on the anode side [245]. The higher the exchange current

density is, the lower the activation overpotential will be. Therefore, the activation overpotential on the cathode side is greater than the anode side which results in cathodic exchange current density affecting the V-I curve more severely than the anodic exchange current density does.

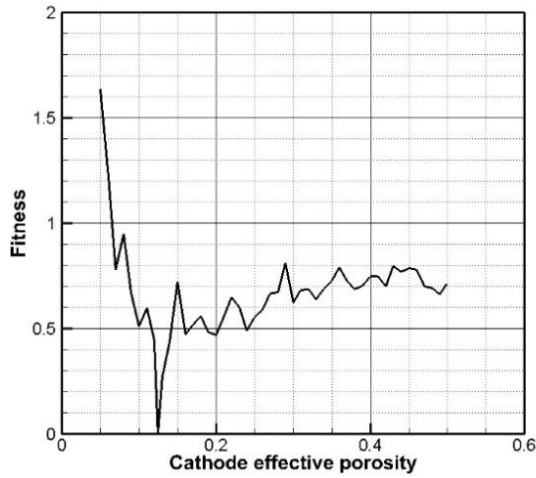
- The fitness value is less than 10 for all cases except when cathodic exchange current density deviates from its base case value.
- According to Figure 4-4, further increasing anodic and cathodic exchange current density values does not have considerable effects on the polarization curve. This indicates that the optimization problem would not be sensitive to the upper limit of the design variables, especially for the cathode and anode exchange current densities. The phenomenon is a result of high operating temperatures, and the dependence would be stronger at lower operating temperatures of intermediate-temperature SOFCs.



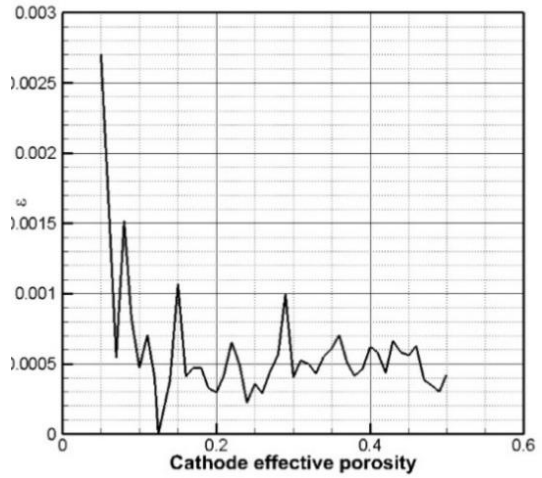
(a) The sensitivity of fitness function to ϕ_a



(b) The sensitivity of total error values

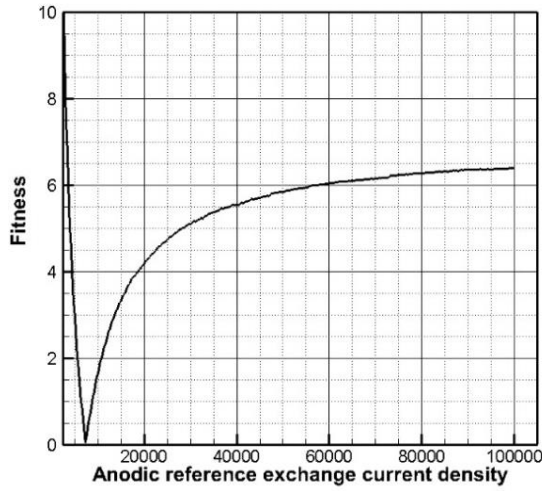


(c) The sensitivity of fitness function

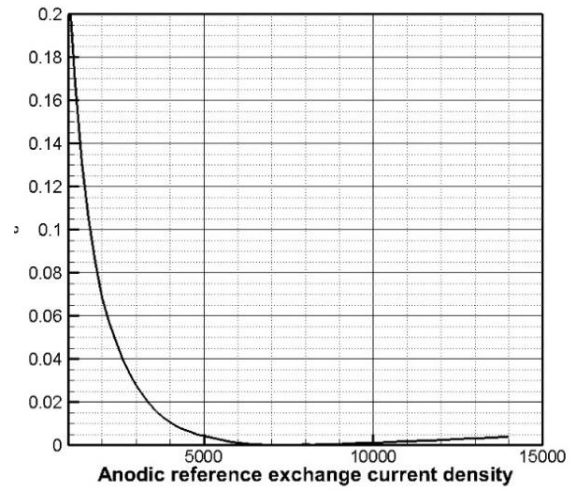


(d) The sensitivity of total error values

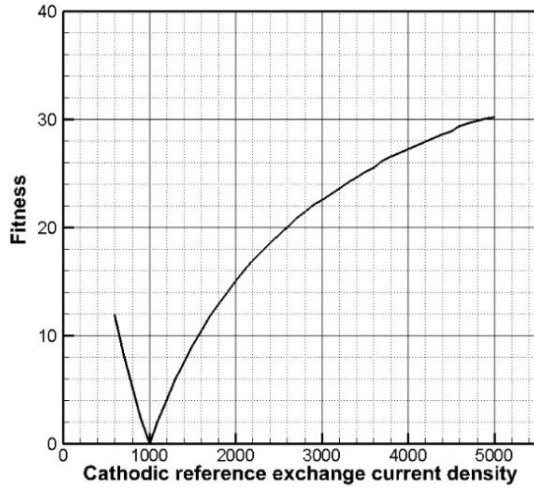
Figure 4-3. Sensitivity of system response to anode and cathode effective porosity ϕ_a, ϕ_c ($\phi_a^{true} = 0.08$, $\phi_c^{true} = 0.125$)



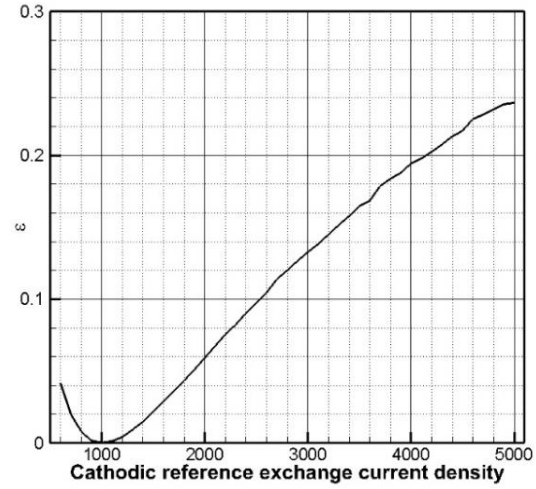
(a) The sensitivity of fitness function



(b) The sensitivity of total error values



(c) The sensitivity of fitness function



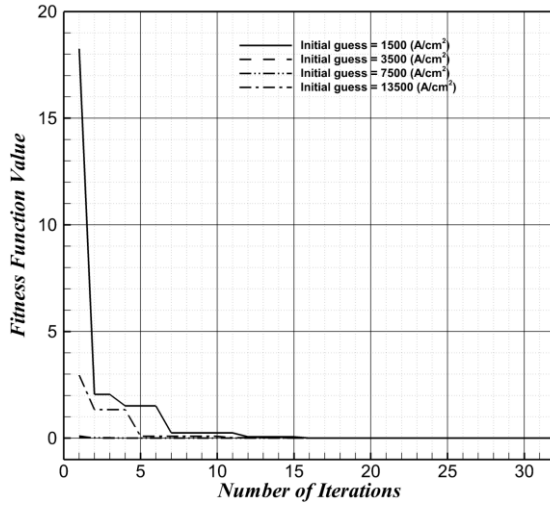
(d) The sensitivity of total error values

Figure 4-4. Sensitivity of system response to anode and cathode exchange current density, $J_{0,a}$, $J_{0,c}$ ($J_{0,a}^{true} = 7460$, $J_{0,c}^{true} = 1000$)

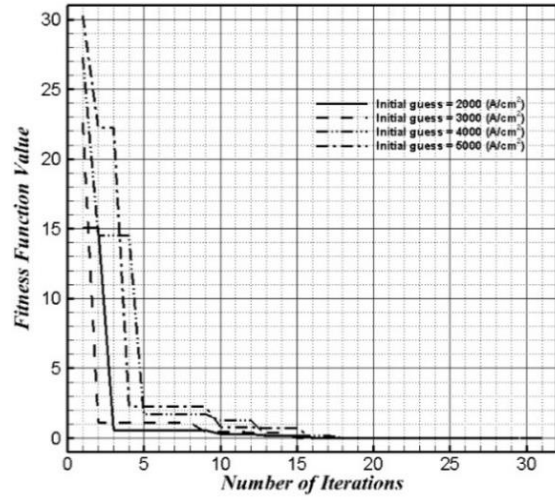
4.3. Optimal Parameter Estimation Results

This section presents the implementation of the optimization technique to the inverse problem. It may be noted that the target polarization curve can be generated by other numerical or experimental approaches. Anodic and cathodic exchange current densities and anode and cathode effective porosities were chosen as the four parameters to be estimated through the inverse analysis. The pattern search method [246] was utilized as the optimization technique for estimating the parameters in this thesis. Genetic Algorithm

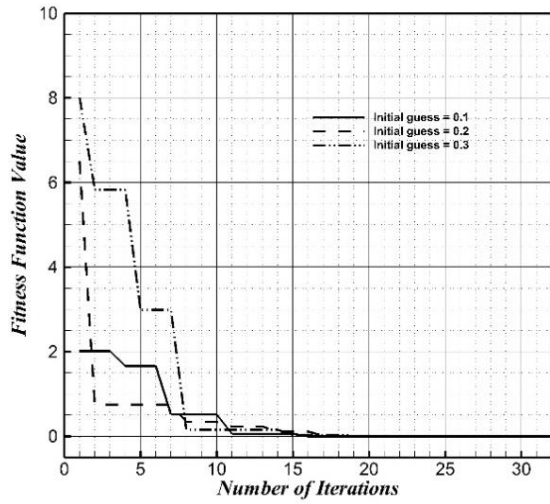
and Simulated Annealing algorithms were also utilized but they either failed to obtain the results or showed slow convergence. The effective porosities were chosen because they take into account the effects of porosity, tortuosity, and the pore diameter at the same time. Steps 1 to 5 presented in section 4.1 were utilized according to the algorithm shown in Figure 4-2 in order to find unknown parameters, both separately and simultaneously. The convergence histories, i.e. the fitness function values, are represented through Figure 4-5 and Figure 4-6 with the corresponding minimum function values and the estimated parameters reported in Table 4-3. The results in Figure 4-5 (Table 4-3a) show that the inverse approach can be successfully used to find the unknown parameters separately with no error, and in less than 20 iterations regardless of the initial guess for the design variables. In the next stage, the number of design variables was increased to two. From the sensitivity analysis, it was found that cathodic exchange current density has the largest effect on the polarization curve while the cathode effective porosity showed the smallest effect. Therefore, the inverse analysis was applied to two cases shown in the first and second sets of rows in Table 4-3b. As depicted in Figure 4-6 and Table 4-3, when $J_{0,c}$ and ϕ_a are the design variables, parameters can be estimated successfully, and the error is bounded within 7 percent. However, estimating $J_{0,a}$ instead of ϕ_a along with the $J_{0,c}$ resulted in 26 percent error in the value obtained for $J_{0,a}$. Note that cathode porosity was not added to the design variables during this stage as it did not show significant effects on the polarization curve through the sensitivity analysis. During the next stage, $J_{0,a}$, $J_{0,c}$, ϕ_a were chosen for the design variables and the solution to the inverse problem successfully yielded the real values of design variables. Finally, all the unknown variables were estimated simultaneously. In this case, the solution again converged to the values fairly close to the real ones. However, the same problem mentioned for $J_{0,a}$ when the number of design variables was equal to 2 still exists for the case of 3 design variables; the effect is more sensible for $J_{0,a}$ and ϕ_c in the case of 4 design variables if the initial guess is far away from the solution. This shows that the inverse approach can be effectively applied to the simplified pseudo-2D model to estimate the electrodes microstructural properties with either no error, in the case of single parameter estimation or within an acceptable error band, for the case of multi-parameter estimation. In conclusion, the inverse method might not provide exact values of the parameters only when design variables do not have a significant effect on the polarization curve (this case is more dominant), or when the initial guess is far away from the real values.



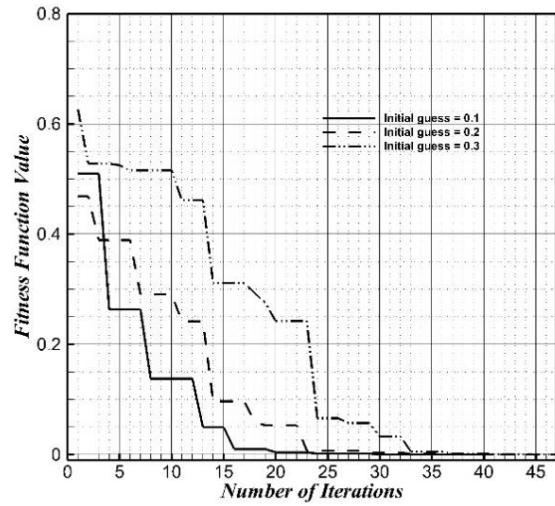
(a) Anode exchange current density, $J_{0,a}$



(b) Cathode exchange current density, $J_{0,c}$

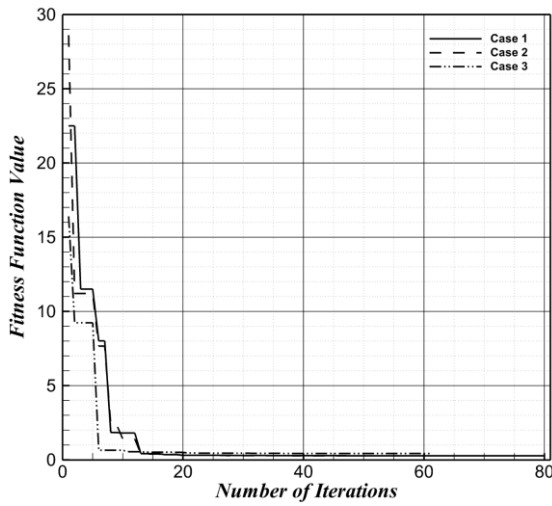


(c) Anode effective porosity ϕ_a

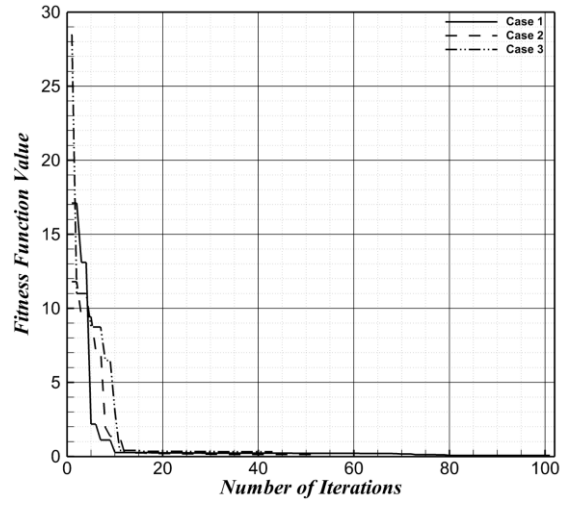


(d) cathode effective porosity ϕ_c

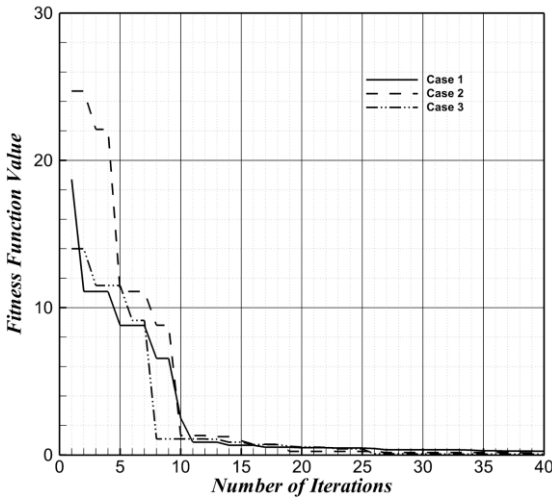
Figure 4-5. Convergence history for the inverse single parameter estimation for different initial estimates



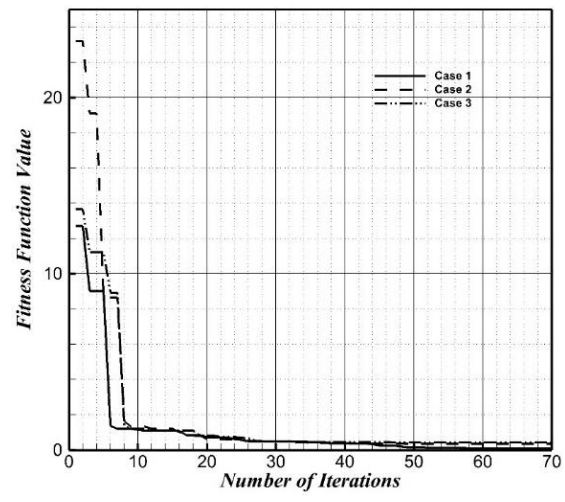
(a)



(b)



(c)



(d)

Figure 4-6. Convergence history of the inverse estimation of: (a) $J_{0,c}$ and ϕ_a ; (b) $J_{0,c}$ and $J_{0,a}$; (c) $J_{0,c}$, $J_{0,a}$, and ϕ_a ; (d) $J_{0,c}$, $J_{0,a}$, ϕ_a , and ϕ_c for three different cases with different initial conditions

Table 4-3. Summary of results obtained by the inverse analysis for single parameter and multi-parameter estimation of the design variables

a. Single parameter variation

Parameter(s) to be estimated	Initial Guess				Estimates (percentage estimation error)				Best fitness function value
	$J_{0,a}$	$J_{0,c}$	ϕ_a	ϕ_c	$J_{0,a}$ ($J_{0,a}^{\text{true}}: 7460$)	$J_{0,c}$ ($J_{0,c}^{\text{true}}: 1000$)	ϕ_a ($\phi_a^{\text{true}}: 0.08$)	ϕ_c ($\phi_c^{\text{true}}: 0.125$)	
Anodic exchange current density ($J_{0,a}$)	1. 1500	—	—	—	7460 (0%)	—	—	—	1.167e-13
	2. 3500	—	—	—	7460 (0%)	—	—	—	1.167e-13
	3. 7500	—	—	—	7460 (0%)	—	—	—	1.167e-13
	4. 13500	—	—	—	7460 (0%)	—	—	—	1.167e-13
Cathodic exchange current density ($J_{0,c}$)	1. —	2000	—	—	—	1000 (0%)	—	—	1.167e-13
	2. —	3000	—	—	—	1000 (0%)	—	—	1.167e-13
	3. —	4000	—	—	—	1000 (0%)	—	—	1.167e-13
	4. —	5000	—	—	—	1000 (0%)	—	—	1.167e-13
Anode effective porosity (ϕ_a)	1. —	—	0.1	—	—	—	0.08 (0%)	—	9.807e-05
	2. —	—	0.2	—	—	—	0.08 (0%)	—	1.088e-04
	3. —	—	0.3	—	—	—	0.08 (0%)	—	3.767e-05
Cathode effective porosity (ϕ_c)	1. —	—	—	0.1	—	—	—	0.125 (0%)	1.714e-04
	2. —	—	—	0.2	—	—	—	0.125 (0%)	1.407e-04
	3. —	—	—	0.3	—	—	—	0.125 (0%)	2.023e-04

b. Multiple parameter variation

Parameter(s) to be estimated	Initial Guess					Estimates (percentage estimation error)				Best fitness function value
	$J_{0,a}$	$J_{0,c}$	ϕ_a	ϕ_c	$J_{0,a}$ ($J_{0,a}^{\text{true}}: 7460$)	$J_{0,c}$ ($J_{0,c}^{\text{true}}: 1000$)	ϕ_a ($\phi_a^{\text{true}}: 0.08$)	ϕ_c ($\phi_c^{\text{true}}: 0.125$)		
$J_{0,a}$ and $J_{0,c}$	1.	10000	2000	—	—	7626 (2.22%)	991 (-0.9%)	—	—	6.365e-02
	2.	12000	1500	—	—	7645 (2.48%)	988 (-1.2%)	—	—	1.271e-01
	3.	12000	3500	—	—	9450 (26.7%)	945 (-5.5%)	—	—	3.203e-01
$J_{0,c}$ and ϕ_a	1.	—	1500	0.1	—	—	950 (-5.00%)	0.0846 (5.75%)	—	2.707e-01
	2.	—	2500	0.1	—	—	950 (-5.00%)	0.0846 (5.75%)	—	2.707e-01
	3.	—	3500	0.1	—	—	948 (-5.20%)	0.0852 (6.50%)	—	2.742e-01
	4.	—	3500	0.2	—	—	938 (-6.20%)	0.0792 (-1.00%)	—	4.267e-01
$J_{0,a}$, $J_{0,c}$ and ϕ_a	1.	12000	1500	0.2	—	7544 (1.13%)	996 (-0.40%)	0.0802 (0.25%)	—	1.664e-02
	2.	12000	2500	0.1	—	7648 (2.52%)	990 (-1.00%)	0.0805 (0.62%)	—	3.989e-02
	3.	10000	3500	0.1	—	7694 (3.14%)	990 (-1.00%)	0.0803 (3.75%)	—	4.048e-02
$J_{0,a}$, $J_{0,c}$, ϕ_a and ϕ_c	1.	10000	1500	0.1	0.1	7702 (3.24%)	990 (-1.00%)	0.0803 (3.75%)	0.1248 (-0.16%)	3.225e-02
	2.	10000	2500	0.1	0.1	7831 (4.97%)	964 (-3.60%)	0.0836 (4.50%)	0.1654 (32.3%)	3.453e-01
	3.	12000	1500	0.1	0.1	7859 (5.35%)	977 (-2.30%)	0.0841 (5.12%)	0.1043 (-16.6%)	4.030e-01

It was shown that the solution to the inverse problem might yield incorrect values for $J_{0,a}$ when the number of design variables is more than one or when there is a large error in the initial guess. In order to further examine how significant effects of deviation in the obtained value for $J_{0,a}$ from the practical value are, single parameter estimation was performed for different values of $J_{0,a}$. In this case, the only design variable $J_{0,c}$, which was shown to have the highest effect on the polarization curve, was estimated through the inverse analysis at different values of $J_{0,a}$. The percentage error in the obtained $J_{0,c}$ as a function of the percentage deviation from the real $J_{0,a}$ is depicted in Figure 4-7. As illustrated in Figure 4-7, a large deviation in $J_{0,a}$ results in limited error in the obtained value for $J_{0,c}$. This phenomenon is in accordance with the results of the sensitivity analysis conducted on the effects of $J_{0,a}$ on the polarization curve.

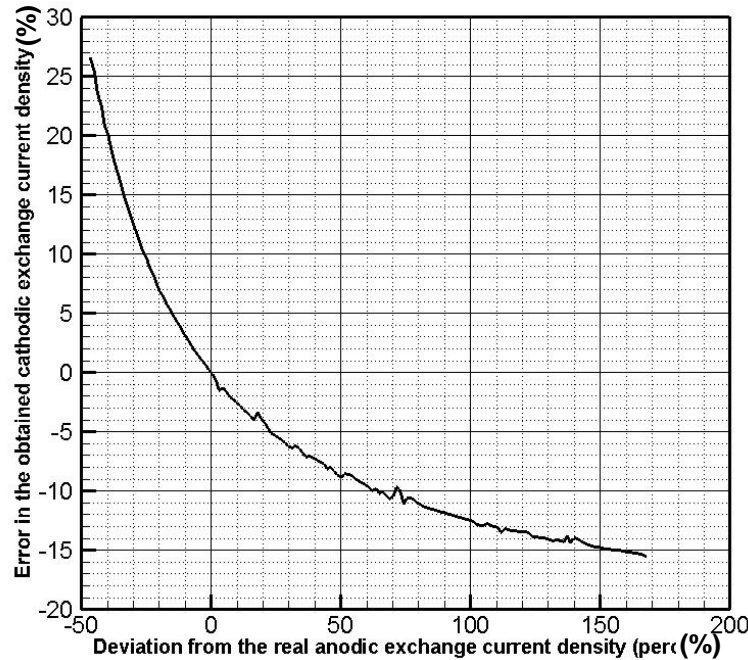


Figure 4-7. The percentage error in the obtained $J_{0,c}$ as a function of the percentage deviation from the real $J_{0,a}$

Chapter 5.

Virtual Hydrogen Sensor Development Formulation

5.1. Data Generation

The pseudo-2D model developed and validated in chapter 3 was implemented as a C++-MEX file in MATLAB for generating the data. The schematic of the high-temperature planar SOFC operating in co-flow configuration used in the study is depicted in Figure 3-4. The geometrical and electrochemical parameters of the SOFC are reported in Table 3-6 and Table 3-8, respectively. One may note that the pseudo-2D model is capable of solving the energy equation and finding the operating temperature of the cell (which is different from the inlet temperature). Solving the energy equation helps one obtain more accurate results for species concentration as temperature highly affects the diffusion of species in the porous electrodes. The activation energy on the cathode and anode sides are set identical to those used by Costamagna et al. [247]. The concentration of the reactants at the reaction sites was plotted as a function of the non-dimensional channel length in Figure 4-1. It is seen that the hydrogen and oxygen concentrations calculated with the pseudo-2D model match well with the ones obtained by the accurate 3D model [65].

As discussed earlier, nine parameters consisting of the cell voltage, cell active surface area, anode effective porosity, cathode effective porosity, inlet temperature, operating pressure at the cathode side, hydrogen mole fraction at the anode inlet, oxygen mole fraction at the cathode inlet, and the anodic total molar flow rate were chosen as input parameters of both regression and classification problems, while the percentage of the cell suffering from starvation will be the output. The range and values of input variables which would result in 480,000 data points are provided in Table 5-1.

Table 5-1. Range of different features used for generating the data set

Parameters	Range of values	Units
Voltage (V)	[0.1,1.1] with 0.1 increments	V
Active area (A_{act})	0.5, 1.0, 1.5, and 2.0	cm ²
Anode flow rate (\dot{N}_a)	[20,100] with 20 increments	sccm
Inlet oxygen concentration ($X_{O_2,i}$)	0.21 and 1.00	—
Inlet hydrogen concentration ($X_{H_2,i}$)	0.6, 0.8, 0.9, and 0.97	—
Inlet temperature (T_i)	700, 750, 800, 825, 850, 875, and 900	°C
Anode effective porosity ($\phi_{eff,a}$)	[0.1,0.2] with 0.05 increments	—
Cathode effective porosity ($\phi_{eff,c}$)	[0.1,0.2] with 0.05 increments	—
Cathode pressure (P_c)	1, 3, 5, and 10	atm
Anode pressure (P_a)	1 (fixed)	atm
Cathode molar flow rate (\dot{N}_c)	400 (fixed)	sccm

5.2. Data Preprocessing

Poor data preprocessing can have a detrimental impact on performance of machine learning algorithms [248]. Machine learning algorithms might exhibit poor performance if the features do not look alike in terms of their magnitude, range and distribution of values [248]. Indeed, it is known that if the variance of one of the features is orders of magnitude larger than the others, there is the possibility that the objective function is dominated by that feature. Consequently, the estimator (classifier or regressor) cannot learn from all features properly. Examining Table 5-1, we notice that there is a large variation in the numerical values of the input variables by as much as 4 orders of magnitude. Therefore, it is imperative that one preprocesses the data. There are two approaches to reducing the scale of the data range. One may map the data to a 0-1 range by subtracting the minimum from each value and dividing the result by the data range. An alternative approach is known as z-score normalization or standardization which is the preferred method in data science as it reshapes the input distribution to a zero-mean Gaussian (normal) distribution with unit variance [248]. Mathematically, $x_{standardized} = \frac{x_{raw} - \bar{x}}{\sigma}$, where \bar{x} and σ represent mean and standard deviation of the set, respectively [248]. This work has adopted the z-score normalization. An example of the raw (first row) and standardized (second row) data for a random point in the dataset is shown in Table 5-2. Note that the units are the same as those provided in Table 5-1. For the classification problem, all data points are being used to train the estimator. The output will be “zero” if

the cell operates in normal condition, while the starved cell is labeled as “one”. On the other hand, only data points corresponding to the starved cells are used to train the regressor. The output of the regressor will be a number between 0 and 1 that indicates the percentage of the cell which is starved at a given set of features. It should be noted that in the absence of the classifier, the regressor would receive a lot of data with no starvation for which the extent of starvation is zero. This would bias the regressor towards zero starvation, potentially reducing its accuracy. The data pre-processing and data training were performed using Sklearn, Keras v2.3.1, Numpy v1.18.1, and Pandas v1.0.1 packages in Python v3.7.6.

Table 5-2. An example of the raw and standardized data for a random point in the dataset

	A_{act}	V	P_c	\dot{N}_a	$X_{O_2,i}$	$X_{H_2,i}$	T_i	$\phi_{eff,a}$	$\phi_{eff,c}$
Raw:	1.5	0.4	5	40	0.21	0.6	850	0.1	0.2
Std:	0.448442	-0.72467	0.074205	-0.70583	-0.99898	-1.5623	0.54804	-1.2261	1.2262

5.3. Data Classification Task: Starved vs. Normal Operation

A classifier aims to classify (or label) the data into discrete bins. Classifier are trained with a pre-labeled data set of the form $D = (x_1, y_1), \dots, (x_i, y_i), \dots, (x_n, y_n)$, where x_i 's are m-dimensional vectors; y_i 's are labels corresponding to x_i 's (with the current study using two labels, '1' for starved and '0' for normal); m represents the number of inputs ($m = 9$ in the current study); and n is the number of data points ($n = 480,000$ in the current study) [249]. The relationship between x and y is not always a functional relationship and is described by the probability distribution $P(x, y)$. Considering each datapoint belonging to the dataset D as an independent sample from P, the optimum class membership will be found [250]. After standardizing the data, the 480,000 data points randomly divided into training set (consisting of 70% of the data) and test set (consisting of 30% of the data). Logistic Regression, K-Nearest Neighbors, Naïve Bayes, and ANN classifiers were trained, and the results are compared in section 5.5. Support Vector Machine (SVM), was not employed by the current study due to the huge dataset being used. While a full thesis on the difference between these methods is beyond the scope of this work, we will nonetheless highlight the key features very briefly here.

The k-nearest neighbor algorithm is a widely-used method for classification problems. The algorithm finds k data points nearest to the test data point, and calculates

the posterior probability $P(y|x)$ as the fraction of these neighbors that belong to class '1' [251]–[253]. The Naïve Bayes algorithm, also known as independence Bayes or simple Bayes, is a probabilistic classifier which is based on Bayes' theorem and maximum likelihood [254], [255]. One problem with the Naïve Bayes algorithm is making unrealistically strong independence assumptions between the features. The oversimplified nature of Naïve Bayes makes it less accurate than other classification algorithms [256]. However, Naïve Bayes is an extremely powerful classifier when there is only small training data available. The Logistic Regression, on the other hand, uses a posterior probability of the form [257]

$$P(1|x, \alpha) = \frac{1}{1 + e^{-(\alpha x)}} \quad (3)$$

Where α is a column vector with m elements. The parameters α are found such that they maximize the likelihood $\prod_{i=1}^n P(y_i|x_i, \alpha)$. The function presented in equation (3) is also called the sigmoid function with the output varying between 0 and 1. The data point x_i will be labeled as 1 if the calculated posterior probability shown in equation (3) is ≥ 0.5 , else its labeled 0 [257]. An ANN is an extension to the Logistic Regression model consisting of multiple layers of “neurons”. Each ANN consists of input neurons that receive the components of x as input. The weighted sum of neurons in the input layer is fed to the neurons in the hidden layer. If there are multiple hidden layers, the weighted sum of outputs of neurons in each hidden layer is fed to the neurons in the next hidden layer, and the weighted sum of outputs of the neurons in the last hidden layer is fed to the output layer. An ANN with just one output layer (no hidden layers) operating with sigmoid function acts exactly the same as Logistic Regression. An ANN is trained by selecting the various weights in a process called back-propagation to minimize output prediction error [258]. Schematic of the ANN employed by the current study is depicted in Figure 5-1. Note that the number of nodes in the first and second hidden layers changed between 2 and 9 in the current study. Figure 5-1 represents the case with 8 neurons in both hidden layers. The case with more than two hidden layers was not considered for avoiding complexity, overfitting, and very long training times. There is an activation function acting at all hidden layers, as well as the output layer, to find the output signal of each neuron. The Rectified Linear Unit function, defined as $ReLU = \max(0, x)$, was employed for the neurons in the hidden layer while the sigmoid function was used at the output neuron. Using Rectified

Linear Unit function is beneficial in the sense that it does not activate all the neurons at the same time, which is more computationally efficient. During training an ANN, all of the weights are randomly initialized. Thereafter, the output signal is evaluated for each datapoint in the training set. After finding the output for N_e data points, where N_e is called number of epochs, the error is found by the binary cross-entropy function [259]. The calculated error (loss) is then used to update the weights of the network through back-propagation. The trained neural network is finally applied to the test set in order to find the accuracy of the network.

Accuracy of a classifier is defined as the ratio of the number of correct estimations to the total number of data points in the test set. Many researchers have used accuracy as a metric for validating their classification models. However, the accuracy of the model does not necessarily guarantee the effective performance, especially when classes are skew. For our performance metric, we first calculate the binary confusion matrix ([260]–[262]) shown in Table 5-3. Here, the “true class” refers to the true state operation of the fuel cell, while the inferred class refers to the predicted state operation of the fuel cell. TP (true positive) refers to a starved data point correctly classified as starved, while TN (true negative) refers to the normal data point being correctly classified as normal. On the other hand, if an observation is falsely classified into a negative or positive class, it is marked as FN (false negative) and FP (false positive), respectively. Using the confusion matrix, “Recall” (also known as sensitivity, hit rate, or true positive rate) is calculated as:

$$\text{Recall} = \text{True Positive Rate (TPR)} = \frac{\text{TP}}{\text{TP} + \text{FN}} \quad (2)$$

while precision or positive predictive value is defined as:

$$\text{Precision} = \text{Positive Predictive Value (PPV)} = \frac{\text{TP}}{\text{TP} + \text{FP}} \quad (3)$$

While it would be desirable to maximize both metrics, it is widely understood that there is a trade-off between maximizing recall and maximizing precision [260]–[262]. In order to combine the effects of these two factors, F1 score is evaluated as the Harmonic mean of TPR and PPV as follows:

$$\text{F1 score} = \frac{2 \cdot \text{TPR} \cdot \text{PPV}}{\text{TPR} + \text{PPV}} = \frac{2 \cdot \text{TP}}{2 \cdot \text{TP} + \text{FP} + \text{FN}} \quad (4)$$

Validation of the trained classifier can be done once all the performance indicators are calculated. It should be noted that the validation metric is only calculated for the test set, and none of the observations from the training set were used for finding the performance indicators.

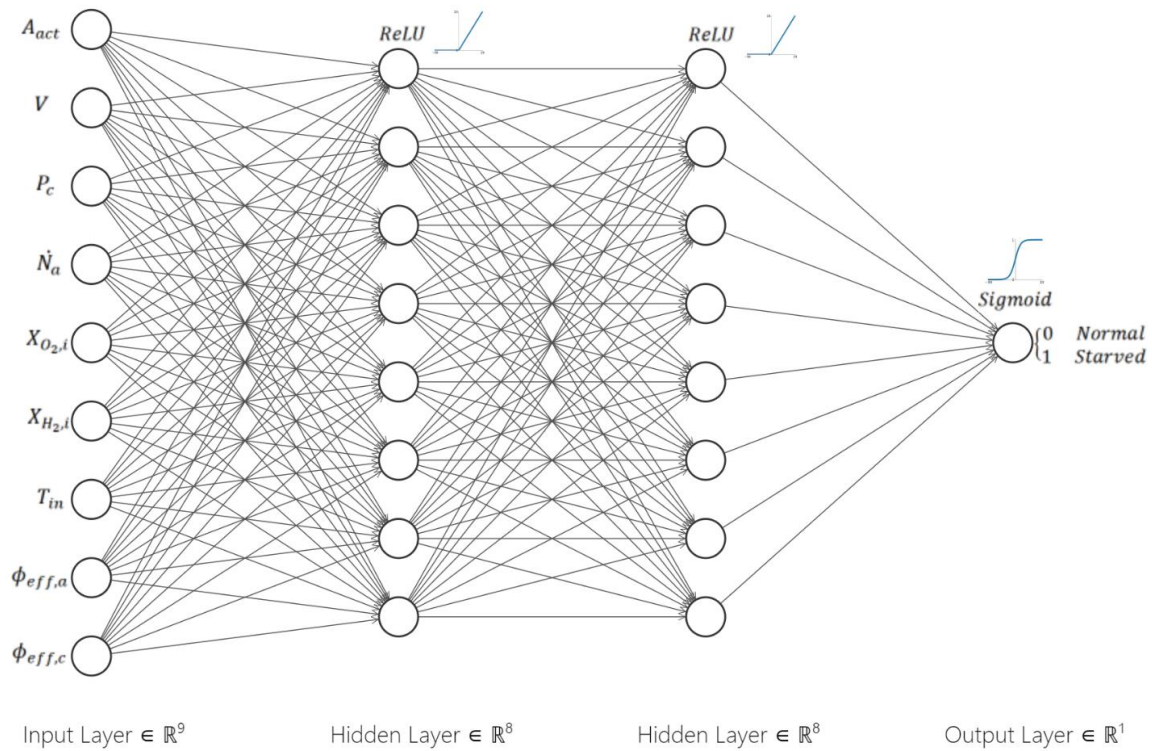


Figure 5-1. The neural network used for the classification

Table 5-3. Confusion matrix for the classification problem

		Inferred Class	
		Starved (1)	Normal (0)
True Class	Starved (1)	True Positive (TP)	False Negative (FN)
	Normal (0)	False Positive (FP)	True Negative (TN)

5.4. Data Regression Task: Percentage of the Cell Starved

In this section, an ANN was employed to find the percentage of the cell which is starved. For improved clarification, we will use a subscript 'r' to denote the ANN used for regression (i.e. ANN_r). The ANN_r employed for the regression task is almost the same as the one presented in Figure 5-1. Rather than using the entire dataset, the ANN_r was only trained and validated on the starved data. The classifiers were used to figure out if the cell operates in normal or starved condition. If the cell is marked as “starved” by the classifier, the ANN_r will be used to evaluate the percentage of the cell suffering from hydrogen starvation, as shown in Figure 5-2.

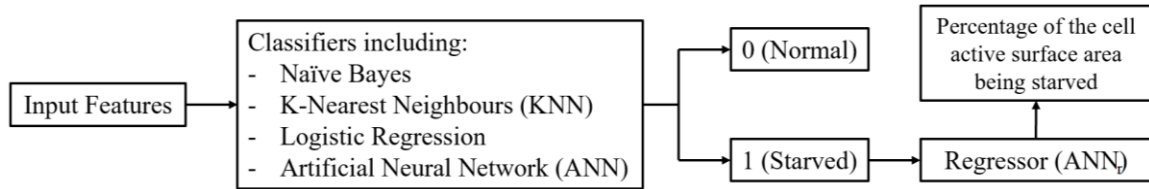


Figure 5-2. Schematic of the virtual hydrogen sensor proposed in this study

Since “the percentage of the cell active surface area being starved” is a continuous variable, a linear activation function is used at the output layer instead of the sigmoid function that was utilized for the binary classification problem. The input data (x values) used for training the regressor is the same as what was used for classification. The process of training will be continued until the desired accuracy is achieved. The mean squared error (MSE) presented in equation 5 was used as the loss/cost function for the regressor that needed to be minimized.

$$\text{MSE} = \frac{1}{N} \sum_{i=1}^N (y - \hat{y})^2 \quad (5)$$

Where y is the vector of observed values and \hat{y} represents the estimated values. The process of training the neural network is done by calculating and minimizing the MSE. The mean absolute error (MAE) defined in equation 6, was evaluated for the test set for the purpose of validation.

$$\text{MAE} = \frac{1}{N} \sum_{i=1}^N |y - \hat{y}| \quad (6)$$

The regression task was firstly done using the whole data set, i.e. including both starved and normal observations. The trained regressor had very high MSE and MAE, indicating extremely low accuracy. It was determined that the presence of several datapoints with no starvation heavily biased the training. Technically, the regressor is being used to yield a number between zero and one as the ratio of the cell being starved. Therefore, all the cells operating in normal condition with y values equal to zero will dominate the weights of the network. In order to solve this issue, the regressor was again trained, but this time using the starved data. Taking the mentioned approach is practical in the sense that the classifier can be used to determine if the cell is starved or not. Once the cell performance is found to deviate from the normal condition, the regressor is used to estimate the ratio of the cell active area prone to hydrogen starvation. Control strategies can then be employed according to the requirements in terms of minimum starvation ratio being allowed during the operation. Convergence history of the regression problem for the neural network with 8 neurons in both hidden layers based on the test set MSE is shown in Figure 5-3. The convergence plots for the classification problem were omitted for brevity. According to Figure 5-3, the solution has almost converged after 150 epochs where MSE stayed constant at 4.8×10^{-3} .

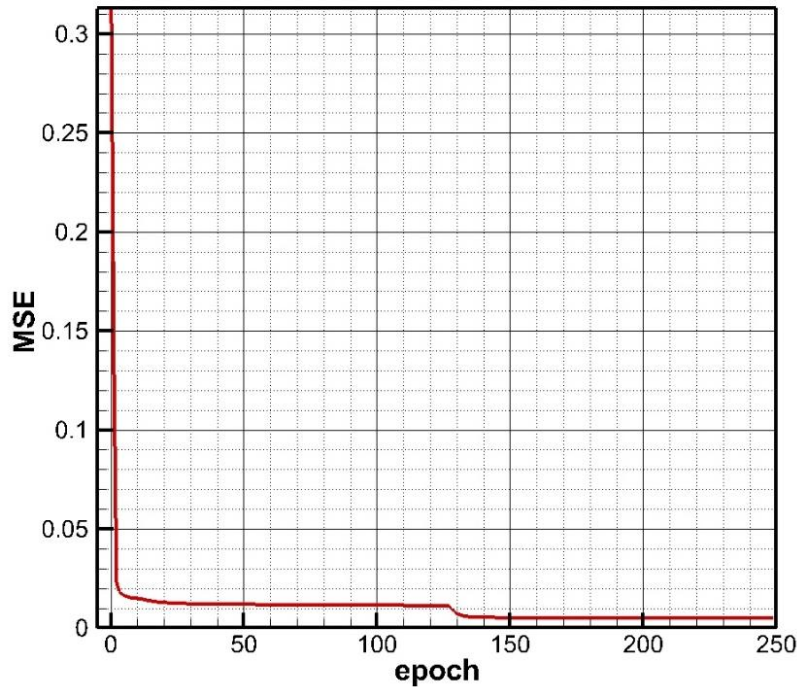


Figure 5-3. Convergence history of the test set for the regression problem based on MSE

5.5. Data Classification and Regression Results

5.5.1. Classification Results

In this section, the performance of the classifiers is presented. For the classification problem, Naïve Bayes algorithm gave the least accurate results. The confusion matrix obtained by the Naïve Bayes algorithm is shown in Table 5-4:

Table 5-4. Confusion matrix obtained by the Naïve Bayes algorithm

Confusion Matrix for Naïve Bayes Method		Inferred Class	
		Starved (1)	Normal (0)
True Class	Starved (1)	25739	3790
	Normal (0)	4683	62556

According to Table 5-4, precision, recall, and F1-Score of the Naïve Bayes are found to be 0.846, 0.872, and 0.859, respectively. On the other hand, classification performance indicators of both Logistic Regression and KNN are compared in Figure 5-4. Performance indicators for Naïve Bayes are not mentioned in Figure 5-4 due to low accuracy. As shown

in Figure 5-4, the optimum value of $k = 21$ results in the best performance for the KNN method. One should also note that KNN outperforms both Naïve Bayes and Logistic Regression methods for any value of k . Furthermore, KNN with appropriately tuned k value yielded considerably higher performance indicators in comparison with both Naïve Bayes and Logistic Regression algorithms. Finally, neural networks with various numbers of neurons in the first and second hidden layers were trained in order to find the optimum number of neurons in each layer. The F1-Scores of the neural networks are shown in Figure 5-5.

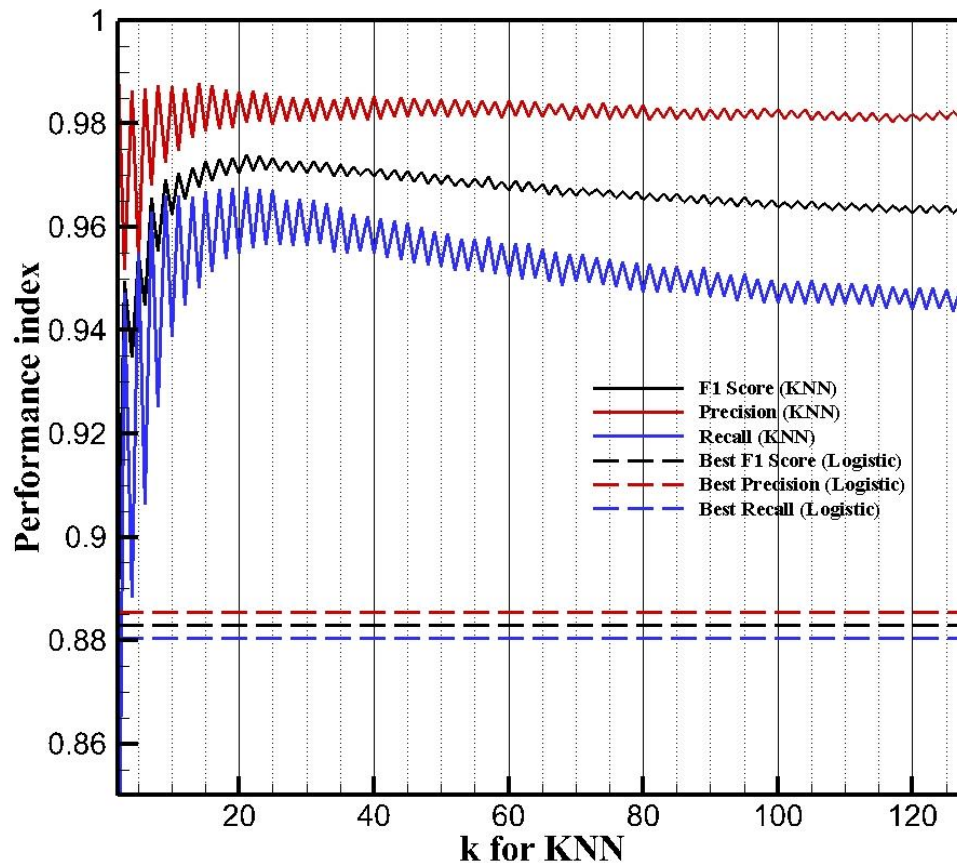


Figure 5-4. Comparison of performance indicators for the KNN with Logistic Regression methods

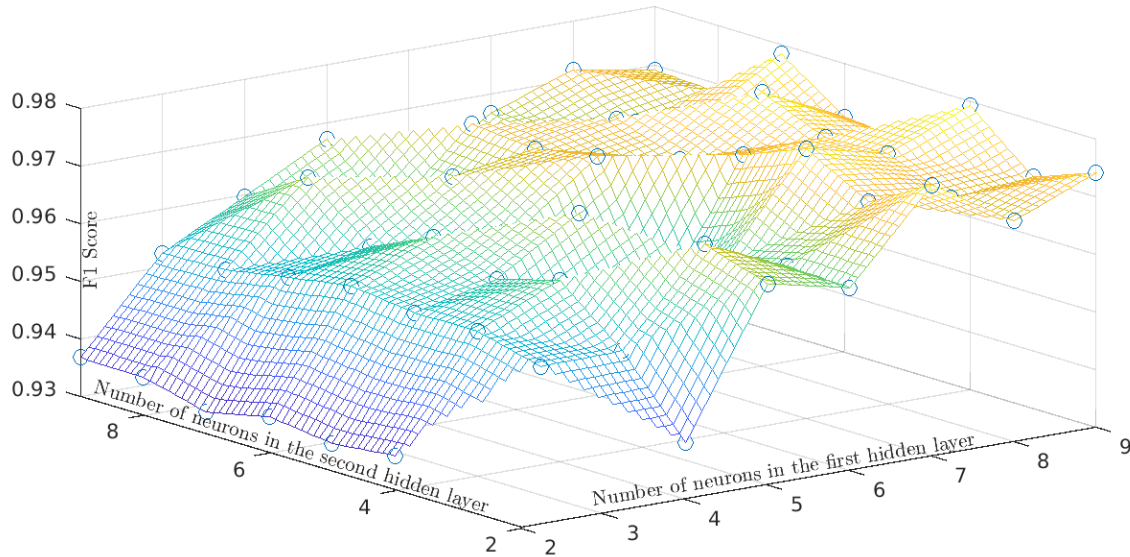


Figure 5-5. The F1-Score corresponding to the ANN for different number of neurons in each hidden layer

According to Figure 5-5, at least 8 and 6 neurons in the first and second hidden layers, respectively, are required to ensure an F1-Score above 0.97 for the classification problem using the ANN. It is also worth mentioning that the KNN can compete with ANN in terms of classifying the cell performance into “normal” or “starved”. However, ANN slightly outperformed the KNN when using the appropriate structure for the neural network by one percent. According to the information presented through Table 5-4, Figure 5-4, and Figure 5-5 it is evident that both KNN and ANN can be successfully utilized for identifying the starvation. However, KNN needs longer training time as the Euclidean distance of each point with all other points in the data set should be found at each iteration. Naïve Bayes and Logistic Regression can be used for classification as well, but only when an F1-Score above 0.9 is not required. Optimum results for each classifier are provided in Table 5-5.

Table 5-5. Comparison of performance indicators for different classifiers in detecting incidence of fuel starvation

Classifier	Best Precision	Best Recall	Best F1 score
Naïve Bayes	0.846	0.872	0.859
Logistic Regression	0.885	0.881	0.883
KNN	0.980	0.966	0.973
ANN	0.985	0.971	0.979

5.5.2. Regression Results

Next, we will examine the results for the regressor to predict the extent of starvation. Figure 5-6 plots the accuracy of the ANN_r for different number of neurons in the first and second hidden layers (as measured by MAE). The results indicate that the number of neurons in both hidden layers should be above 6 to ensure accuracy (based on the MAE) above 95 percent. Comparing the ANNs trained for the classification and regression problems, one can conclude that the F1 score of the classification problem is not always an increasing function of the number of neurons in the second hidden layer, while this is the case for the accuracy of the regression problem (at least for small number of neurons in the second hidden layer). Therefore, the performance of the network depends on the number of neurons in the second layer for the case of regression while the classification can be still done without using the second hidden layer. According to the results, the classifier is able to accurately detect the starvation. Since Ni oxidation is highly correlated with hydrogen starvation [24], [161], by virtue of the high accuracy of more than 97 percent, the trained model can predict the SOFC region prone to Ni oxidation. Therefore, the pair of classifier-regressor introduced in this work successfully acts as a virtual hydrogen sensor for online tracking of the hydrogen concentration along the cell.

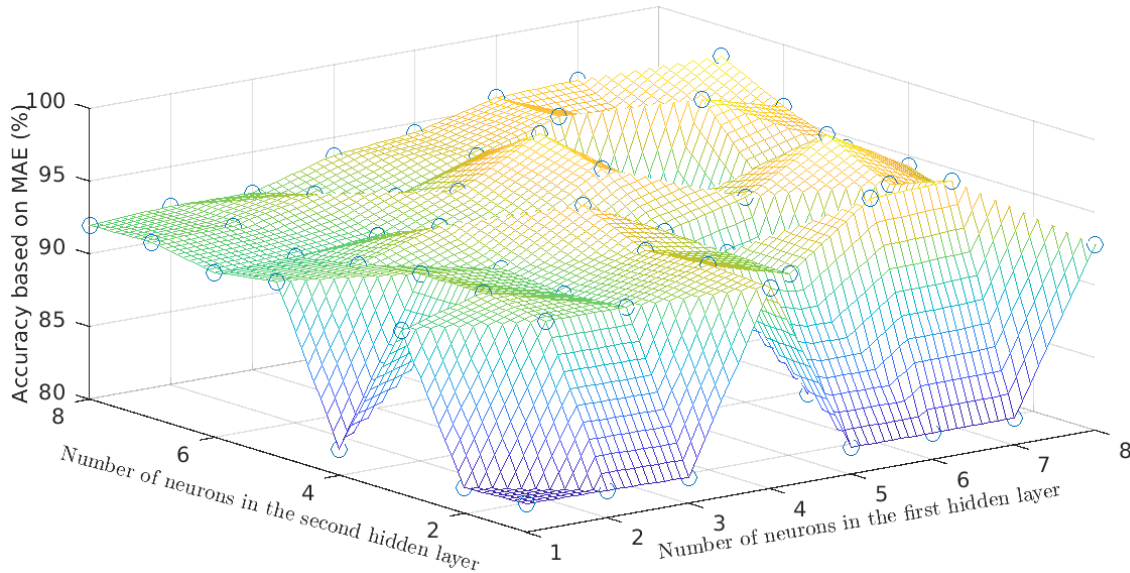


Figure 5-6. The test set accuracy of the ANN_r calculated based on the MAE

From Figure 5-6 it is seen that the optimal neural network consists of the configuration with eight neurons in the first hidden layer, and seven neurons in the second hidden layer. It may be noted that the output of each neuron, i , is calculated as $y_i = \mathcal{A}(\sum W_{i,j}x_j + b_i)$, where \mathcal{A} is the activation function, $W_{i,j}$ refers to the weight that is multiplied by the i^{th} neuron in that layer used to calculate the output of the j^{th} neuron in the following layer, and b_i is the bias. Table 5-6 shows the weighting matrices and bias for the different layers of the optimal neural network. Note that these matrices should be applied to the standardized and normalized input vector based on the data provided in Table 5-1.

Table 5-6. Weight matrices of the optimum neural network with nine input neurons, eight neurons in the first hidden layer, and seven neurons in the second hidden layer. HAa corresponds to the Ath neuron in the ath hidden layer.

Matrix of weights connecting the input layer to the first hidden layer								
Layer 1 →	H1 ₁	H2 ₁	H3 ₁	H4 ₁	H5 ₁	H6 ₁	H7 ₁	H8 ₁
Bias (1)	0.0220	0.3821	0.1986	0.3311	0.4446	0.2543	0.6349	-0.2734
Inputs ↓								
A _{act}	0.1534	0.0162	-0.3190	0.0895	0.1321	0.1512	0.0021	-0.0271
V	-0.4184	-0.0306	-0.3962	-0.1160	-0.1869	-0.4082	-0.0797	-0.1203
P _c	-0.0268	-0.1901	0.1540	-0.0094	0.0056	-0.0419	0.1651	-0.3947
N _a	-0.0968	0.4264	0.0457	-0.2468	-0.1673	-0.1197	0.1855	0.0531
X _{O₂,i}	-0.6201	-0.0096	0.0819	-0.3391	0.2427	0.7564	0.0222	0.0257
X _{H₂,i}	0.0061	0.0656	-0.0008	-0.0163	0.0146	0.0081	0.0372	-0.0135
T _{in}	0.0573	-0.0939	0.0590	0.1465	0.1853	0.0619	0.0617	-0.0014
Φ _{eff,a}	0.0451	0.0201	-0.0765	0.0136	0.0047	0.0609	-0.1057	-0.0724
Φ _{eff,c}	0.0000	0.0002	-0.0029	-0.0011	0.0004	-0.0012	-0.0019	-0.0037

Matrix of weights connecting the first hidden layer to the second hidden layer							
Layer 2 →	H1 ₂	H2 ₂	H3 ₂	H4 ₂	H5 ₂	H6 ₂	H7 ₂
Bias (1)	0.140878	0.137754	-0.07366	-0.01432	0.136232	0.428837	-0.46937
Layer 1 ↓							
H1 ₁	0.246711	0.308855	-0.37222	-0.05076	0.29747	-0.36572	0.253609
H2 ₁	0.307311	0.257533	0.010117	-0.04704	0.274051	-0.07993	0.002275
H3 ₁	-0.02209	0.006349	0.205899	-0.0583	0.00226	0.432076	0.035871
H4 ₁	0.238801	0.228487	-0.03497	-0.01565	0.216718	-0.13937	0.070381
H5 ₁	0.324863	0.31422	-0.0465	0.005582	0.283322	-0.11904	0.015197
H6 ₁	0.267497	0.279421	-0.35156	-0.05443	0.347365	-0.36821	0.264745
H7 ₁	0.16913	0.106282	0.57131	-0.0048	0.112995	-0.39812	0.406462
H8 ₁	0.105326	0.108682	-0.50069	0.019647	0.186085	-0.14848	-0.05092

Matrix of weights connecting the second hidden layer to the output layer (first column represents the bias weight)								
	Bias (1)	H1 ₂	H2 ₂	H3 ₂	H4 ₂	H5 ₂	H6 ₂	H7 ₂
Output	0.106408	0.259376	0.274962	-0.99903	-0.03094	0.273015	-1.15387	-0.92201

5.5.3. Effect of Misclassified Data Input

The F1-score for the most accurate classifier was 0.98 (refer from Figure 5-5). It stands to reason that some normal data points (nearly 2 percent) may be misclassified by the classifier and passed on to the ANN_r. Since the ANN_r was not trained with these “normal” data points, it is important to analyze the ANN_r performance for these possible error-inputs. To this end, Figure 5-7 plots the output of ANN_r to all the normal data (i.e. all data with true class being normal, not just the misclassified data). It is seen from this figure that ANN_r will give negative values for the ratio of the cell active area being starved for a normal operating point (the maximum value reported in Figure 5-7 is less than 0.001). Therefore, if the regressor gives a negative number as the output, it will be an indication of that point being a normal operating point which is labeled by the classifier as starved by mistake.

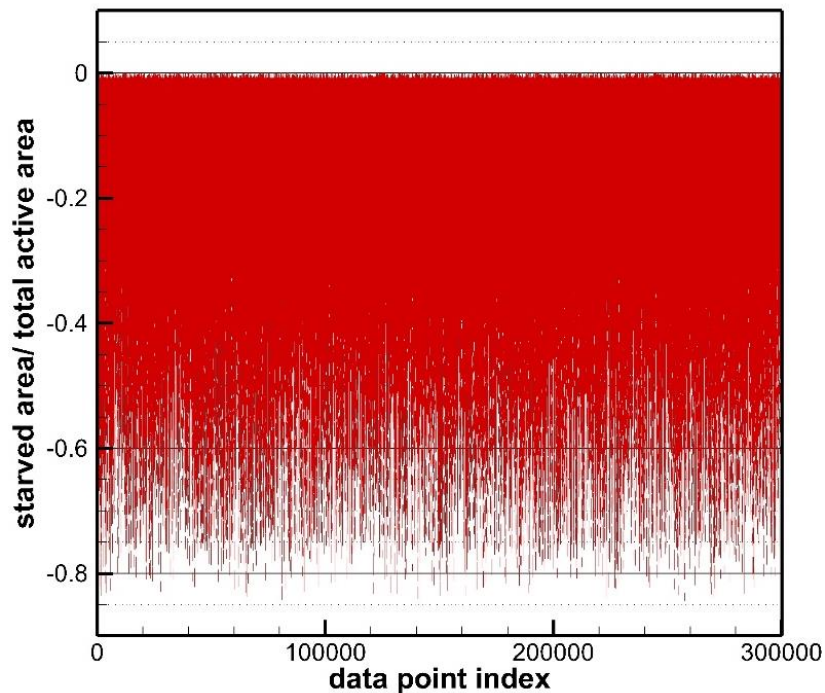


Figure 5-7. Regression results for “normal” operating points

5.5.4. Validation of the Virtual Sensor

The optimal trained neural networks were employed to find the ratio between the starved area and the total active area in a virtual experiment. The virtual experiment was performed at anode flow rate of $\dot{N}_a = 30 \text{ sccm}$, cathode pressure of $P_c = 1 \text{ atm}$, and cell temperature of $T = 860 \text{ }^\circ\text{C}$, with active area of 0.5 cm^2 and effective porosity of 0.12. While using pure oxygen as the oxidizer, hydrogen mole fraction at the anode inlet was set to 0.85. The voltage was gradually increased and the extent of hydrogen starvation (ratio of starved area to total active area) was compared and plotted in Figure 5-8. It is seen from Figure 5-8 that at very high values of cell voltage (resulting from the no load condition), no hydrogen starvation was noticed by either the real model or the virtual sensor. Reducing the cell voltage (increasing the load) firstly results in part of the cell being starved around $V=0.56 \text{ [V]}$. Further decreasing the voltage increases the starved area until at $V=0 \text{ [V]}$ (limiting current) nearly the whole length of the cell suffers from hydrogen starvation. One may note that other input parameters were kept constant at values not used for training the neural networks to further examine the robustness of the method. Comparing the data obtained by regressor/classifier pair with the values obtained by the model, it is evident that the virtual sensor can be effectively utilized for predicting both the incidence and the extent of hydrogen starvation in SOFCs. One may note that voltage was changed in 0.02 [V] increments to obtain the data in Figure 5-8, while the network was trained using the data generated with voltage values changing in 0.1 [V] increments. However, the results are still very close, and this further demonstrates the robustness of the developed virtual sensor.

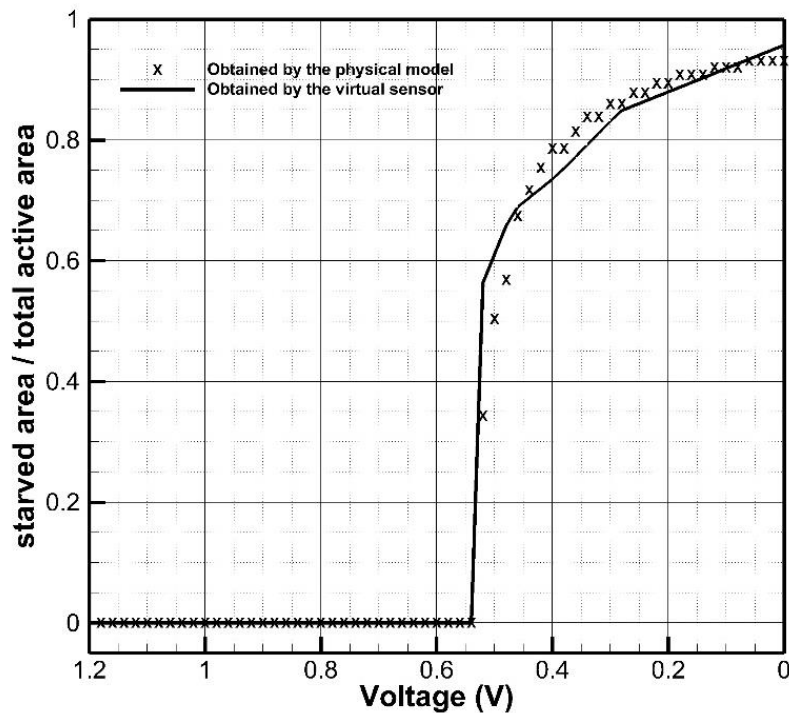


Figure 5-8. Validation of ANNr based virtual hydrogen sensor.

Although the classifier-regressor pair in this thesis is accurate and robust in terms of following the data behavior, it is worth mentioning that the pair is trained using the data generated by the model and the model is accurate when starvation has not happened to a very high extent for some quite long time. Operating in the starved region for a long time will result in irreversible processes that might cause even cell voltage reversal before complete mechanical failure of the electrolyte occurs. In that case, the model used for generating the data should be able to follow the starvation voltage-wise which was not the case for the current work since voltage was an input of the model.

Chapter 6.

Conclusion

In this study, a single cell of a planar SOFC was firstly simulated in 3D using the commercial SOFC module of ANSYS Fluent and the results were validated against the experimental investigations in the literature. Besides, a step-by-step procedure for using SOFC module was presented, providing readers with a deep insight into the software. All material properties, geometry modeling, meshing size, flow zone types, and solver settings were precisely discussed. After doing the simulations in 3D, it was shown that 3D model introduced here is capable of solving mass, momentum, energy, electric potential, and species equations properly. Furthermore, it was indicated that temperature gradients along the cell are so small that one can ignore them without any loss of precision, assuming that cell temperature is constant along the cell. Thereafter, the simplified quasi-2D method was developed for modeling a single cell of the SOFC. Notwithstanding the numerous assumptions made in the pseudo-2D case, the solution for quasi-2D code converged to the same solution given by the 3D model in a very faster fashion. Furthermore, maximum error observed in the model was bounded within less than 6 percent which was the case for intermediate values of current density. Therefore, the pseudo-2D code can be efficiently used as an alternate method for finding the polarization curve of the cell. A pattern search based inverse algorithm was applied to the polarization curve given by the simplified pseudo-2D model to estimate electrodes microstructural properties. An inverse algorithm with the appropriate objective function was introduced followed by a sensitivity analysis conducted to study the effects of the design variables on the cell polarization curve. Anodic and cathodic exchange current densities, as well as the anode and cathode porosities, were successfully estimated by the inverse approach in the way that minimizes the difference between the actual polarization curve and the one corresponding to each set of unknown design variables. One may note that the exact same procedure can be applied to a stack model rather than a single cell as long as a fast and reliable SOFC stack solver is available for conducting the direct simulation. The following conclusions were drawn based on the results:

- The cell polarization curve was greatly sensitive to the cathodic exchange current density and anode effective porosity, while it was insignificantly affected by the

anodic exchange current density. Also, the effect of cathode porosity was found to be minimal.

- Using the introduced representation of the error was found to be a suitable approach for defining the fitness function when the cell polarization curve is used for the inverse parameter estimation. Generally, oscillations were either smoothed or completely removed when using the proposed fitness function.
- The pattern search method was effectively incorporated into the inverse analysis to capture an accurate set of unknown design variables, whereas the genetic algorithm and the simulated annealing optimization techniques failed to do so.
- In the case of optimization with more than two design variables and a significantly inaccurate initial guess, deviation from the real values might be observed for the parameters to which the polarization curve is not considerably sensitive.
- It was shown that the optimization problem is not sensitive to the upper limit of the design variables for the case of exchange current densities.
- Different values of the initial guesses for the optimization problem should be used in order to correctly describe the effectiveness of the inverse method in estimating the unknown parameters.

In addition to finding the polarization curve, the pseudo-2D model was capable of finding the hydrogen concentration distribution along the channels of SOFC. Thanks to the very fast and accurate performance of the pseudo-2D model, a huge data set of 480,000 data points was generated. Nine features including the cell voltage, the cell active surface area, anode effective porosity, cathode effective porosity, inlet temperature, operating pressure at the cathode side, hydrogen mole fraction at the anode inlet, oxygen mole fraction at the cathode inlet, and the anodic total molar flow rate were chosen to change for each data point. The goal of the study was to see if machine learning can be used to first detect, and then estimate the portion of the cell suffering from starvation using ANN. The dependent variable will be binary for the classification problem while it will be a number between zero and one for the regression case. Different classifiers including Naïve Bayes, Logistic Regression, KNN, and ANN were used for the classification while the ANN was utilized for regression. The following conclusions are made:

- In order to achieve high accuracy, the regressor should be trained using only the starved data. The classifier, however, should be fed by the whole data set.

- The ANN and KNN outperform Naïve Bayes and Logistic Regression methods for the classification problem.
- Tuning the parameter k in the KNN algorithm highly increases the F1-Score of the classifier.
- Tuning the number of neurons in hidden layers of the ANN increases the F1-Score of the classifier.
- The KNN, although simple, competes with ANN in terms of performance and accuracy.
- ANN with one hidden layer can be used for the classification problem, while two hidden layers should be utilized for the regression.
- The pair of classifier-regressor introduced in this work successfully acts as a virtual hydrogen sensor for online tracking of the hydrogen concentration along the cell.

Chapter 7.

Recommendations for future works

7.1. Developing the pseudo-2D model for a button-cell SOFC

The model developed in this work corresponds to an anode-supported planar cell. Developing the same model for button-cell configuration will be beneficial in the sense that it would be easier and more practical to build an experimental setup for a button-cell SOFC. The model can then be validated against the experimental results and be used by the inverse algorithm to estimate porosity of GDL materials. The challenge for applying the pseudo-2D model to a button-cell would be the addition of incoming species as we move radially outward through the nodes.

7.2. Extending the pseudo-2D model for studying the stack dynamic operation

The model presented in this thesis corresponds to steady state performance of a single cell. It would be useful to develop the same model for dynamic operations so that it can be used for online control purposes since time derivative of the state (control) variables is required for designing a control. In order to achieve this goal, a good point to start from will be comparing the time constants of voltage, current, temperature, and species concentrations dynamic response. It is mentioned in the literature that the temperature time constant is larger than the others, and at least the energy equation must be solved for the dynamic mode even if a lumped temperature is assumed for the cell. Once the dynamic response of the system is modelled for a single cell, the results will be extendable for stack operation.

7.3. Developing a virtual oxygen sensor for predicting oxygen starvation in PEMFCs

Oxygen starvation on the cathode side of PEMFCs is an issue that have attracted researchers' attention recently. Using the same procedure employed in this thesis, the

same pair of classifier-regressor can be trained based on either simulation or experimental data for a PEMFC. Since oxygen starvation results in hydrogen pumping and cathodic hydrogen emissions in PEMFCs, developing such a virtual sensor will be beneficial in terms of safety concerns prevent excessive hydrogen emissions at the cathode side.

References

- [1] IEO, "International Energy Outlook 2017," [https://www.eia.gov/outlooks/ieo/pdf/0484\(2017\).pdf](https://www.eia.gov/outlooks/ieo/pdf/0484(2017).pdf), 2017. [Online]. Available: [https://www.eia.gov/outlooks/ieo/pdf/0484\(2017\).pdf](https://www.eia.gov/outlooks/ieo/pdf/0484(2017).pdf).
- [2] S. Yadav, M. K. Singh, and K. Sudhakar, "Modelling of Solid Oxide Fuel Cell- A Review," *Int. J. Sci. Eng. Res.*, vol. 6, no. 4, pp. 834–841, 2015, doi: 10.5541/ijot.71377.
- [3] M. Rokni, "Plant characteristics of an integrated solid oxide fuel cell cycle and a steam cycle," *Energy*, vol. 35, no. 12, pp. 4691–4699, 2010, doi: 10.1016/j.energy.2010.09.032.
- [4] C. Sun and U. Stimming, "Recent anode advances in solid oxide fuel cells," *J. Power Sources*, vol. 171, no. 2, pp. 247–260, 2007, doi: 10.1016/j.jpowsour.2007.06.086.
- [5] K. H. J. Buschow, *Encyclopedia of materials : science and technology*. Elsevier, 2001.
- [6] N. Chitose *et al.*, *Journal of the Electrochemical Society.*, vol. 151. Electrochemical Society, 1948.
- [7] D. Bhattacharyya and R. Rengaswamy, "A Review of Solid Oxide Fuel Cell (SOFC) Dynamic Models," *Ind. Eng. Chem. Res.*, vol. 48, no. 13, pp. 6068–6086, Jul. 2009, doi: 10.1021/ie801664j.
- [8] C. J. Steffen, J. E. Freeh, and L. M. Larosiliere, "Solid Oxide Fuel Cell/Gas Turbine Hybrid Cycle Technology for Auxiliary Aerospace Power," in *Volume 5: Turbo Expo 2005*, Jan. 2005, pp. 253–260, doi: 10.1115/GT2005-68619.
- [9] J. E. Freeh, J. W. Pratt, and J. Brouwer, "Development of a Solid-Oxide Fuel Cell/Gas Turbine Hybrid System Model for Aerospace Applications," in *Volume 7: Turbo Expo 2004*, Jan. 2004, pp. 371–379, doi: 10.1115/GT2004-53616.
- [10] V. Liso, A. C. Olesen, M. P. Nielsen, and S. K. Kær, "Performance comparison between partial oxidation and methane steam reforming processes for solid oxide fuel cell (SOFC) micro combined heat and power (CHP) system," *Energy*, vol. 36, no. 7, pp. 4216–4226, Jul. 2011, doi: 10.1016/J.ENERGY.2011.04.022.
- [11] M. Rokni, "Thermodynamic analysis of SOFC (solid oxide fuel cell)–Stirling hybrid plants using alternative fuels," *Energy*, vol. 61, pp. 87–97, Nov. 2013, doi: 10.1016/J.ENERGY.2013.06.001.

- [12] Y. Komatsu, S. Kimijima, and J. S. Szmyd, "Performance analysis for the part-load operation of a solid oxide fuel cell–micro gas turbine hybrid system," *Energy*, vol. 35, no. 2, pp. 982–988, Feb. 2010, doi: 10.1016/J.ENERGY.2009.06.035.
- [13] R. A. Roberts and J. Brouwer, "Dynamic Simulation of a Pressurized 220 kW Solid Oxide Fuel-Cell–Gas-Turbine Hybrid System: Modeled Performance Compared to Measured Results," *J. Fuel Cell Sci. Technol.*, vol. 3, no. 1, p. 18, Feb. 2006, doi: 10.1115/1.2133802.
- [14] W. R. Dunbar, N. Lior, and R. A. Gaggioli, "Combining fuel cells with fuel-fired power plants for improved exergy efficiency," *Energy*, vol. 16, no. 10, pp. 1259–1274, Oct. 1991, doi: 10.1016/0360-5442(91)90155-F.
- [15] C. Bang-Møller, M. Rokni, B. Elmegaard, J. Ahrenfeldt, and U. B. Henriksen, "Decentralized combined heat and power production by two-stage biomass gasification and solid oxide fuel cells," *Energy*, vol. 58, pp. 527–537, Sep. 2013, doi: 10.1016/J.ENERGY.2013.06.046.
- [16] C. Sun and U. Stimming, "Recent anode advances in solid oxide fuel cells," *J. Power Sources*, vol. 171, no. 2, pp. 247–260, 2007, doi: 10.1016/j.jpowsour.2007.06.086.
- [17] J. I. Gazzarri and O. Kesler, "Electrochemical AC impedance model of a solid oxide fuel cell and its application to diagnosis of multiple degradation modes," *J. Power Sources*, vol. 167, no. 1, pp. 100–110, 2007, doi: 10.1016/j.jpowsour.2007.02.010.
- [18] T. J. Gatts, "Investigation of the Heating and Cooling of Composite Glass Seals for SOFCs," Ohio State University, 2008.
- [19] C.-K. Lin, T.-T. Chen, Y.-P. Chyou, and L.-K. Chiang, "Thermal stress analysis of a planar SOFC stack," *J. Power Sources*, vol. 164, no. 1, pp. 238–251, 2007, doi: 10.1016/j.jpowsour.2006.10.089.
- [20] K. . Recknagle, R. . Williford, L. . Chick, D. . Rector, and M. . Khaleel, "Three-dimensional thermo-fluid electrochemical modeling of planar SOFC stacks," *J. Power Sources*, vol. 113, no. 1, pp. 109–114, 2003, doi: 10.1016/S0378-7753(02)00487-1.
- [21] G. Wang, Y. Yang, H. Zhang, and W. Xia, "3-D model of thermo-fluid and electrochemical for planar SOFC," *J. Power Sources*, vol. 167, no. 2, pp. 398–405, 2007, doi: 10.1016/j.jpowsour.2007.02.019.
- [22] M. Iwata *et al.*, "Performance analysis of planar-type unit SOFC considering current and temperature distributions," *Solid State Ionics*, vol. 132, no. 3–4, pp. 297–308, Jul. 2000, doi: 10.1016/S0167-2738(00)00645-7.

- [23] G. Brus, K. Miyawaki, H. Iwai, M. Saito, and H. Yoshida, "Tortuosity of an SOFC anode estimated from saturation currents and a mass transport model in comparison with a real micro-structure," *Solid State Ionics*, vol. 265, pp. 13–21, Nov. 2014, doi: 10.1016/J.SSI.2014.07.002.
- [24] G. Brus, K. Miyoshi, H. Iwai, M. Saito, and H. Yoshida, "Change of an anode's microstructure morphology during the fuel starvation of an anode-supported solid oxide fuel cell," *Int. J. Hydrogen Energy*, vol. 40, no. 21, pp. 6927–6934, Jun. 2015, doi: 10.1016/J.IJHYDENE.2015.03.143.
- [25] M. Secanell, J. Wishart, and P. Dobson, "Computational design and optimization of fuel cells and fuel cell systems: A review," *J. Power Sources*, vol. 196, no. 8, pp. 3690–3704, 2011, doi: 10.1016/j.jpowsour.2010.12.011.
- [26] P. Liu, Z. Luo, J. Kong, X. Yang, Q. Liu, and H. Xu, "Ba_{0.5}Sr_{0.5}Co_{0.8}Fe_{0.2}O_{3-δ}-based dual-gradient cathodes for solid oxide fuel cells," *Ceram. Int.*, vol. 44, no. 4, pp. 4516–4519, Mar. 2018, doi: 10.1016/J.CERAMINT.2017.12.034.
- [27] X. Shao *et al.*, "High performance anode with dendritic porous structure for low temperature solid oxide fuel cells," *Int. J. Hydrogen Energy*, vol. 43, no. 37, pp. 17849–17856, Sep. 2018, doi: 10.1016/J.IJHYDENE.2018.07.171.
- [28] S. Miller, X. Xiao, J. Setlock, S. Farmer, and K. Faber, "Freeze-cast yttria-stabilized zirconia pore networks: Effects of alcohol additives," *Int. J. Appl. Ceram. Technol.*, vol. 15, no. 2, pp. 296–306, Mar. 2018, doi: 10.1111/ijac.12794.
- [29] Y. Zhang, S. Zha, and M. Liu, "Dual-Scale Porous Electrodes for Solid Oxide Fuel Cells from Polymer Foams," *Adv. Mater.*, vol. 17, no. 4, pp. 487–491, Feb. 2005, doi: 10.1002/adma.200400466.
- [30] X. Liu, X. Meng, D. Han, H. Wu, F. Zeng, and Z. Zhan, "Impregnated nickel anodes for reduced-temperature solid oxide fuel cells based on thin electrolytes of doped LaGaO₃," *J. Power Sources*, vol. 222, pp. 92–96, Jan. 2013, doi: 10.1016/J.JPOWSOUR.2012.08.019.
- [31] B. Tjaden, D. J. L. Brett, and P. R. Shearing, "Tortuosity in electrochemical devices: a review of calculation approaches," *Int. Mater. Rev.*, vol. 63, no. 2, pp. 47–67, Feb. 2018, doi: 10.1080/09506608.2016.1249995.
- [32] D. Cetin, S. Poizeau, J. Pietras, and S. Gopalan, "Phase stabilization of La₂NiO₄ in La_xCe_{1-x}O₂:La₂NiO₄ composites for solid oxide fuel cell applications," *Solid State Ionics*, vol. 307, pp. 14–20, Sep. 2017, doi: 10.1016/J.SSI.2017.05.001.
- [33] D. Cetin, S. Poizeau, J. Pietras, and S. Gopalan, "Decomposition of La₂NiO₄ in Sm_{0.2}Ce_{0.8}O₂-La₂NiO₄ composites for solid oxide fuel cell applications," *Solid State Ionics*, vol. 300, pp. 91–96, Feb. 2017, doi: 10.1016/J.SSI.2016.11.030.

- [34] D. Cetin, S. Poizeau, and S. Gopalan, "Phase Stability and Electrochemical Characterization of Solid Oxide Fuel Cell Cathodes Containing K₂NiF₄ Structured Oxides," *Meet. Abstr.*, vol. MA2016-02, no. 39, pp. 2870–2870, Sep. 2016, Accessed: Jan. 07, 2019. [Online]. Available: <http://ma.ecsdl.org/content/MA2016-02/39/2870.short>.
- [35] Y. Yu, K. F. Ludwig, U. B. Pal, S. Gopalan, and S. N. Basu, "Electronic Structure Measurements of Heteroepitaxial Solid Oxide Fuel Cell Cathode Thin Films," *ECS Trans.*, vol. 64, no. 2, pp. 203–210, Aug. 2014, doi: 10.1149/06402.0203ecst.
- [36] J. N. Davis *et al.*, "Hard X-ray Fluorescence Measurements of Heteroepitaxial Solid Oxide Fuel Cell Cathode Materials," in *ECS Transactions*, May 2012, vol. 41, no. 11, pp. 19–24, doi: 10.1149/1.3687387.
- [37] K. Wang *et al.*, "A Review on solid oxide fuel cell models," *Int. J. Hydrogen Energy*, vol. 36, no. 12, pp. 7212–7228, 2011, doi: 10.1016/j.ijhydene.2011.03.051.
- [38] D. Marra, C. (Cesare) Pianese, P. Polverino, and M. Sorrentino, *Models for solid oxide fuel cell systems: exploitation of models hierarchy for industrial design of control and diagnosis strategies*. Springer, 2016.
- [39] N. Laosiripojana, W. Wiyaratn, W. Kiatkittipong, A. Arpornwichanop, A. Soottitantawat, and S. Assabumrungrat, "Reviews on solid oxide fuel cell technology," *Eng. J.*, vol. 13, no. 1, pp. 65–83, 2009, doi: 10.4186/ej.2009.13.1.65.
- [40] S. P. S. Badwal and K. Foger, "Solid oxide electrolyte fuel cell review," *Ceram. Int.*, vol. 22, no. 3, pp. 257–265, Jan. 1996, doi: 10.1016/0272-8842(95)00101-8.
- [41] L. Barelli, E. Barluzzi, and G. Bidini, "Diagnosis methodology and technique for solid oxide fuel cells: A review," *Int. J. Hydrogen Energy*, vol. 38, no. 12, pp. 5060–5074, 2013, doi: 10.1016/j.ijhydene.2013.02.024.
- [42] M. Bavarian, M. Soroush, I. G. Kevrekidis, and J. B. Benziger, "Mathematical Modeling, Steady-State and Dynamic Behavior, and Control of Fuel Cells: A Review [†]," *Ind. Eng. Chem. Res.*, vol. 49, no. 17, pp. 7922–7950, Sep. 2010, doi: 10.1021/ie100032c.
- [43] S. P. Jiang and S. H. Chan, "A review of anode materials development in solid oxide fuel cells," *J. Mater. Sci.*, vol. 39, no. 14, pp. 4405–4439, Jul. 2004, doi: 10.1023/B:JMSC.0000034135.52164.6b.
- [44] J. Molenda *et al.*, "Status report on high temperature fuel cells in Poland – Recent advances and achievements," *Int. J. Hydrogen Energy*, vol. 42, no. 7, pp. 4366–4403, Feb. 2017, doi: 10.1016/J.IJHYDENE.2016.12.087.

- [45] R. H. Pletcher, J. C. Tannehill, and D. A. Anderson, *Computational fluid mechanics and heat transfer*, Third. CRC Press, Taylor and Francis Group, 2012.
- [46] A. Pramuanjaroenkij, S. Kakaç, and X. Yang Zhou, "Mathematical analysis of planar solid oxide fuel cells," *Int. J. Hydrogen Energy*, vol. 33, no. 10, pp. 2547–2565, 2008, doi: 10.1016/j.ijhydene.2008.02.043.
- [47] W. Jeong and J. Seong, "Comparison of effects on technical variances of computational fluid dynamics (CFD) software based on finite element and finite volume methods," *Int. J. Mech. Sci.*, vol. 78, pp. 19–26, Jan. 2014, doi: 10.1016/J.IJMECSCI.2013.10.017.
- [48] T. Dey, P. C. Ghosh, D. Singdeo, M. Bose, and R. N. Basu, "Diagnosis of scale up issues associated with planar solid oxide fuel cells," *Int. J. Hydrogen Energy*, vol. 36, no. 16, pp. 9967–9976, 2011, doi: 10.1016/j.ijhydene.2011.05.052.
- [49] H. Liu, P. Li, and J. Van Lew, "CFD study on flow distribution uniformity in fuel distributors having multiple structural bifurcations of flow channels," *Int. J. Hydrogen Energy*, vol. 35, no. 17, pp. 9186–9198, 2010, doi: 10.1016/j.ijhydene.2010.06.043.
- [50] C. Zhao, C. Wang, T. Zhang, and J. Pu, "Flow Distribution Analysis in the SOFC Stack Using CFD Technique," in *ASME 2017 15th International Conference on Fuel Cell Science, Engineering and Technology*, Jun. 2017, p. V001T02A003, doi: 10.1115/FUELCELL2017-3177.
- [51] C. Zhao *et al.*, "Numerical simulation of flow distribution for external manifold design in solid oxide fuel cell stack," *Int. J. Hydrogen Energy*, vol. 42, no. 10, pp. 7003–7013, 2017, doi: 10.1016/j.ijhydene.2016.12.009.
- [52] S. Su *et al.*, "Flow distribution analyzing for the solid oxide fuel cell short stacks with rectangular and discrete cylindrical rib configurations," *Int. J. Hydrogen Energy*, vol. 40, no. 1, pp. 577–592, 2015, doi: 10.1016/j.ijhydene.2014.10.125.
- [53] W. Bi, J. Li, and Z. Lin, "Flow uniformity optimization for large size planar solid oxide fuel cells with U-type parallel channel designs," *J. Power Sources*, vol. 195, no. 10, pp. 3207–3214, May 2010, doi: 10.1016/J.JPOWSOUR.2009.11.127.
- [54] D. Chen, Q. Zeng, S. Su, W. Bi, and Z. Ren, "Geometric optimization of a 10-cell modular planar solid oxide fuel cell stack manifold," *Appl. Energy*, vol. 112, pp. 1100–1107, Dec. 2013, doi: 10.1016/J.APENERGY.2013.04.035.
- [55] K. Rashid, S. K. Dong, R. A. Khan, and S. H. Park, "Optimization of manifold design for 1 kW-class flat-tubular solid oxide fuel cell stack operating on reformed natural gas," *J. Power Sources*, vol. 327, pp. 638–652, Sep. 2016, doi: 10.1016/J.JPOWSOUR.2016.07.077.

- [56] W. J. Sembler and S. Kumar, "optimization of a single-cell solid-oxide fuel cell using computational fluid dynamics," *J. Fuel Cell Sci. Technol.*, vol. 8, no. 2, p. 021007, 2011, doi: 10.1115/1.4002616.
- [57] Y. Yang, G. Wang, H. Zhang, and W. Xia, "Comparison of heat and mass transfer between planar and MOLB-type SOFCs," *J. Power Sources*, vol. 177, no. 2, pp. 426–433, Mar. 2008, doi: 10.1016/J.JPOWSOUR.2007.11.025.
- [58] G. M. Goldin, H. Zhu, R. J. Kee, D. Bierschenk, and S. A. Barnett, "Multidimensional flow, thermal, and chemical behavior in solid-oxide fuel cell button cells," *J. Power Sources*, vol. 187, no. 1, pp. 123–135, Feb. 2009, doi: 10.1016/J.JPOWSOUR.2008.10.097.
- [59] Z. Qu *et al.*, "Three-dimensional computational fluid dynamics modeling of anode-supported planar SOFC," *Int. J. Hydrogen Energy*, vol. 36, no. 16, pp. 10209–10220, 2011, doi: 10.1016/j.ijhydene.2010.11.018.
- [60] C. Boigues-Muñoz, G. Santori, S. McPhail, and F. Polonara, "Thermochemical model and experimental validation of a tubular SOFC cell comprised in a 1 kWelstack designed for μ CHP applications," *Int. J. Hydrogen Energy*, vol. 39, no. 36, pp. 1–10, 2014, doi: 10.1016/j.ijhydene.2014.09.021.
- [61] Z. Zhang *et al.*, "Three-dimensional CFD modeling of transport phenomena in multi-channel anode-supported planar SOFCs," *Int. J. Heat Mass Transf.*, vol. 84, pp. 942–954, 2015, doi: 10.1016/j.ijheatmasstransfer.2015.01.097.
- [62] M. E. Saied, K. I. Ahmed, M. A. Ahmed, and M. M. N. M. G. El-sebaie, "Numerical Study of Solid Oxide Fuel Cell Performance with Helical and Serpentine Flow Field Designs," *Int. J. Control. Autom. Syst.*, vol. 4, no. 3, pp. 27–33, 2015.
- [63] S.-S. Wei, T.-H. Wang, and J.-S. Wu, "Numerical modeling of interconnect flow channel design and thermal stress analysis of a planar anode-supported solid oxide fuel cell stack," *Energy*, vol. 69, pp. 553–561, May 2014, doi: 10.1016/j.energy.2014.03.052.
- [64] S. K. Dong, W. N. Jung, K. Rashid, and A. Kashimoto, "Design and numerical analysis of a planar anode-supported SOFC stack," *Renew. Energy*, vol. 94, pp. 637–650, 2016, doi: 10.1016/j.renene.2016.03.098.
- [65] B. Ghorbani and K. Vijayaraghavan, "3D and simplified pseudo-2D modeling of single cell of a high temperature solid oxide fuel cell to be used for online control strategies," *Int. J. Hydrogen Energy*, vol. 43, no. 20, pp. 9733–9748, May 2018, doi: 10.1016/J.IJHYDENE.2018.03.211.
- [66] G. J. Nelson, "An analytical approach for solid oxide cell electrode geometric design," *J. Power Sources*, vol. 300, pp. 365–375, Dec. 2015, doi: 10.1016/J.JPOWSOUR.2015.09.085.

- [67] W. J. Sembler and S. Kumar, "Modification of results from computational-fluid-dynamics simulations of single-cell solid-oxide fuel cells to estimate multi-cell stack performance," in *ASME 2010 8th International Fuel Cell Science, Engineering and Technology Conference: Volume 2*, 2010, pp. 15–24, doi: 10.1115/FuelCell2010-33014.
- [68] S. Murthy and A. G. Fedorov, "Radiation heat transfer analysis of the monolith type solid oxide fuel cell," *J. Power Sources*, vol. 124, no. 2, pp. 453–458, Nov. 2003, doi: 10.1016/S0378-7753(03)00732-8.
- [69] A. Sciacovelli and V. Verda, "Optimal Design of a Solid Oxide Fuel Cell for Hybrid Vehicle Application," in *4th European Automotive Simulation Conference*, 2009, [Online]. Available: <https://www.ansys.com/-/media/ansys/corporate/resourcelibrary/conference-paper/optimal-solid-oxide.pdf>.
- [70] S. Campanari and P. Iora, "Definition and sensitivity analysis of a finite volume SOFC model for a tubular cell geometry," *J. Power Sources*, vol. 132, no. 1–2, pp. 113–126, May 2004, doi: 10.1016/J.JPOWSOUR.2004.01.043.
- [71] S. L. Puthran, U. O. Koylu, S. Hosder, and F. Dogan, "Three-Dimensional CFD Modeling of Tubular Solid Oxide Fuel Cells With Different Fuels," in *ASME 2011 9th International Conference on Fuel Cell Science, Engineering and Technology*, Jan. 2011, pp. 465–473, doi: 10.1115/FuelCell2011-54761.
- [72] G. Goldin *et al.*, "Coupling complex reformer chemical kinetics with three-dimensional computational fluid dynamics," in *ECS Transactions*, Sep. 2009, vol. 25, no. 2, pp. 1253–1262, doi: 10.1149/1.3205654.
- [73] M. S. Thesis and E. D. Dimitriou, "Analysis and Simulation of an Anode Supported Solid Oxide Fuel Cell Single Channel for Operation with Biosyngas and Methane by," no. December, 2011.
- [74] K. Rashid, S. K. Dong, and M. T. Mehran, "Numerical investigations to determine the optimal operating conditions for 1 kW-class flat-tubular solid oxide fuel cell stack," *Energy*, vol. 141, pp. 673–691, Dec. 2017, doi: 10.1016/J.ENERGY.2017.09.082.
- [75] S. Hosseini, K. Ahmed, and M. O. Tadé, "CFD model of a methane fuelled single cell SOFC stack for analysing the combined effects of macro/micro structural parameters," *J. Power Sources*, vol. 234, pp. 180–196, Jul. 2013, doi: 10.1016/J.JPOWSOUR.2012.12.123.
- [76] J. J. Ramírez-Minguela, J. M. Mendoza-Miranda, V. D. Muñoz-Carpio, V. H. Rangel-Hernández, V. Pérez-García, and J. L. Rodríguez-Muñoz, "Internal reforming of methane in a mono-block-layer build solid oxide fuel cell with an embedding porous pipe: Numerical analysis," *Energy Convers. Manag.*, vol. 79, pp. 461–469, Mar. 2014, doi: 10.1016/J.ENCONMAN.2013.12.061.

- [77] M. Dillig, T. Plankenbühler, and J. Karl, "Thermal effects of planar high temperature heat pipes in solid oxide cell stacks operated with internal methane reforming," *J. Power Sources*, vol. 373, pp. 139–149, Jan. 2018, doi: 10.1016/J.JPOWSOUR.2017.11.007.
- [78] M. Peksen, "3D transient multiphysics modelling of a complete high temperature fuel cell system using coupled CFD and FEM," *Int. J. Hydrogen Energy*, vol. 39, no. 10, pp. 5137–5147, 2014, doi: 10.1016/j.ijhydene.2014.01.063.
- [79] I. Zinovik and D. Poulikakos, "Modeling the temperature field in the reforming anode of a button-shaped solid oxide fuel cell," *Electrochim. Acta*, vol. 54, no. 26, pp. 6234–6243, Nov. 2009, doi: 10.1016/J.ELECTACTA.2009.06.001.
- [80] K. Ahmed and K. Foger, "Kinetics of internal steam reforming of methane on Ni/YSZ-based anodes for solid oxide fuel cells," *Catal. Today*, vol. 63, no. 2–4, pp. 479–487, Dec. 2000, doi: 10.1016/S0920-5861(00)00494-6.
- [81] E. De La Pena-Cortes, F. Elizalde-Blancas, A. Hernandez-Guerrero, A. Gallegos-Munoz, and J. M. Belman-Flores, "Numerical Analysis of the Internal Fuel Processing in Solid Oxide Fuel Cells," in *Volume 6B: Energy*, Nov. 2013, p. V06BT07A022, doi: 10.1115/IMECE2013-65273.
- [82] K. J. Kattke and R. J. Braun, "Characterization of a novel, highly integrated tubular solid oxide fuel cell system using high-fidelity simulation tools," *J. Power Sources*, vol. 196, no. 15, pp. 6347–6355, Aug. 2011, doi: 10.1016/J.JPOWSOUR.2011.03.030.
- [83] H. Moon, D. W. Kang, H. G. Park, and S. H. Hyun, "Stress and camber analysis of anode-supported electrolytes by tape-casting and co-firing techniques," *Int. J. Hydrogen Energy*, vol. 36, no. 17, pp. 10991–10997, 2011, doi: 10.1016/j.ijhydene.2011.05.097.
- [84] J. Malzbender, "Curvature and stresses for bi-layer functional ceramic materials," *J. Eur. Ceram. Soc.*, vol. 30, no. 16, pp. 3407–3413, Dec. 2010, doi: 10.1016/J.JEURCERAMSOC.2010.07.036.
- [85] J. Wei and J. Malzbender, "Steady state creep of Ni-8YSZ substrates for application in solid oxide fuel and electrolysis cells," *J. Power Sources*, vol. 360, pp. 1–10, Aug. 2017, doi: 10.1016/J.JPOWSOUR.2017.05.113.
- [86] C. Wang, T. Zhang, C. Zhao, and J. Pu, "Numerical Study of Thermal Stresses in a Planar Solid Oxide Fuel Cell Stack," in *ASME 2017 15th International Conference on Fuel Cell Science, Engineering and Technology*, Jun. 2017, p. V001T02A002, doi: 10.1115/FUELCCELL2017-3176.
- [87] K. S. Weil and B. J. Koeppel, "Comparative finite element analysis of the stress–strain states in three different bonded solid oxide fuel cell seal designs," *J. Power Sources*, vol. 180, no. 1, pp. 343–353, May 2008, doi: 10.1016/J.JPOWSOUR.2008.01.093.

- [88] K. S. Weil and B. J. Koeppel, "Thermal stress analysis of the planar SOFC bonded compliant seal design," *Int. J. Hydrogen Energy*, vol. 33, no. 14, pp. 3976–3990, 2008, doi: 10.1016/j.ijhydene.2007.11.008.
- [89] T. L. Jiang and M. H. Chen, "Thermal-stress analyses of an operating planar solid oxide fuel cell with the bonded compliant seal design," *Int. J. Hydrogen Energy*, vol. 34, no. 19, pp. 8223–8234, 2009, doi: 10.1016/j.ijhydene.2009.07.089.
- [90] M. Peksen, A. Al-Masri, L. Blum, and D. Stolten, "3D transient thermomechanical behaviour of a full scale SOFC short stack," *Int. J. Hydrogen Energy*, vol. 38, no. 10, pp. 4099–4107, Apr. 2013, doi: 10.1016/J.IJHYDENE.2013.01.072.
- [91] M. Fakouri Hasanabadi, M. A. Faghihi-Sani, A. H. Kokabi, and J. Malzbender, "The analysis of torsional shear strength test of sealants for solid oxide fuel cells," *Ceram. Int.*, vol. 43, no. 15, pp. 12546–12550, Oct. 2017, doi: 10.1016/J.CERAMINT.2017.06.128.
- [92] D. N. Boccaccini *et al.*, "Determination of the bonding strength in solid oxide fuel cells' interfaces by Schwickerath crack initiation test," *J. Eur. Ceram. Soc.*, vol. 37, no. 11, pp. 3565–3578, Sep. 2017, doi: 10.1016/J.JEURCERAMSOC.2017.04.018.
- [93] T. Dey, D. Singdeo, J. Deshpande, and P. C. Ghosh, "Structural Analysis of Solid Oxide Fuel Cell under Externally Applied Compressive Pressure," *Energy Procedia*, vol. 54, pp. 789–795, Jan. 2014, doi: 10.1016/J.EGYPRO.2014.07.322.
- [94] N. K. Karri, B. J. Koeppel, B. N. Nguyen, and K. Lai, "Structural Reliability of Cathode Contact Materials in Planar SOFCs," *ECS Trans.*, vol. 78, no. 1, pp. 1701–1712, May 2017, doi: 10.1149/07801.1701ecst.
- [95] M. Peksen, "A coupled 3D thermofluid–thermomechanical analysis of a planar type production scale SOFC stack," *Int. J. Hydrogen Energy*, vol. 36, no. 18, pp. 11914–11928, Sep. 2011, doi: 10.1016/J.IJHYDENE.2011.06.045.
- [96] M. Peksen, "3D thermomechanical behaviour of solid oxide fuel cells operating in different environments," *Int. J. Hydrogen Energy*, vol. 38, no. 30, pp. 13408–13418, 2013, doi: 10.1016/j.ijhydene.2013.07.112.
- [97] M. Saied, K. Ahmed, M. Ahmed, M. Nemat-Alla, and M. El-Sebaie, "Investigations of solid oxide fuel cells with functionally graded electrodes for high performance and safe thermal stress," *Int. J. Hydrogen Energy*, vol. 42, no. 24, pp. 15887–15902, 2017, doi: 10.1016/j.ijhydene.2017.05.071.
- [98] M. Nemat-Alla, "Reduction of thermal stresses by developing two-dimensional functionally graded materials," *Int. J. Solids Struct.*, vol. 40, no. 26, pp. 7339–7356, Dec. 2003, doi: 10.1016/J.IJSOLSTR.2003.08.017.

- [99] Y. J. Kim and M. C. Lee, "Numerical investigation of flow/heat transfer and structural stress in a planar solid oxide fuel cell," *Int. J. Hydrogen Energy*, vol. 42, no. 29, pp. 18504–18513, 2017, doi: 10.1016/j.ijhydene.2017.04.140.
- [100] P. Pianko-Oprych, T. Zinko, and Z. Jaworski, "Simulation of thermal stresses for new designs of microtubular Solid Oxide Fuel Cell stack," *Int. J. Hydrogen Energy*, vol. 40, no. 42, pp. 14584–14595, 2015, doi: 10.1016/j.ijhydene.2015.05.164.
- [101] T. Ackmann, L. G. J. de Haart, W. Lehnert, and D. Stolten, "Modeling of mass and heat transport in planar substrate type SOFCs," *J. Electrochem. Soc.*, vol. 150, no. 6, p. A783, 2003, doi: 10.1149/1.1574029.
- [102] A. Pramuanjaroenkij, S. Kakaç, and X. Yang Zhou, "Mathematical analysis of planar solid oxide fuel cells," *Int. J. Hydrogen Energy*, vol. 33, no. 10, pp. 2547–2565, 2008, doi: 10.1016/j.ijhydene.2008.02.043.
- [103] D. H. Jeon, "A comprehensive CFD model of anode-supported solid oxide fuel cells," *Electrochim. Acta*, vol. 54, no. 10, pp. 2727–2736, 2009, doi: 10.1016/j.electacta.2008.11.048.
- [104] D. F. Cheddie and N. D. H. Munroe, "A dynamic 1D model of a solid oxide fuel cell for real time simulation," *J. Power Sources*, vol. 171, no. 2, pp. 634–643, 2007, doi: 10.1016/j.jpowsour.2007.06.170.
- [105] P. Iora, P. Aguiar, C. S. Adjiman, and N. P. Brandon, "Comparison of two IT DIR-SOFC models: Impact of variable thermodynamic, physical, and flow properties. Steady-state and dynamic analysis," *Chem. Eng. Sci.*, vol. 60, no. 11, pp. 2963–2975, 2005, doi: 10.1016/j.ces.2005.01.007.
- [106] Y. KANG, J. LI, G. CAO, H. TU, J. LI, and J. YANG, "One-dimensional dynamic modeling and simulation of a planar direct internal reforming solid oxide fuel cell," *Chinese J. Chem. Eng.*, vol. 17, no. 2, pp. 304–317, Apr. 2009, doi: 10.1016/S1004-9541(08)60209-8.
- [107] S. . Chan, K. . Khor, and Z. . Xia, "A complete polarization model of a solid oxide fuel cell and its sensitivity to the change of cell component thickness," *J. Power Sources*, vol. 93, no. 1, pp. 130–140, 2001, doi: 10.1016/S0378-7753(00)00556-5.
- [108] K. Nikooyeh, A. A. Jeje, and J. M. Hill, "3D modeling of anode-supported planar SOFC with internal reforming of methane," *J. Power Sources*, vol. 171, no. 2, pp. 601–609, 2007, doi: 10.1016/j.jpowsour.2007.07.003.
- [109] H. Yakabe, M. Hishinuma, M. Uratani, Y. Matsuzaki, and I. Yasuda, "Evaluation and modeling of performance of anode-supported solid oxide fuel cell," *J. Power Sources*, vol. 86, no. 1, pp. 423–431, 2000, doi: 10.1016/S0378-7753(99)00444-9.

- [110] H. Yakabe, T. Ogiwara, M. Hishinuma, and I. Yasuda, "3-D model calculation for planar SOFC," *J. Power Sources*, vol. 102, no. 1, pp. 144–154, 2001, doi: 10.1016/S0378-7753(01)00792-3.
- [111] H. Mahcene, H. Ben Moussa, H. Bouguettaia, D. Bechki, S. Babay, and M. S. Meftah, "Study of species, temperature distributions and the solid oxide fuel cells performance in a 2-D model," *Int. J. Hydrogen Energy*, vol. 36, no. 6, pp. 4244–4252, 2011, doi: 10.1016/j.ijhydene.2010.07.075.
- [112] P. Costamagna, L. Magistri, and A. F. Massardo, "Design and part-load performance of a hybrid system based on a solid oxide fuel cell reactor and a micro gas turbine," *J. Power Sources*, vol. 96, no. 2, pp. 352–368, Jun. 2001, doi: 10.1016/S0378-7753(00)00668-6.
- [113] X.-J. Wu, X.-J. Zhu, G.-Y. Cao, H.-Y. Tu, and W.-Q. Hu, "A Hybrid Experimental Model of a Solid Oxide Fuel Cell Stack," *J. Fuel Cell Sci. Technol.*, vol. 6, no. 1, p. 011013, Feb. 2009, doi: 10.1115/1.2971125.
- [114] F. Standaert, K. Hemmes, and N. Woudstra, "Analytical fuel cell modeling," *J. Power Sources*, vol. 63, no. 2, pp. 221–234, Dec. 1996, doi: 10.1016/S0378-7753(96)02479-2.
- [115] R. Bove, P. Lunghi, and N. M. Sammes, "SOFC mathematic model for systems simulations—Part 2: definition of an analytical model," *Int. J. Hydrogen Energy*, vol. 30, no. 2, pp. 189–200, Feb. 2005, doi: 10.1016/J.IJHYDENE.2004.04.018.
- [116] M. YOKOO, "Simulation analysis of a system combining solid oxide and polymer electrolyte fuel cells," *J. Power Sources*, vol. 137, no. 2, pp. 206–215, Oct. 2004, doi: 10.1016/j.jpowsour.2004.06.007.
- [117] P.-W. Li and K. Suzuki, "Numerical modeling and performance study of a tubular SOFC," *J. Electrochem. Soc.*, vol. 151, no. 4, p. A548, Apr. 2004, doi: 10.1149/1.1647569.
- [118] R. Bove and N. Sammes, "The effect of current collectors configuration on the performance of a tubular SOFC," *Meet. Abstr.*, vol. MA2005-01, no. 30, pp. 1224–1224, Feb. 2006, Accessed: Jan. 12, 2018. [Online]. Available: <http://ma.ecsdl.org/content/MA2005-01/30/1224.short>.
- [119] K. J. Kattke, R. J. Braun, A. M. Colclasure, and G. Goldin, "High-fidelity stack and system modeling for tubular solid oxide fuel cell system design and thermal management," *J. Power Sources*, vol. 196, no. 8, pp. 3790–3802, Apr. 2011, doi: 10.1016/J.JPOWSOUR.2010.12.070.
- [120] E. A. El-Hay, M. A. El-Hameed, and A. A. El-Fergany, "Steady-state and dynamic models of solid oxide fuel cells based on Satin Bowerbird Optimizer," *Int. J. Hydrogen Energy*, vol. 43, no. 31, pp. 14751–14761, Aug. 2018, doi: 10.1016/J.IJHYDENE.2018.06.032.

- [121] Y. Bae, S. Lee, K. J. Yoon, J. H. Lee, and J. Hong, "Three-dimensional dynamic modeling and transport analysis of solid oxide fuel cells under electrical load change," *Energy Convers. Manag.*, vol. 165, no. March, pp. 405–418, 2018, doi: 10.1016/j.enconman.2018.03.064.
- [122] S. Choudhury, P. Bhowmik, and P. K. Rout, "Seeker optimization approach to dynamic PI based virtual impedance drooping for economic load sharing between PV and SOFC in an islanded microgrid," *Sustain. Cities Soc.*, vol. 37, pp. 550–562, Feb. 2018, doi: 10.1016/J.SCS.2017.11.013.
- [123] M. Taghizadeh, M. Hoseintabar, and J. Faiz, "Frequency control of isolated WT/PV/SOFC/UC network with new control strategy for improving SOFC dynamic response," *Int. Trans. Electr. Energy Syst.*, vol. 25, no. 9, pp. 1748–1770, Sep. 2015, doi: 10.1002/etep.1925.
- [124] J. Kupecki, K. Motylinski, and J. Milewski, "Dynamic analysis of direct internal reforming in a SOFC stack with electrolyte-supported cells using a quasi-1D model," *Appl. Energy*, vol. 227, pp. 198–205, Oct. 2018, doi: 10.1016/J.APENERGY.2017.07.122.
- [125] X. Fang and Z. Lin, "Numerical study on the mechanical stress and mechanical failure of planar solid oxide fuel cell," *Appl. Energy*, vol. 229, pp. 63–68, Nov. 2018, doi: 10.1016/J.APENERGY.2018.07.077.
- [126] M. Gallo, D. Marra, M. Sorrentino, C. Pianese, and S. F. Au, "A versatile computational tool for model-based design, control and diagnosis of a generic Solid Oxide Fuel Cell Integrated Stack Module," *Energy Convers. Manag.*, vol. 171, pp. 1514–1528, Sep. 2018, doi: 10.1016/J.ENCONMAN.2018.06.062.
- [127] B. S. Gerwe, K. Mizuno, O. Sekizawa, K. Nitta, K. Amezawa, and S. B. Adler, "Frequency-Resolved Evaluation of Electrode Oxidation State in La_{0.6}Sr_{0.4}CoO₃ Thin Films with Operando XAS," *Meet. Abstr.*, vol. MA2018-02, no. 48, pp. 1657–1657, Jul. 2018, Accessed: Sep. 17, 2018. [Online]. Available: <http://ma.ecsdl.org/content/MA2018-02/48/1657.short>.
- [128] B. Stoeckl, V. Subotić, M. Preininger, H. Schroettner, and C. Hochenauer, "SOFC operation with carbon oxides: Experimental analysis of performance and degradation," *Electrochim. Acta*, vol. 275, pp. 256–264, Jun. 2018, doi: 10.1016/J.ELECTACTA.2018.04.036.
- [129] C. Ni, M. Cassidy, and J. T. S. Irvine, "Image analysis of the porous yttria-stabilized zirconia (YSZ) structure for a lanthanum ferrite-impregnated solid oxide fuel cell (SOFC) electrode," *J. Eur. Ceram. Soc.*, vol. 38, no. 16, pp. 5463–5470, Dec. 2018, doi: 10.1016/J.JEURCERAMSOC.2018.08.026.
- [130] M. Le Bars and M. G. Worster, "Interfacial conditions between a pure fluid and a porous medium: implications for binary alloy solidification," *J. Fluid Mech.*, vol. 550, no. 1, p. 149, Feb. 2006, doi: 10.1017/S0022112005007998.

- [131] W. G. Bessler, S. Gewies, and M. Vogler, "A new framework for physically based modeling of solid oxide fuel cells," *Electrochim. Acta*, vol. 53, no. 4, pp. 1782–1800, Dec. 2007, doi: 10.1016/j.electacta.2007.08.030.
- [132] M. Boder and R. Dittmeyer, "Catalytic modification of conventional SOFC anodes with a view to reducing their activity for direct internal reforming of natural gas," *J. Power Sources*, vol. 155, no. 1, pp. 13–22, Apr. 2006, doi: 10.1016/j.jpowsour.2004.11.075.
- [133] D. L. Damm and A. G. Fedorov, "Local thermal non-equilibrium effects in porous electrodes of the hydrogen-fueled SOFC," *J. Power Sources*, vol. 159, no. 2, pp. 1153–1157, Sep. 2006, doi: 10.1016/j.jpowsour.2005.12.008.
- [134] M. Tatko, M. Mosiałek, A. Kędra, E. Bielańska, M. Ruggiero-Mikołajczyk, and P. Nowak, "Thermal shock resistant composite cathode material $\text{Sm}_{0.5}\text{Sr}_{0.5}\text{CoO}_{3-\delta}\text{--La}_{0.6}\text{Sr}_{0.4}\text{FeO}_{3-\delta}$ for solid oxide fuel cells," *J. Solid State Electrochem.*, vol. 20, no. 1, pp. 143–151, Jan. 2016, doi: 10.1007/s10008-015-3010-9.
- [135] A. Mielewczyk-Gryn, S. Wachowski, K. I. Lilova, X. Guo, M. Gazda, and A. Navrotsky, "Influence of antimony substitution on spontaneous strain and thermodynamic stability of lanthanum orthoniobate," *Ceram. Int.*, vol. 41, no. 2, pp. 2128–2133, Mar. 2015, doi: 10.1016/j.ceramint.2014.10.010.
- [136] M. Tatko, M. Mosiałek, M. Dudek, P. Nowak, A. Kędra, and E. Bielańska, "Composite cathode materials $\text{Sm}_{0.5}\text{Sr}_{0.5}\text{CoO}_3\text{--La}_{0.6}\text{Sr}_{0.4}\text{FeO}_3$ for solid oxide fuel cells," *Solid State Ionics*, vol. 271, pp. 103–108, Mar. 2015, doi: 10.1016/j.ssi.2014.10.011.
- [137] L. dos Santos-Gómez, J. M. Porras-Vázquez, E. R. Losilla, and D. Marrero-López, "Improving the efficiency of layered perovskite cathodes by microstructural optimization," *J. Mater. Chem. A*, vol. 5, no. 17, pp. 7896–7904, May 2017, doi: 10.1039/C6TA10946B.
- [138] P. A. Connor *et al.*, "Tailoring SOFC Electrode Microstructures for Improved Performance," *Adv. Energy Mater.*, vol. 8, no. 23, p. 1800120, Aug. 2018, doi: 10.1002/aenm.201800120.
- [139] I. Gholaminezhad, K. Jafarpur, M. H. Paydar, and G. Karimi, "Multi-scale multi-objective optimization and uncertainty analysis of methane-fed solid oxide fuel cells using Monte Carlo simulations," *Energy Convers. Manag.*, vol. 153, pp. 175–187, Dec. 2017, doi: 10.1016/J.ENCONMAN.2017.10.011.
- [140] S. H. Chan and Z. T. Xia, "Anode Micro Model of Solid Oxide Fuel Cell," *J. Electrochem. Soc.*, vol. 148, no. 4, p. A388, Apr. 2001, doi: 10.1149/1.1357174.
- [141] J. Deseure, Y. Bultel, L. Dessemond, and E. Siebert, "Theoretical optimisation of a SOFC composite cathode," *Electrochim. Acta*, vol. 50, no. 10, pp. 2037–2046, Mar. 2005, doi: 10.1016/j.electacta.2004.09.012.

- [142] D. H. Jeon, J. H. Nam, and C.-J. Kim, "Microstructural Optimization of Anode-Supported Solid Oxide Fuel Cells by a Comprehensive Microscale Model," *J. Electrochem. Soc.*, vol. 153, no. 2, p. A406, 2006, doi: 10.1149/1.2139954.
- [143] J. H. Nam and D. H. Jeon, "A comprehensive micro-scale model for transport and reaction in intermediate temperature solid oxide fuel cells," *Electrochim. Acta*, vol. 51, no. 17, pp. 3446–3460, Apr. 2006, doi: 10.1016/j.electacta.2005.09.041.
- [144] J. Shi and X. Xue, "CFD analysis of a symmetrical planar SOFC with heterogeneous electrode properties," *Electrochim. Acta*, vol. 55, no. 18, pp. 5263–5273, Jul. 2010, doi: 10.1016/j.electacta.2010.04.060.
- [145] D. Farina, Y. Jiang, O. Skipa, O. Dossel, C. Kaltwasser, and W. R. Bauer, "The use of the simulation results as a priori information to solve the inverse problem of electrocardiography for a patient," in *Computers in Cardiology, 2005*, 2005, pp. 571–574, doi: 10.1109/CIC.2005.1588165.
- [146] A. Fichtner, A. Zunino, and L. Gebraad, "Hamiltonian Monte Carlo solution of tomographic inverse problems," *Geophys. J. Int.*, vol. 216, no. 2, pp. 1344–1363, Feb. 2019, doi: 10.1093/gji/ggy496.
- [147] J. Málek, B. Růžek, and P. Kolář, "Isometric method: Efficient tool for solving non-linear inverse problems," *Stud. Geophys. Geod.*, vol. 51, no. 4, pp. 469–490, Oct. 2007, doi: 10.1007/s11200-007-0028-1.
- [148] R. Sikora, A. Kaminska, and J. Sikora, "The inverse problem solution for infinite regions using the impedance tomography technique," *IEEE Trans. Magn.*, vol. 32, no. 3, pp. 1294–1297, May 1996, doi: 10.1109/20.497482.
- [149] A. Ritter, R. Muñoz-Carpena, C. M. Regalado, M. Vanclooster, and S. Lambot, "Analysis of alternative measurement strategies for the inverse optimization of the hydraulic properties of a volcanic soil," *J. Hydrol.*, vol. 295, no. 1–4, pp. 124–139, Aug. 2004, doi: 10.1016/J.JHYDROL.2004.03.005.
- [150] W. W.-G. Yeh, "Review of Parameter Identification Procedures in Groundwater Hydrology: The Inverse Problem," *Water Resour. Res.*, vol. 22, no. 2, pp. 95–108, Feb. 1986, doi: 10.1029/WR022i002p00095.
- [151] K. C. Abbaspour, C. A. Johnson, and M. T. van Genuchten, "Estimating Uncertain Flow and Transport Parameters Using a Sequential Uncertainty Fitting Procedure," *Vadose Zo. J.*, vol. 3, no. 4, p. 1340, Nov. 2004, doi: 10.2136/vzj2004.1340.
- [152] P. Sarmah, T. K. Gogoi, and R. Das, "Estimation of operating parameters of a SOFC integrated combined power cycle using differential evolution based inverse method," *Appl. Therm. Eng.*, vol. 119, pp. 98–107, Jun. 2017, doi: 10.1016/J.APPLTHERMALENG.2017.03.060.

- [153] J. Shi and X. Xue, "Inverse approach to quantify multi-physicochemical properties of porous electrodes for solid oxide fuel cells," *Electrochim. Acta*, vol. 56, no. 24, pp. 8718–8726, Oct. 2011, doi: 10.1016/J.ELECTACTA.2011.07.073.
- [154] T. K. Gogoi and R. Das, "Inverse analysis of an internal reforming solid oxide fuel cell system using simplex search method," *Appl. Math. Model.*, vol. 37, no. 10–11, pp. 6994–7015, Jun. 2013, doi: 10.1016/J.APM.2013.02.046.
- [155] C. Comminges, Q. X. Fu, M. Zahid, N. Y. Steiner, and O. Bucheli, "Monitoring the degradation of a solid oxide fuel cell stack during 10,000 h via electrochemical impedance spectroscopy," *Electrochim. Acta*, vol. 59, pp. 367–375, 2012, doi: 10.1016/j.electacta.2011.10.080.
- [156] J. A. Schuler, Z. Wullemmin, A. Hessler-Wyser, C. Comminges, N. Y. Steiner, and J. Van Herle, "Cr-poisoning in (La,Sr)(Co,Fe)O₃ cathodes after 10,000 h SOFC stack testing," *J. Power Sources*, vol. 211, pp. 177–183, Aug. 2012, doi: 10.1016/j.jpowsour.2012.03.045.
- [157] A. El-amiri, A. Saifi, A. Elhassnaoui, A. Obbadi, Y. Errami, and S. Sahnoun, "Control of solid oxide fuel cells damage using infrared thermography," *Int. J. Hydrogen Energy*, vol. 45, no. 20, pp. 11695–11703, Apr. 2020, doi: 10.1016/j.ijhydene.2018.04.222.
- [158] I. Tikiz, I. Taymaz, and H. Pehlivan, "CFD modelling and experimental validation of cell performance in a 3-D planar SOFC," *Int. J. Hydrogen Energy*, vol. 44, no. 29, pp. 15441–15455, Jun. 2019, doi: 10.1016/j.ijhydene.2019.04.152.
- [159] J. Pan, J. Yang, D. Yan, J. Pu, B. Chi, and J. Li, "Effect of thermal cycling on durability of a solid oxide fuel cell stack with external manifold structure," *Int. J. Hydrogen Energy*, vol. 45, no. 35, pp. 17927–17934, Jul. 2020, doi: 10.1016/j.ijhydene.2020.04.260.
- [160] B. Ghorbani and K. Vijayaraghavan, "A review study on software-based modeling of hydrogen-fueled solid oxide fuel cells," *International Journal of Hydrogen Energy*, vol. 44, no. 26. Elsevier Ltd, pp. 13700–13727, May 21, 2019, doi: 10.1016/j.ijhydene.2019.03.217.
- [161] M. Mozdzierz, M. Chalusiak, S. Kimijima, J. S. Szmyd, and G. Brus, "An afterburner-powered methane/steam reformer for a solid oxide fuel cells application," *Heat Mass Transf. und Stoffuebertragung*, vol. 54, no. 8, pp. 2331–2341, Aug. 2018, doi: 10.1007/s00231-018-2331-5.
- [162] J. Kupecki, K. Motylinski, A. Zurawska, M. Kosiorek, and L. Ajdys, "Numerical analysis of an SOFC stack under loss of oxidant related fault conditions using a dynamic non-adiabatic model," *Int. J. Hydrogen Energy*, vol. 44, no. 38, pp. 21148–21161, Aug. 2019, doi: 10.1016/j.ijhydene.2019.04.029.

- [163] L. Bernadet, C. Moncasi, M. Torrell, and A. Tarancón, "High-performing electrolyte-supported symmetrical solid oxide electrolysis cells operating under steam electrolysis and co-electrolysis modes," *Int. J. Hydrogen Energy*, vol. 45, no. 28, pp. 14208–14217, May 2020, doi: 10.1016/j.ijhydene.2020.03.144.
- [164] M. Hubert, J. Laurencin, P. Cloetens, B. Morel, D. Montinaro, and F. Lefebvre-Joud, "Impact of Nickel agglomeration on Solid Oxide Cell operated in fuel cell and electrolysis modes," *J. Power Sources*, vol. 397, pp. 240–251, Sep. 2018, doi: 10.1016/j.jpowsour.2018.06.097.
- [165] C. Schluckner, V. Subotić, S. Preißl, and C. Hochenauer, "Numerical analysis of flow configurations and electrical contact positions in SOFC single cells and their impact on local effects," *Int. J. Hydrogen Energy*, vol. 44, no. 3, pp. 1877–1895, Jan. 2019, doi: 10.1016/j.ijhydene.2018.11.132.
- [166] Q. Fang, L. Blum, R. Peters, M. Peksen, P. Batfalsky, and D. Stolten, "SOFC stack performance under high fuel utilization," *Int. J. Hydrogen Energy*, vol. 40, no. 2, pp. 1128–1136, Jan. 2015, doi: 10.1016/j.ijhydene.2014.11.094.
- [167] R. Gaynor, F. Mueller, F. Jabbari, and J. Brouwer, "On control concepts to prevent fuel starvation in solid oxide fuel cells," *J. Power Sources*, vol. 180, no. 1, pp. 330–342, May 2008, doi: 10.1016/j.jpowsour.2008.01.078.
- [168] K. Takino *et al.*, "Simulation of SOFC performance using a modified exchange current density for pre-reformed methane-based fuels," *Int. J. Hydrogen Energy*, vol. 45, no. 11, pp. 6912–6925, Feb. 2020, doi: 10.1016/j.ijhydene.2019.12.089.
- [169] R. R. Mosbaek, "Solid Oxide Fuel Cell Stack Diagnostics," Technical University of Denmark, 2014.
- [170] T. Allag and T. Das, "Robust control of solid oxide fuel cell ultracapacitor hybrid system," *IEEE Trans. Control Syst. Technol.*, vol. 20, no. 1, pp. 1–10, Jan. 2012, doi: 10.1109/TCST.2010.2098478.
- [171] Q. Fang, L. Blum, R. Peters, M. Peksen, P. Batfalsky, and D. Stolten, "SOFC stack performance under high fuel utilization," *Int. J. Hydrogen Energy*, vol. 40, no. 2, pp. 1128–1136, Jan. 2015, doi: 10.1016/J.IJHYDENE.2014.11.094.
- [172] P. Pianko-Oprych, T. Zinko, and Z. Jaworski, "CFD modelling of hydrogen starvation conditions in a planar Solid Oxide Fuel Cell," *Polish J. Chem. Technol.*, vol. 19, no. 2, pp. 16–25, 2017, doi: 10.1515/pjct-2017-0022.
- [173] A. Faes *et al.*, "A Review of RedOx Cycling of Solid Oxide Fuel Cells Anode," *Membranes (Basel)*, vol. 2, no. 3, pp. 585–664, Aug. 2012, doi: 10.3390/membranes2030585.
- [174] K. Patan, *Artificial Neural Networks for the Modelling and Fault Diagnosis of Technical Processes*. Springer Berlin Heidelberg, 2008.

- [175] C. L. Moreira and J. A. Peças Lopes, "MicroGrids dynamic security assessment," *2007 Int. Conf. Clean Electr. Power, ICCEP '07*, pp. 26–32, 2007, doi: 10.1109/ICCEP.2007.384181.
- [176] E. B. Sydney, E. R. Duarte, W. J. Martinez Burgos, J. C. de Carvalho, C. Larroche, and C. R. Soccol, "Development of short chain fatty acid-based artificial neuron network tools applied to biohydrogen production," *Int. J. Hydrogen Energy*, vol. 45, no. 8, pp. 5175–5181, Feb. 2020, doi: 10.1016/j.ijhydene.2019.10.128.
- [177] T. Akter and S. Desai, "Developing a predictive model for nanoimprint lithography using artificial neural networks," *Mater. Des.*, vol. 160, pp. 836–848, Dec. 2018, doi: 10.1016/j.matdes.2018.10.005.
- [178] M. Shao, X. J. Zhu, H. F. Cao, and H. F. Shen, "An artificial neural network ensemble method for fault diagnosis of proton exchange membrane fuel cell system," *Energy*, vol. 67, pp. 268–275, Apr. 2014, doi: 10.1016/j.energy.2014.01.079.
- [179] Y. Bicer, I. Dincer, and M. Aydin, "Maximizing performance of fuel cell using artificial neural network approach for smart grid applications," *Energy*, vol. 116, pp. 1205–1217, Dec. 2016, doi: 10.1016/j.energy.2016.10.050.
- [180] I. S. Han, S. K. Park, and C. B. Chung, "Modeling and operation optimization of a proton exchange membrane fuel cell system for maximum efficiency," *Energy Convers. Manag.*, vol. 113, pp. 52–65, Apr. 2016, doi: 10.1016/j.enconman.2016.01.045.
- [181] M. A. R. Biswas and M. D. Robinson, "Performance Estimation of Direct Methanol Fuel Cell Using Artificial Neural Network," in *Volume 6B: Energy*, Nov. 2015, doi: 10.1115/IMECE2015-51723.
- [182] M. Tafazoli, H. Baseri, E. Alizadeh, and M. Shakeri, "Modeling of direct methanol fuel cell using the artificial neural network," *J. Fuel Cell Sci. Technol.*, vol. 10, no. 4, 2013, doi: 10.1115/1.4024859.
- [183] K. Y. Chang, C. Y. Chang, W. J. Wang, and C. Y. Chen, "Modeling polarization of a DMFC system via neural network with immune-based particle swarm optimization," *Int. J. Green Energy*, vol. 9, no. 4, pp. 309–321, May 2012, doi: 10.1080/15435075.2011.621481.
- [184] A. Hasiloglu, Ö. Aras, and M. Bayramoglu, "Artificial Intelligence Techniques for the Estimation of Direct Methanol Fuel Cell Performance," in *Journal of Physics: Conference Series*, May 2016, vol. 707, no. 1, doi: 10.1088/1742-6596/707/1/012048.
- [185] M. A. Rafe Biswas and M. D. Robinson, "Prediction of Direct Methanol Fuel Cell Stack Performance Using Artificial Neural Network," *J. Electrochem. Energy Convers. Storage*, vol. 14, no. 3, Aug. 2017, doi: 10.1115/1.4036811.

- [186] Y. Tian and H. Zou, "Modeling and control of MCFC system based on artificial neural networks," in *Conference Proceedings - IEEE International Conference on Systems, Man and Cybernetics*, 2007, vol. 6, pp. 4519–4523, doi: 10.1109/ICSMC.2006.384857.
- [187] C. Shen, G. Y. Cao, and X. J. Zhu, "Nonlinear modeling of MCFC stack based on RBF neural networks identification," *Simul. Model. Pract. Theory*, vol. 10, no. 1–2, pp. 109–119, Oct. 2002, doi: 10.1016/S1569-190X(02)00064-3.
- [188] Y. D. Tian, "Research of molten carbonate fuel cells modeling based on neural computing," in *Applied Mechanics and Materials*, 2013, vol. 389, pp. 81–84, doi: 10.4028/www.scientific.net/AMM.389.81.
- [189] T. Y. Kim, B. S. Kim, T. C. Park, and Y. K. Yeo, "Model-based control of a molten carbonate fuel cell (MCFC) process," *Korean J. Chem. Eng.*, vol. 35, no. 1, pp. 118–128, Jan. 2018, doi: 10.1007/s11814-017-0274-z.
- [190] F. Yang, X. J. Zhu, and G. Y. Cao, "Nonlinear fuzzy modeling of a MCFC stack by an identification method," *J. Power Sources*, vol. 166, no. 2, pp. 354–361, 2007, doi: 10.1016/j.jpowsour.2007.01.062.
- [191] P. L. Zervas, A. Tatsis, H. Sarimveis, and N. C. G. Markatos, "Development of a novel computational tool for optimizing the operation of fuel cells systems: Application for phosphoric acid fuel cells," *J. Power Sources*, vol. 185, no. 1, pp. 345–355, Oct. 2008, doi: 10.1016/j.jpowsour.2008.06.081.
- [192] F. J. Asensio, J. I. San Martín, I. Zamora, and J. Garcia-Villalobos, "Fuel cell-based CHP system modelling using Artificial Neural Networks aimed at developing techno-economic efficiency maximization control systems," *Energy*, vol. 123, pp. 585–593, 2017, doi: 10.1016/j.energy.2017.02.043.
- [193] P. Yuan and S. F. Liu, "Transient analysis of a solid oxide fuel cell unit with reforming and water-shift reaction and the building of neural network model for rapid prediction in electrical and thermal performance," *Int. J. Hydrogen Energy*, vol. 45, no. 1, pp. 924–936, Jan. 2020, doi: 10.1016/j.ijhydene.2019.10.165.
- [194] D. Marra, M. Sorrentino, C. Pianese, and B. Iwanschitz, "A neural network estimator of Solid Oxide Fuel Cell performance for on-field diagnostics and prognostics applications," *J. Power Sources*, vol. 241, pp. 320–329, 2013, doi: 10.1016/j.jpowsour.2013.04.114.
- [195] J. Milewski, K. Świrski, M. Santarelli, and P. Leone, *Advanced Methods of Solid Oxide Fuel Cell Modeling*. Green Energy and Technology.
- [196] J. Milewski and K. Świrski, "Modelling the SOFC behaviours by artificial neural network," *Int. J. Hydrogen Energy*, vol. 34, no. 13, pp. 5546–5553, 2009, doi: 10.1016/j.ijhydene.2009.04.068.

- [197] O. Razbani and M. Assadi, "Artificial neural network model of a short stack solid oxide fuel cell based on experimental data," *J. Power Sources*, vol. 246, pp. 581–586, 2014, doi: 10.1016/j.jpowsour.2013.08.018.
- [198] O. Razbani, I. Wærnhus, and M. Assadi, "Experimental investigation of temperature distribution over a planar solid oxide fuel cell," *Appl. Energy*, vol. 105, pp. 155–160, 2013, doi: 10.1016/j.apenergy.2012.12.062.
- [199] M. Tafazoli, M. Shakeri, M. Baniassadi, and A. Babaei, "An investigation on effect of backbone geometric anisotropy on the performance of infiltrated SOFC electrodes," *Energy Equip. Syst.*, vol. 5, no. 3, pp. 251–264, 2017, doi: 10.22059/ees.2017.27566.
- [200] M. . Fuad and M. . Hussain, "Machine Learning Based Modeling for Solid Oxide Fuel Cells Power Performance Prediction," *Proc. 6th Int. Conf. Process Syst. Eng. (PSE ASIA)*, no. June, pp. 19–24, 2013.
- [201] S. Bozorgmehri and M. Hamed, "Modeling and optimization of anode-supported solid oxide fuel cells on cell parameters via artificial neural network and genetic algorithm," *Fuel Cells*, vol. 12, no. 1, pp. 11–23, 2012, doi: 10.1002/fuce.201100140.
- [202] A. M. Nassef *et al.*, "Maximizing SOFC performance through optimal parameters identification by modern optimization algorithms," *Renew. Energy*, vol. 138, pp. 458–464, 2019, doi: 10.1016/j.renene.2019.01.072.
- [203] M. V. Le, T. A. Nguyen, and T. A. N. Nguyen, "Modeling and Optimization of the BSCF-Based Single-Chamber Solid Oxide Fuel Cell by Artificial Neural Network and Genetic Algorithm," *J. Chem.*, vol. 2019, 2019, doi: 10.1155/2019/7828019.
- [204] X.-J. Wu, X.-J. Zhu, G.-Y. Cao, and H.-Y. Tu, "Predictive control of SOFC based on a GA-RBF neural network model," *J. Power Sources*, vol. 179, no. 1, pp. 232–239, Apr. 2008, doi: 10.1016/J.JPOWSOUR.2007.12.036.
- [205] J. Tang and P. Huang, "Modeling the Electrical Conductivity of Anode for Solid Oxide Fuel Cell using Support Vector Regression Machine," *IOP Conf. Ser. Mater. Sci. Eng.*, vol. 562, p. 012095, 2019, doi: 10.1088/1757-899x/562/1/012095.
- [206] K. Chaichana, Y. Patcharavorachot, B. Chutichai, D. Saebea, S. Assabumrungrat, and A. Arpornwichanop, "Neural network hybrid model of a direct internal reforming solid oxide fuel cell," *Int. J. Hydrogen Energy*, vol. 37, no. 3, pp. 2498–2508, Feb. 2012, doi: 10.1016/j.ijhydene.2011.10.051.
- [207] J. Arriagada, P. Olausson, and A. Selimovic, "Artificial neural network simulator for SOFC performance prediction," *J. Power Sources*, vol. 112, no. 1, pp. 54–60, 2002, doi: 10.1016/S0378-7753(02)00314-2.

- [208] A. Zamaniyan, F. Joda, A. Behroozsarand, and H. Ebrahimi, "Application of artificial neural networks (ANN) for modeling of industrial hydrogen plant," *Int. J. Hydrogen Energy*, vol. 38, no. 15, pp. 6289–6297, 2013, doi: 10.1016/j.ijhydene.2013.02.136.
- [209] S. O. T. Ogaji, R. Singh, P. Pilidis, and M. Diacakis, "Modelling fuel cell performance using artificial intelligence," *J. Power Sources*, vol. 154, no. 1, pp. 192–197, 2006, doi: 10.1016/j.jpowsour.2005.03.226.
- [210] Z. Yan, A. He, S. Hara, and N. Shikazono, "Modeling of solid oxide fuel cell (SOFC) electrodes from fabrication to operation: Microstructure optimization via artificial neural networks and multi-objective genetic algorithms," *Energy Convers. Manag.*, vol. 198, no. May, p. 111916, 2019, doi: 10.1016/j.enconman.2019.111916.
- [211] B. Ghorbani and K. Vijayaraghavan, "An inverse-problem approach: Estimating multi-physiochemical properties of porous electrodes of single cell of a hydrogen-fueled solid oxide fuel cell by applying the pattern-search optimization to a pseudo-2D numerical model," *J. Power Sources*, p. 227437, Nov. 2019, doi: 10.1016/j.jpowsour.2019.227437.
- [212] B. Ghorbani and K. Vijayaraghavan, "A Novel Computationally Efficient Pseudo-2D Approach for Modeling Single Cell of a High-Temperature Solid Oxide Fuel Cell Using Modal Analysis," in *Volume 1A: 38th Computers and Information in Engineering Conference*, Aug. 2018, doi: 10.1115/DETC2018-86047.
- [213] A. Blum, *Neural Networks in C++*. NY: Wiley, 1992.
- [214] Z. Boger and H. Guterman, "Knowledge extraction from artificial neural networks models," in *Proceedings of the IEEE International Conference on Systems, Man and Cybernetics*, 1997, vol. 4, pp. 3030–3035, doi: 10.1109/icsmc.1997.633051.
- [215] M. J. A. Berry and G. Linoff, *Data mining techniques : for marketing, sales, and customer relationship management*. Wiley, 2004.
- [216] M. M. Mench, Ed., *Fuel Cell Engines*. Hoboken, NJ, USA: John Wiley & Sons, Inc., 2008.
- [217] G. Chiodelli and L. Malavasi, "Electrochemical open circuit voltage (OCV) characterization of SOFC materials," *Ionics (Kiel)*, vol. 19, no. 8, pp. 1135–1144, Aug. 2013, doi: 10.1007/s11581-013-0843-z.
- [218] "ANSYS Fluent Advanced Add-On Modules," Release 17., ANSYS,inc.
- [219] R. H. Perry, D. W. Green, and J. O. Maloney, *Perry's chemical engineers' handbook*. McGraw-Hill, 1997.

- [220] R. B. (Robert B. Bird, W. E. Stewart, and E. N. Lightfoot, *Transport phenomena*. J. Wiley, 2002.
- [221] R. E. Sonntag, C. (Claus) Borgnakke, G. J. (Gordon J. Van Wylen, and G. J. (Gordon J. Van Wylen, *Fundamentals of thermodynamics*. Wiley, 1998.
- [222] J. N. Stam, "Modeling Of Radiative Heat Transfer In Solid Oxide Fuel Cells," TU Delft, 2015.
- [223] N. Mahato, A. Banerjee, A. Gupta, S. Omar, and K. Balani, "Progress in material selection for solid oxide fuel cell technology: A review," *Prog. Mater. Sci.*, vol. 72, pp. 141–337, 2015, doi: 10.1016/j.pmatsci.2015.01.001.
- [224] K. Prabhakaran, M. O. Beigh, J. Lakra, N. M. Gokhale, and S. C. Sharma, "Characteristics of 8mol% yttria stabilized zirconia powder prepared by spray drying process," *J. Mater. Process. Technol.*, vol. 189, no. 1, pp. 178–181, 2007, doi: 10.1016/j.jmatprotec.2007.01.019.
- [225] Y. Jiang, J. Gao, M. Liu, Y. Wang, and G. Meng, "Fabrication and characterization of Y2O3 stabilized ZrO2 films deposited with aerosol-assisted MOCVD," *Solid State Ionics*, vol. 177, no. 39, pp. 3405–3410, 2007, doi: 10.1016/j.ssi.2006.10.009.
- [226] C. Brahim, A. Ringuedé, M. Cassir, M. Putkonen, and L. Niinistö, "Electrical properties of thin yttria-stabilized zirconia overlayers produced by atomic layer deposition for solid oxide fuel cell applications," *Appl. Surf. Sci.*, vol. 253, no. 8, pp. 3962–3968, 2007, doi: 10.1016/j.apsusc.2006.08.043.
- [227] V. V. Ivanov *et al.*, "Formation of a thin-layer electrolyte for SOFC by magnetic pulse compaction of tapes cast of nanopowders," *J. Power Sources*, vol. 159, no. 1, pp. 605–612, 2006, doi: 10.1016/j.jpowsour.2005.11.039.
- [228] J. H. Kuo, H. U. Anderson, and D. M. Sparlin, "Oxidation-reduction behavior of undoped and Sr-doped LaMnO3: Defect structure, electrical conductivity, and thermoelectric power," *J. Solid State Chem.*, vol. 87, no. 1, pp. 55–63, 1990, doi: 10.1016/0022-4596(90)90064-5.
- [229] A. Hammouche, E. J. L. Schouler, and M. Henault, "Electrical and thermal properties of Sr-doped lanthanum manganites," *Solid State Ionics*, vol. 28, pp. 1205–1207, 1988, doi: 10.1016/0167-2738(88)90358-X.
- [230] S.-S. Wei, T.-H. Wang, and J.-S. Wu, "Numerical modeling of interconnect flow channel design and thermal stress analysis of a planar anode-supported solid oxide fuel cell stack," *Energy*, vol. 69, pp. 553–561, 2014, doi: 10.1016/j.energy.2014.03.052.
- [231] A. Hammouche, E. J. L. Schouler, and M. Henault, "Electrical and thermal properties of Sr-doped lanthanum manganites," *Solid State Ionics*, vol. 28, pp. 1205–1207, 1988, doi: 10.1016/0167-2738(88)90358-X.

- [232] Y. W. Kang, J. Li, G. Y. Cao, H. Y. Tu, J. Li, and J. Yang, "Dynamic temperature modeling of an SOFC using least squares support vector machines," *J. Power Sources*, vol. 179, no. 2, pp. 683–692, 2008, doi: 10.1016/j.jpowsour.2008.01.022.
- [233] X. Zhang, J. Li, G. Li, and Z. Feng, "Dynamic modeling of a hybrid system of the solid oxide fuel cell and recuperative gas turbine," *J. Power Sources*, vol. 163, no. 1 SPEC. ISS., pp. 523–531, 2006, doi: 10.1016/j.jpowsour.2006.09.007.
- [234] L. Zhang, X. Li, J. Jiang, S. Li, J. Yang, and J. Li, "Dynamic modeling and analysis of a 5-kW solid oxide fuel cell system from the perspectives of cooperative control of thermal safety and high efficiency," *Int. J. Hydrogen Energy*, vol. 40, no. 1, pp. 456–476, 2015, doi: 10.1016/j.ijhydene.2014.10.149.
- [235] A. Chaisantikulwat, C. Diaz-Goano, and E. S. Meadows, "Dynamic modelling and control of planar anode-supported solid oxide fuel cell," *Comput. Chem. Eng.*, vol. 32, no. 10, pp. 2365–2381, 2008, doi: 10.1016/j.compchemeng.2007.12.003.
- [236] B. J. Spivey and T. F. Edgar, "Dynamic modeling, simulation, and MIMO predictive control of a tubular solid oxide fuel cell," *J. Process Control*, vol. 22, no. 8, pp. 1502–1520, 2012, doi: 10.1016/j.jprocont.2012.01.015.
- [237] B. gang San, P. lin Zhou, and D. Clealand, "Dynamic modeling of tubular SOFC for marine power system," *J. Mar. Sci. Appl.*, vol. 9, no. 3, pp. 231–240, 2010, doi: 10.1007/s11804-010-1001-x.
- [238] Y. Qi, B. Huang, and K. T. Chuang, "Dynamic modeling of solid oxide fuel cell: The effect of diffusion and inherent impedance," *J. Power Sources*, vol. 150, no. 1–2, pp. 32–47, 2005, doi: 10.1016/j.jpowsour.2005.02.080.
- [239] S. Kang and K. Y. Ahn, "Dynamic modeling of solid oxide fuel cell and engine hybrid system for distributed power generation," *Appl. Energy*, vol. 195, pp. 1086–1099, 2017, doi: 10.1016/j.apenergy.2017.03.077.
- [240] K. Nanaeda, F. Mueller, J. Brouwer, and S. Samuelsen, "Dynamic modeling and evaluation of solid oxide fuel cell - combined heat and power system operating strategies," *J. Power Sources*, vol. 195, no. 10, pp. 3176–3185, 2010, doi: 10.1016/j.jpowsour.2009.11.137.
- [241] A. J. Slippey, "Dynamic Modeling and Analysis of Multiple SOFC System Configurations by," *Library (Lond).*, 2009.
- [242] D. Bhattacharyya and R. Rengaswamy, "Dynamic modeling and system identification of a tubular solid oxide fuel cell (TSOFC)," *Proc. Am. Control Conf.*, pp. 2672–2677, 2009, doi: 10.1109/ACC.2009.5160183.

- [243] R. A. Roberts and J. Brouwer, "Dynamic Simulation of a Pressurized 220kW Solid Oxide Fuel-Cell & Gas-Turbine Hybrid System: Modeled Performance Compared to Measured Results," *J. Fuel Cell Sci. Technol.*, vol. 3, no. 1, p. 18, Feb. 2006, doi: 10.1115/1.2133802.
- [244] P. Sarmah, T. K. Gogoi, and R. Das, "Estimation of operating parameters of a SOFC integrated combined power cycle using differential evolution based inverse method," *Appl. Therm. Eng.*, vol. 119, pp. 98–107, Jun. 2017, doi: 10.1016/J.APPLTHERMALENG.2017.03.060.
- [245] T. Yonekura, Y. Tachikawa, T. Yoshizumi, Y. Shiratori, K. Ito, and K. Sasaki, "Exchange current density of solid oxide fuel cell electrodes," in *ECS Transactions*, 2011, vol. 35, no. 2 PART 2, pp. 1007–1014, doi: 10.1149/1.3570081.
- [246] N. V. Findler, C. Lo, and R. Lo, "Pattern search for optimization," *Math. Comput. Simul.*, vol. 29, no. 1, pp. 41–50, Feb. 1987, doi: 10.1016/0378-4754(87)90065-6.
- [247] P. Costamagna, A. Selimovic, M. Del Borghi, and G. Agnew, "Electrochemical model of the integrated planar solid oxide fuel cell (IP-SOFC)," *Chem. Eng. J.*, vol. 102, no. 1, pp. 61–69, Aug. 2004, doi: 10.1016/J.CEJ.2004.02.005.
- [248] S. Kotsiantis, D. Kanellopoulos, and P. Pintelas, "Data preprocessing for supervised learning," *Int. J. Comput. Sci.*, vol. 1, no. 2, pp. 111–117, 2006.
- [249] S. Dreiseitl and L. Ohno-Machado, "Logistic regression and artificial neural network classification models: A methodology review," *J. Biomed. Inform.*, vol. 35, no. 5–6, pp. 352–359, 2002, doi: 10.1016/S1532-0464(03)00034-0.
- [250] R. O. Duda, P. E. Hart, and D. G. Stork, *Pattern Classification (2nd Edition)*, 2nd ed. New York, NY: Wiley-Interscience, 2000.
- [251] D. Coomans and D. L. Massart, "Alternative k-nearest neighbour rules in supervised pattern recognition. Part 1. k-Nearest neighbour classification by using alternative voting rules," *Anal. Chim. Acta*, vol. 136, no. C, pp. 15–27, 1982, doi: 10.1016/S0003-2670(01)95359-0.
- [252] F. Nigsch, A. Bender, B. Van Buuren, J. Tissen, E. Nigsch, and J. B. O. Mitchell, "Melting point prediction employing k-nearest neighbor algorithms and genetic parameter optimization," *J. Chem. Inf. Model.*, vol. 46, no. 6, pp. 2412–2422, Nov. 2006, doi: 10.1021/ci060149f.
- [253] P. Hall, B. U. Park, and R. J. Samworth, "Choice of neighbor order in nearest-neighbor classification," *Ann. Stat.*, vol. 36, no. 5, pp. 2135–2152, Oct. 2008, doi: 10.1214/07-AOS537.
- [254] G. I. Webb, J. R. Boughton, and Z. Wang, "Not so naive Bayes: Aggregating one-dependence estimators," *Mach. Learn.*, vol. 58, no. 1, pp. 5–24, Jan. 2005, doi: 10.1007/s10994-005-4258-6.

- [255] P. Domingos and M. Pazzani, "On the Optimality of the Simple Bayesian Classifier under Zero-One Loss," *Mach. Learn.*, vol. 29, no. 2–3, pp. 103–130, 1997, doi: 10.1023/A:1007413511361.
- [256] A. Niculescu-Mizil and R. Caruana, "Predicting good probabilities with supervised learning," in *ICML 2005 - Proceedings of the 22nd International Conference on Machine Learning*, 2005, pp. 625–632, doi: 10.1145/1102351.1102430.
- [257] B. D. Ripley, *Pattern recognition and neural networks*. Cambridge University Press, 2014.
- [258] R. Rojas, "The Backpropagation Algorithm," in *Neural Networks*, Springer, Berlin, Heidelberg, 1996, pp. 149–182.
- [259] K. P. Murphy, *Machine Learning: A Probabilistic Perspective*, 4th ed. 2012.
- [260] T. J. DeVries, M. A. G. Von Keyserlingk, D. M. Weary, and K. A. Beauchemin, "Technical note: Validation of a system for monitoring feeding behavior of dairy cows," *J. Dairy Sci.*, vol. 86, no. 11, pp. 3571–3574, 2003, doi: 10.3168/jds.S0022-0302(03)73962-9.
- [261] P. P. Nielsen, "Automatic registration of grazing behaviour in dairy cows using 3D activity loggers," *Appl. Anim. Behav. Sci.*, vol. 148, no. 3–4, pp. 179–184, 2013, doi: 10.1016/j.applanim.2013.09.001.
- [262] S. Ruuska, W. Hämäläinen, S. Kajava, M. Mughal, P. Matilainen, and J. Mononen, "Evaluation of the confusion matrix method in the validation of an automated system for measuring feeding behaviour of cattle," *Behav. Processes*, vol. 148, pp. 56–62, Mar. 2018, doi: 10.1016/j.beproc.2018.01.004.

Appendix A.

Equations Used for Finding the Enthalpy of Species

The curves used for finding the enthalpy of the species as a function of temperature at the atmospheric pressure, found by using the data provided in tables of [221], are shown through figures A.1 to A.4. Note that only the data for temperatures between 700 °K and 2000 °K is used.

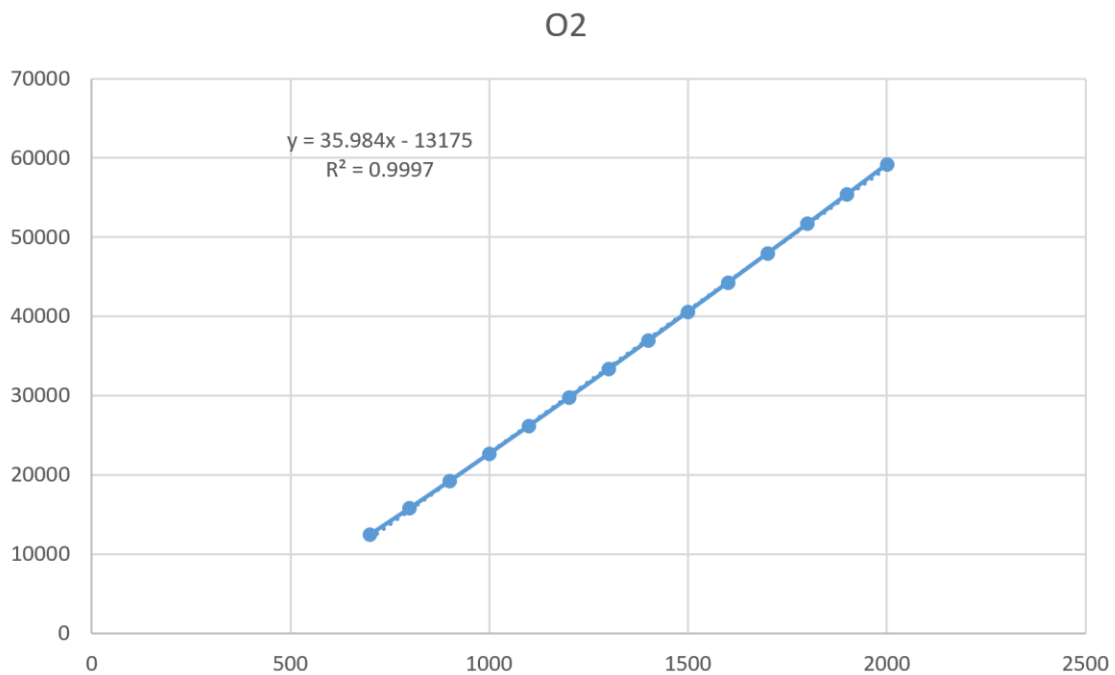


Figure A.1. Enthalpy of Oxygen in kJ/kmol as a function of temperature in °K

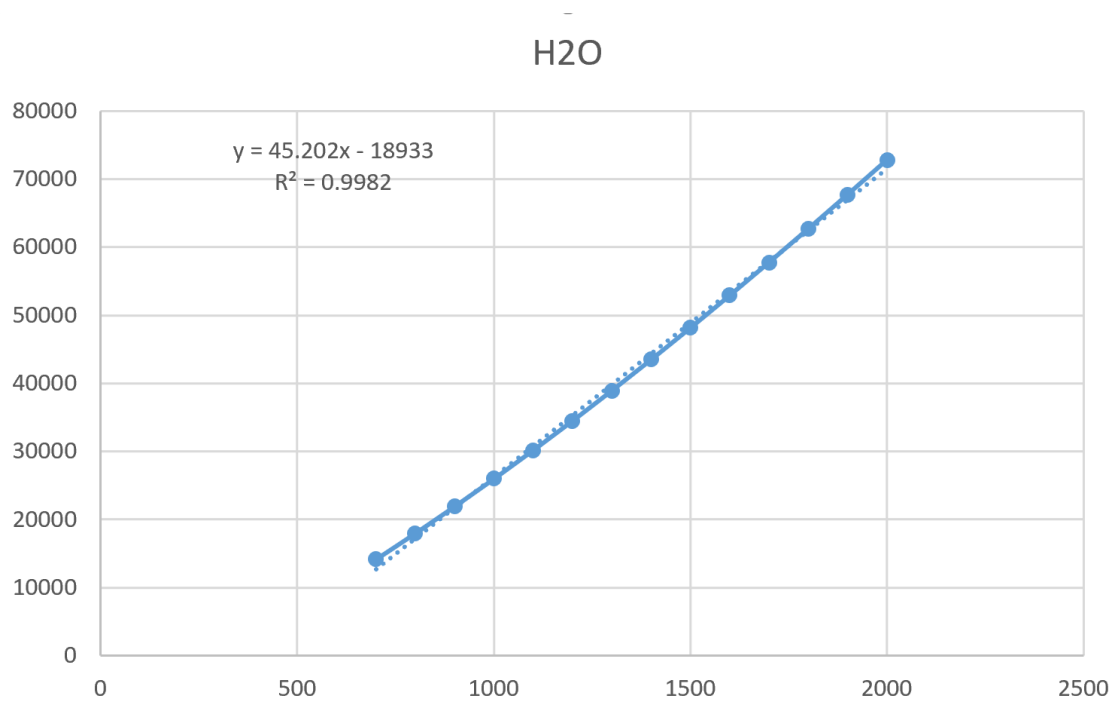


Figure A.2. Enthalpy of water vapor in kJ/kmol as a function of temperature in °K

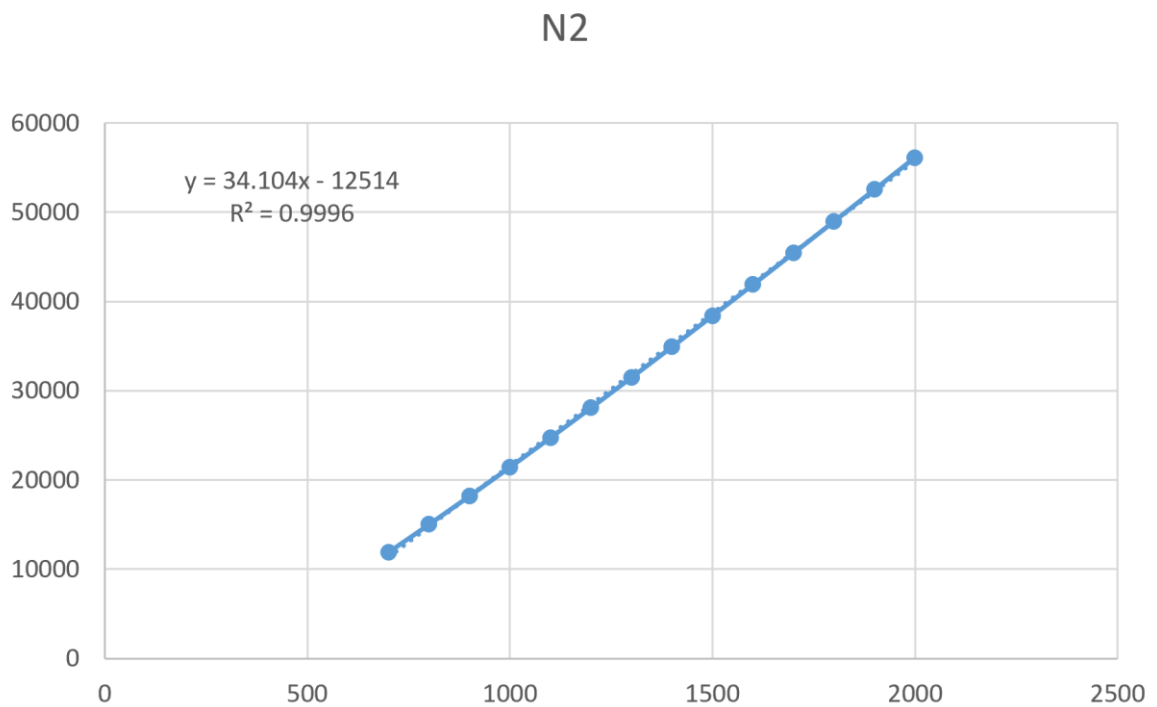


Figure A.3. Enthalpy of nitrogen in kJ/kmol as a function of temperature in °K

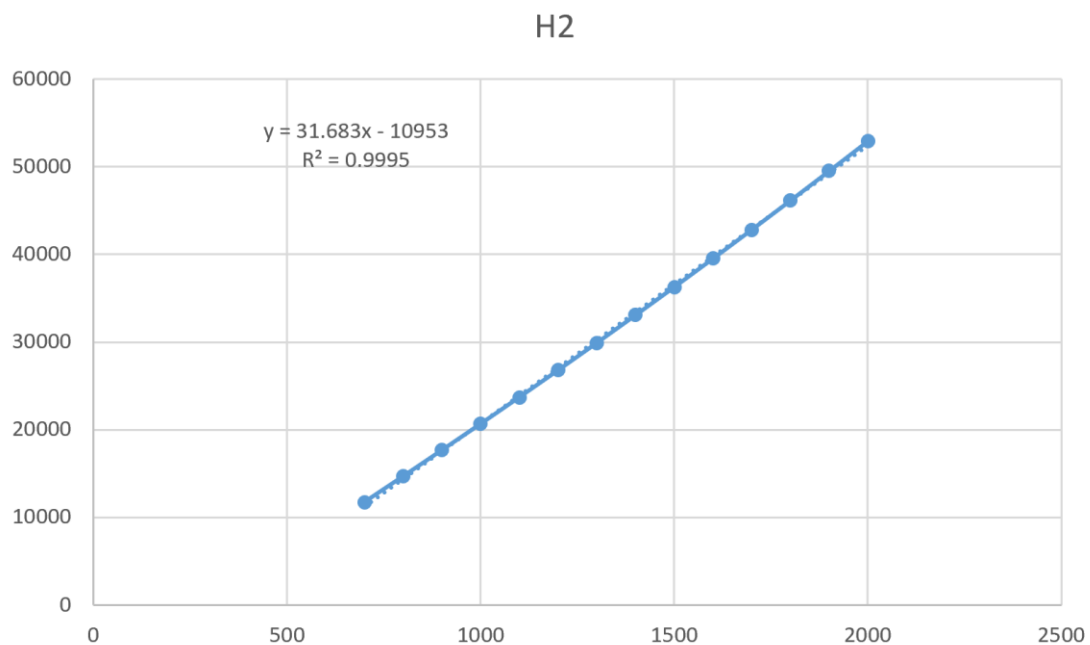


Figure A.4. Enthalpy of hydrogen in kJ/kmol as a function of temperature in °K

Appendix B.

Solution to the Steady State Energy Equation of SOFCs

In this section, the proof for the Eq. (27) is provided. The energy equation is used for a lumped control volume over the entire cell as follows:

$$\sum_{\text{inlet}} \dot{n} \bar{h} = \sum_{\text{outlet}} \dot{n} \bar{h} + V_{\text{cell}} I \quad \text{Eq. (B.1)}$$

Where, \dot{n} is the molar flow rate and \bar{h} represents the enthalpy of the species. Sums presented in Eq. (A.1) are calculated as follows:

$$\begin{aligned} \sum_{\text{inlet}} \dot{n} \bar{h} = & \dot{n}_{\text{in},a} (X_{\text{H}_2,\text{in}} \bar{h}(T_{\text{in}})_{\text{H}_2,\text{in}} + X_{\text{H}_2\text{O},\text{in}} \bar{h}(T_{\text{in}})_{\text{H}_2\text{O},\text{in}}) \\ & + \dot{n}_{\text{in},c} (X_{\text{O}_2,\text{in}} \bar{h}(T_{\text{in}})_{\text{O}_2,\text{in}} + X_{\text{N}_2,\text{in}} \bar{h}(T_{\text{in}})_{\text{N}_2,\text{in}}) = \dot{H}_{\text{in}} \end{aligned} \quad \text{Eq. (B.2)}$$

$$\begin{aligned} \sum_{\text{outlet}} \dot{n} \bar{h} = & \left(\dot{n}_{\text{in},a} X_{\text{H}_2,\text{in}} - \frac{I}{2F} \right) \bar{h}(T)_{\text{H}_2} + \left(\dot{n}_{\text{in},a} X_{\text{H}_2\text{O},\text{in}} + \frac{I}{2F} \right) \bar{h}(T)_{\text{H}_2\text{O}} \\ & + \left(\dot{n}_{\text{in},c} X_{\text{O}_2,\text{in}} + \frac{I}{4F} \right) \bar{h}(T)_{\text{O}_2} + \dot{n}_{\text{in},c} X_{\text{N}_2,\text{in}} \bar{h}(T)_{\text{N}_2} \end{aligned} \quad \text{Eq. (B.3)}$$

Using the a_i and b_i values mentioned in Table 3-2 for the enthalpy of the reactants and factoring out the unknown terms, i.e. temperature and current, yields:

$$\begin{aligned} \dot{H}_{\text{in}} = & T (a_{\text{H}_2} \dot{n}_{\text{in},a} X_{\text{H}_2,\text{in}} + a_{\text{H}_2\text{O}} \dot{n}_{\text{in},a} X_{\text{H}_2\text{O},\text{in}} + a_{\text{O}_2} \dot{n}_{\text{in},c} X_{\text{O}_2,\text{in}} + a_{\text{N}_2} \dot{n}_{\text{in},c} X_{\text{N}_2,\text{in}}) \\ & - (b_{\text{H}_2} \dot{n}_{\text{in},a} X_{\text{H}_2,\text{in}} + b_{\text{H}_2\text{O}} \dot{n}_{\text{in},a} X_{\text{H}_2\text{O},\text{in}} + b_{\text{O}_2} \dot{n}_{\text{in},c} X_{\text{O}_2,\text{in}} \\ & + b_{\text{N}_2} \dot{n}_{\text{in},c} X_{\text{N}_2,\text{in}}) + IT \left(\frac{a_{\text{H}_2\text{O}} - a_{\text{H}_2}}{2F} - \frac{a_{\text{O}_2}}{4F} \right) \\ & + I \left(\frac{b_{\text{H}_2\text{O}} - b_{\text{H}_2}}{2F} - \frac{b_{\text{O}_2}}{4F} \right) + IV \end{aligned} \quad \text{Eq. (B.4)}$$

Defining:

$$\theta_1 = b_{H_2} \dot{n}_{in,a} X_{H_2,in} + b_{H_2O} \dot{n}_{in,a} X_{H_2O,in} + b_{O_2} \dot{n}_{in,c} X_{O_2,in} + b_{N_2} \dot{n}_{in,c} X_{N_2,in}$$

$$\theta_2 = \frac{a_{H_2O} - a_{H_2}}{2F} - \frac{a_{O_2}}{4F}$$

$$\theta_3 = a_{H_2} \dot{n}_{in,a} X_{H_2,in} + a_{H_2O} \dot{n}_{in,a} X_{H_2O,in} + a_{O_2} \dot{n}_{in,c} X_{O_2,in} + a_{N_2} \dot{n}_{in,c} X_{N_2,in}$$

$$\theta_4 = \frac{b_{H_2O} - b_{H_2}}{2F} - \frac{b_{O_2}}{4F}$$

and solving for T gives the Eq. (A.5) that can be used for evaluating the steady-state temperature of the cell as a function of current, voltage, and inlet conditions.

$$T = \frac{\dot{H}_{in} - \theta_1 - (\theta_4 + V_{cell})I}{\theta_3 + \theta_2 I} \quad \text{Eq. (B.5)}$$